Natural product discovery: investigations of immunogenic cell injury and cell selectivity

By

Joseph Anthony Balsamo

Dissertation

Submitted to the Faculty of the

Graduate School of Vanderbilt University

in partial fulfillment of the requirements

for the degree of

DOCTOR OF PHILOSOPHY

In

Pharmacology

June 30, 2022

Nashville, Tennessee

Approved:

Joey V. Barnett, PhD (chair)

Brian O. Bachmann, PhD (advisor)

Charles C. Hong, MD/PhD

Amy S. Major, PhD

Julie A. Sterling, PhD

For my grandmothers, Palma and Dolores

Whose bravery and resilience know no bounds

ACKNOWLEDGEMENTS

First and foremost, I would like to thank my mentor over the past four years, Dr. Brian Bachmann. I joined the lab under extenuating circumstances, yet you adopted me as one of your own. I was right at home in the Vanderbilt Laboratory for Biosynthetic Studies.

To Dr. Charles Hong, I am grateful for laying the groundwork of my graduate training, his diligence in transitioning my mentorship to Dr. Brian Bachmann, and remaining a strong presence in my training despite the distance between Nashville and College Park, MD.

To my committee members, Amy Major, Julie Sterling, and Joey Barnett, I am thankful for the friendly and familiar presence each committee meeting despite the informality of having committee meetings over zoom. I am most thankful to all my committee members for recognizing when I needed to pause to focus on my mental health.

To Dr. Jonathan Irish and Dr. Brent Ferrel, the collaboration among our labs fostered my development for critical thinking and attention to detail (most notably in figure design).

To my lab mates past and present, I cherish the late nights and weekend shifts shared together in the VLBS, or ear tagging mice (Brenna), or method development (Maddy), or learning DebarcodeR (Sierra). Dr. Jordan Froese, Dr. Ben Reisman, Dr. Adrian Cadar, and Dr. Charles Williams I thank for their patience in teaching a bright-eyed and bushy-tailed student the ropes to graduate school and nurturing my technical skill set.

To my friends made in graduate school: Kevin, Ari, Mike, Nate, Mac, Noah, Clare, and Tim: Halloween, Friendsgiving, Holiday Party, Pontoon boat, ACME, George Jones. I look forward to our paths crossing again.

To my friends from home: Mike, Justin, Chris, Rob, and Hornak, thank you for keeping me humble and making me laugh from over 500 miles away.

To my parents Joseph and Vittoria and my sisters Alexa and Devan, without you I would not be here.

To my best friend Dr. Kelsey Pilewski, thank you for believing in me and your gleeful overcompensation. Without you graduate school would have gone a very different way.

To our cat, Wendy, meow.

TABLE OF CONTENTS

LIST OF TABLES

LIST OF FIGURES

Page

CHAPTER 1 - Introduction

1.1 Natural products as bioeffectors

1.1.1 The sheep, the cyclops, and the hedgehog

Sheep raised in Idaho ingest a litany of local flora for nourishment. In certain instances sheep ranchers observed a fatal eye deformity in young lambs (Figure 1.1) that was attributed to some unknown food source (*1*). Concerned as to the health of their flock, sheep ranchers reached out to the United States Department of Agriculture (USDA) for assistance. The USDA collected a number of vegetal specimens from the area to recreate the cyclopia in a controlled laboratory setting with mice. Ultimately, the USDA identified the California corn lily, *Veratum californicum*, as the toxic plant ingested that yielded the fatal birth defect (Figure 1.1) (*2*). To tease apart the relationship between *V. californicum* and toxicity, *Binns et al.* fed sheep, specifically female ewes, the California corn lily from a number of northwestern environments for varying durations. Toxic effects were observed to be region dependent, most notably, ewes ingesting the stems and leaves of *V.* californium harvested from Muldoon Canyon in Challis National Forest in Idaho exhibited a large number of toxic symptoms (frothing, diuresis, depression, vomiting) and birthed lambs of which greater than 50% were malformed (*3*).

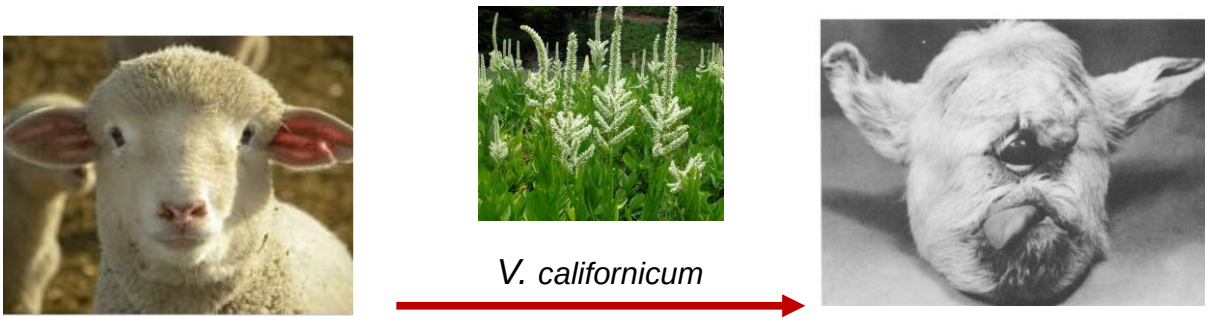

Figure 1.1. Pregnant ewes that ingest *V. californicum* birth defective lambs. The cyclopia phenotype is accompanied by a proboscis on the forehead and oral deformities.

Further study of *V. californicum* revealed ingestion on the plant on the 14th day of gestation provoked the lethal cyclopia in lambs, however the singular chemical agent responsible for the lethality remained unknown (*2*). It was hypothesized that the bioactive component belonged to the alkaloid family of natural products as a number of other *Veratum* species synthesized alkaloid compounds with known teratogenic effects (*3*). Subsequently, several alkaloids were isolated from *V. californicum* and tested in biological systems to identify the natural product that induced these developmental disorders. The compound was determined to be a deoxygenated structural analog of jervine (11-deoxojervine) later named cyclopamine (Figure 1.2) (*4*).

The cyclopamine induced cyclops phenotype was not unique to environmental causes. Indeed, this facial anomaly has genetic basis in the family of *Hedgehog (Hh)* genes. Initial studies in *Drosophila melanogaster*, or fruit flies, identified *Hh* genes that organized developmental patterning of mature, adult-like structures including the nervous system and limbs (*5*). This phenomenon was not exclusive to the fruit fly but rather evolutionarily conserved in higher order species including mouse, lamb, and human(*6-8*). Loss of *Hh* in mouse by double knockout resulted in cyclopia and defective axial patterning of the limbs (*6*). *Hh haploinsufficiency* in human also as

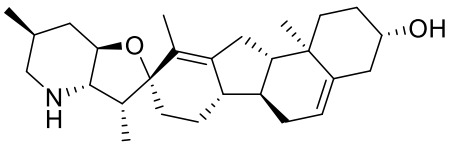

Figure 1.2. Structure of cyclopamine.

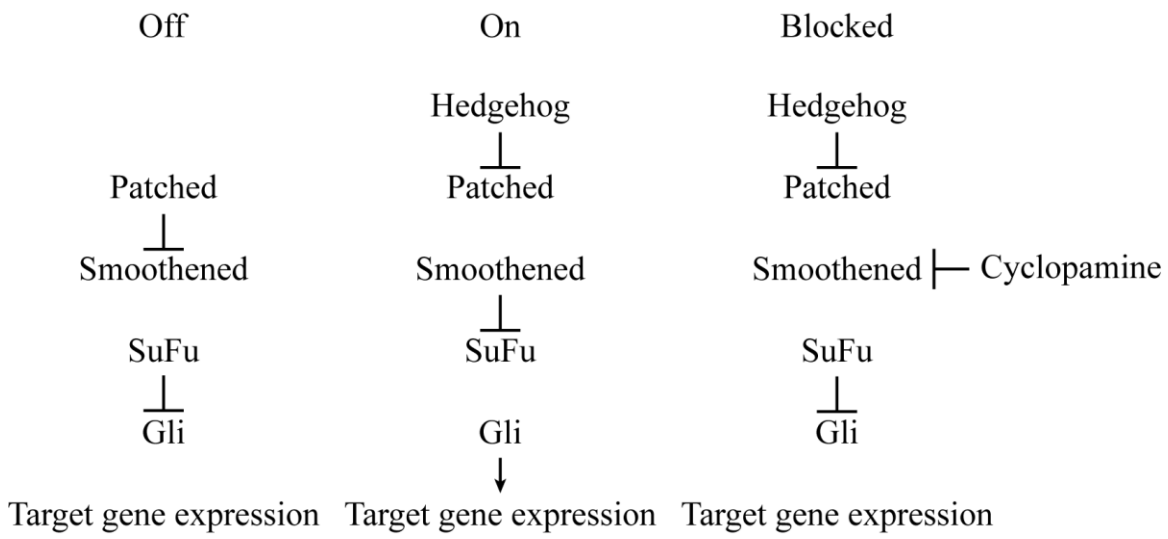

Figure 1.3. Hedgehog signaling in off, on, and blocked states.

dire developmental consequences. For example, work by *Muenke et al* identified *SHH* as the first genetic culprit of holoprosencephaly (HPE), a medical condition in which the forebrain fails to separate into left and right hemispheres leading to an undivided eye field (i.e. cyclopia). By studying 30 families Muenke's research group identified nonsense and missense mutations that sufficiently disrupted *SHH* signaling in human that prevented appropriate neurogenesis (*7*).

While deficits in *Hh* signaling during development results in pronounced body plan malformities, a surplus of *Hh* signaling outside of neonatal developmental windows promote cancer development, a process known as oncogenesis. The hedgehog signaling pathway contains additional proteins including patched (PTCH), smoothened (SMO), suppressor of fused homolog (SUFU) and the transcription factor gli (GLI). After neonatal development *Hh* signaling is largely in the "off" state (Figure 1.3). In the off state, PTCH is bound to SMO and SUFU is bound to the transcription factor GLI (Figure 1.3). In the "on" state, HH binds PTCH at the cell surface leading to the release of SMO. SMO then inhibits SUFU allowing GLI to translocate the nucleus to engage Hh transcriptional programs required for proper development. In certain cancers including basal cell carcinoma and medulloblastoma mutations in *PTCH* and *SMO* gene sequences can drive

constitutive *Hh* signaling activation to promote abnormal cell growth towards the development of metastatic tumors. It was observed that treating cancer cells with cyclopamine inhibits *Hh* signaling suggesting a mechanistic basis, that is the association of a compound with a biological target, for tumor therapy and also HPE induced cyclopia (*9, 10*). Later works by *Beach et al.* developed fluorescent and photoaffinity cyclopamine derivatives to reveal cyclopamine directly bound SMO leading to *Hh* signal blockade (Figure 1.3) (*8*).

The story of cyclopamine delineates a textbook example of natural product influence on mammalian cell phenotypes by discrete interactions with molecular targets. Pregnant ewes ingesting *V. californicum* birthed cyclops lambs consistent with prior observations of alkaloid teratogenic effects of compounds isolated from the California corn lily. This pharmacological observation was later supported by genetic mutations in humans that diminished *Hh* signaling and recapitulated HPE and cyclopia phenotypes thus providing an essential clue that cyclopamine may target the *Hh* pathway. Subsequent studies confirmed that cyclopamine (Figure 1.2) binds SMO to block *Hh* signaling (Figure 1.3) and that this was the chemical agent responsible for the deformed lambs (Figure 1.1) Moreover, while detrimental during development, cyclopamine inhibition of SMO offered a hopeful therapeutic for *Hh* dependent cancers. The most remarkable aspect of these naturally derived or inspired medicinal sources is that from within the entire consortium of biomolecules within these organisms is that individual chemical constituents can be isolated and evaluated independently for bioactivity.

1.1.2 Nature's pharmacopeia

The previous section focused on the discovery of cyclopamine as a *Hh* pathway inhibitor isolated from the plant *V. californicum*. Plants are indeed a bountiful source of natural products with diverse impacts on human biology. Willow bark was historically used for pain management

and gave rise to salyicylic acid which became known as aspirin (*11*). Taxol a potent anti-cancer compound that stabilizes microtubule cell architecture was isolated from a number of *Taxus* species (*12*). Etoposide, a topoisomerase poison used in testicular and lung cancers was isolated from the rhizomes of wild mandrakes (*Podophyllum peltatum*) (*13*).

Fungi as well are a plentiful source of natural products with medicinal implications. Perhaps the most famous example of a fungus derived secondary metabolite is penicillin. The penicillin producing fungus *Penicillium notatum* was observed by Dr. Alexander Fleming in 1929 as a contaminant on bacterial culture dishes; however, this "contaminant" featured a zone of inhibition surrounding fungal colonies that prevented bacterial growth (*14*). From Dr. Fleming's initial observation in 1929, efforts to purify penicillin as a medicine remained lackluster until the onset of World War II. It was hypothesized that treatment of penicillin to wartime wounds could prevent infections and save lives, it did (*15*). The success of penicillin contributed to the 'golden age of antibiotics' in which a large majority of today's antibacterial compounds were discovered. Outside of antibacterial properties, fungal secondary metabolites are garnering attention as a future treatment scheme for depression. The psychedelic compound psylocibin when consumed in large doses elicits effects of euphoria and hallucinations. When consumed in smaller, clinically regimented doses, psylocibin exhibits anti-depressive properties that last in excess of six months in patient cohorts resistant to treatment with traditional synthetic agents such as fluoxetine (*16, 17*).

While the golden age of antibiotic discovery was kickstarted by a fungal natural product, it was dominated by discovery of secondary metabolites from bacteria (*18*). In fact, earthy odors most prominent after rain is due to production of a volatile compound, geosmin, synthesized by a number of *Actinobacteria* belonging to the genus Streptomyces (*19, 20*). The Streptomyces genera

produces over two-thirds of antibiotics including streptomycin, neomycin, tetracycline and an antibiotic of last resort vancomycin. The utility of antibiotics in human medicines is owed in part to selective binding of prokaryotic, but not eukaryotic, ribosomes that stalls protein synthesis and results in death of the bacterial cell (*21*). However, not all secondary metabolites impart function by selectively targeting bacterial ribosomes. Notably, a large component of modern chemotherapies are secondary metabolites that disrupt cellular processes such as mitochondrial function, signal transduction, and DNA replication (*22*-*25*). Recently, the apoptolidin family of glycomacrolides were shown to selectively inhibit the F_1 subcomplex of mitochondrial ATP synthase and prevent leukemia growth in MV-4-11 xenograft mouse models (*26*).

1.1.3 Phenotypic drug discovery

Drug discovery is an exhaustive process that typically follows one of two methods. Method 1, the target-based screen, uses genetic information to identify protein targets implicated in a disease state. Thousands of compounds are screened against the single target protein. Compounds with activity, determined by one biological assay, are advanced and chemically optimized for high-affinity binding and low toxicity. Successful compounds are advanced to animal models with the ultimate goal of gaining clinical approval. Method 2, phenotypic drug discovery (PDD), identifies bioactive compounds by quantifying an assortment of cellular parameters in tandem without regard for target. Between 1999 and 2008 PDD based discovery paradigms contributed 68% of U.S. Food and Drug Administration approved new molecular entities compared to 39% contribution from target-base approaches (*27*).

A successful PDD campaign must determine quantitative endpoints for unambiguous decision on calling ‘hits’ to advance as lead compounds. Historically, death in response to compound exposure indicated a positive hit. In fact, the anthracycline compound doxorubicin was

discovered in this fashion. First isolated from a soil derived *Streptomyces peucetius*, doxorubicin exhibited weak activity against Gram-positive bacteria but was quite efficient at inhibiting transplanted tumors onto mouse and rat to prolong overall survival (*23, 28*). From these initial trials PDD by death expanded and evolved to include plate-based assays that measured cell viability by vital dye staining, mitochondrial activity, and colony formation assays (*29-31*). Even so, these assays remain limited in their capacity to detect signaling pathways that occur prior to and contribute to cellular demise. Surely, death is a simple yes/no endpoint for evaluating overt cytotoxicity but falls drastically short in identifying the 'why' and 'how' of the cytotoxic endpoint. Moreover, is death the be-all-end-all for finding future chemotherapies? To this point chemotherapies identified in this fashion present a number of unpleasant side effects and can induce heart failure. Perhaps a more fruitful approach to discovery is to measure modulation of cell signaling pathways with specific biomarkers.

1.2 Immunogenic cell death

1.2.1 Chemically induced anti-tumor immunity

Immune cells recognize degenerated self-cells regularly to maintain homeostasis. Part of this function includes identification and elimination of would-be cancer cells prior to tumor establishment. Oncogenesis occurs when cells acquire the "correct" number/types of genetic mutations that enable evasion from the immune system. Once detected, a chemotherapeutic regiment can be applied to kill tumor cells that the immune system could not. The intent of chemotherapy is to inhibit some essential cellular process that fostered cancer development to ultimately induce cell death. Upon, or during, cell demise tumor associated antigens (TAA) are released to the extracellular milieu and, if recognized by immune cells, can activate durable immune responses. This phenomenon of a chemical agent eliminating cancer cells in a manner

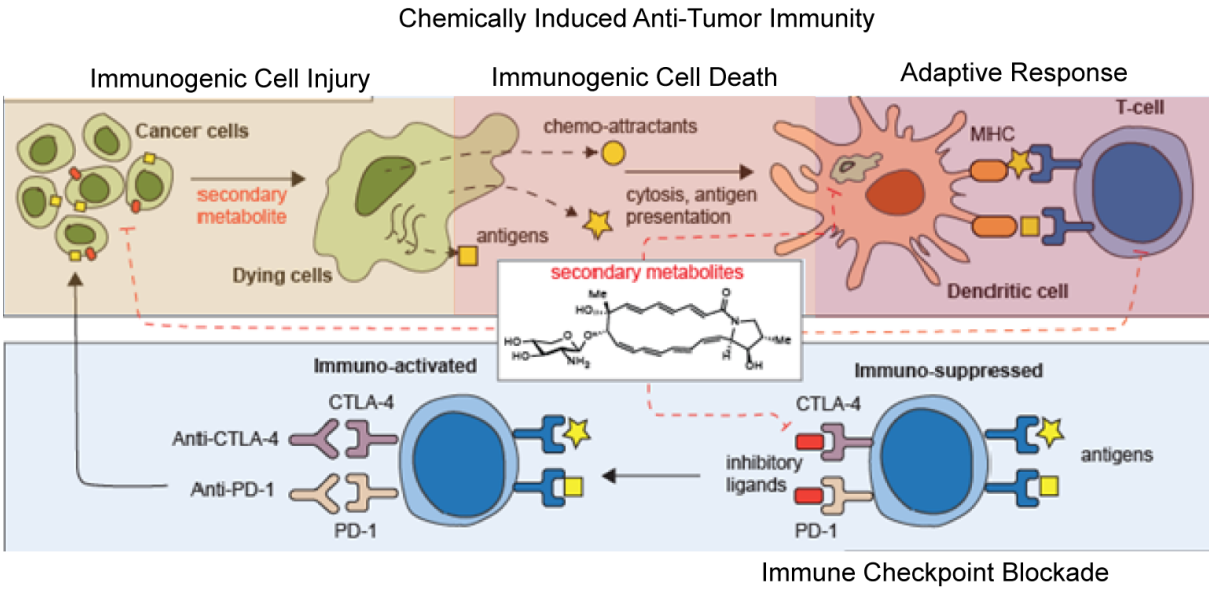

Figure 1.4. Chemically induced anti-tumor immunity schematic separate by injury, death, response, and checkpoint blockade.

that activates an adaptive immune response against TAA is referred to as chemically induced anti-tumor immunity (CIATI) (Figure 1.4).

CIATI references a vast array of biological stressors prescient of cell death that effectively prime the immune system for an enduring anti-tumor response. A major form of CIATI that has received considerable attention is immunogenic cell death (ICD) (*31*). ICD is broadly defined as a form of programmed cell death that sufficiently activates adaptive immune responses in immunocompetent syngeneic hosts. This definition captures the two core components of ICD: the cellular death component and the host response component. The death component, a form of adjuvanticity, catalyzes immune responses by releasing damage associated molecular patterns (DAMPs) to the extracellular space to enhance inflammation and recruit host immune cells (*32*). The recruited host cells then respond to antigenic moieties of the decomposing cell to initiate and amplify the magnitude of immune cell-mediated responses (Figure 1.4).

This paradigm is best exemplified by the pioneering works of Kroemer *et al.* In one of their experiments, a chemical agent is used to challenge tumor *ex vivo*. Following challenge, the cell/drug cocktail is injected into an immunocompetent mouse. Seven to ten days after the first injection, a second injection of only tumor cells is applied to the same mouse. The mouse in then assessed periodically for the tumor emergence. If no tumor develops then the compound used to challenge tumor cells in the first injection elicited ICD. However, if a tumor develops then the compound did not induce ICD. A positive ICD result is then confirmed with immunodeficient mice. The cell/drug mixture is again injected followed by a second injection of cells seven to ten days later. Since no immune response can occur, the tumor is expected to proliferate and confirm that ICD conferred an adaptive immune response that protects immunocompetent mice from tumor rechallenge (*31*). Successful chemotherapies originally discovered by cytotoxicity, such as the anthracycline doxorubicin, were observed *post-hoc* to induce ICD and promote durable anti-tumor immunity (*33, 34*).

Identifying CIATI competent compounds and cancers forecasts a treatment paradigm that couples traditional chemotherapeutics with next generation checkpoint inhibitors, notably monoclonal antibodies. Under homeostatic conditions, checkpoint interactions between immune and non-immune cells serve as a check-points to prevent an inappropriate inflammatory immune response against healthy cells (Figure 1.4). Some cancers employ these checkpoint interactions to evade immune cell detection. Immune checkpoint blockade (ICB) with monoclonal antibodies can re-establish immune cell mediated destruction of a tumor. (*35, 36*). Certain cancers respond remarkably well to ICB but it is not a cure all. ICB-resistant cancers may be overcome by first activating cellular processes that promote CIATI to lower the barrier of immune cell invasion followed by ICB administration to enhance anti-cancer immune cell functions. (Figure 1.4).

Finally, DNA stress in the form of double strand breaks can act as a powerful adjuvant to induce durable antitumor immunological memory. In *ex vivo* culture systems, etoposide in combination with mitoxantrone enhanced dendritic cell mediated T cell activation in the absence of certain immunogenic signals (*37*). Intratumoral injection of *ex vivo* etoposide challenged tumor cells in combination with ICB induced total tumor regression and protected from tumor rechallenge in mouse (*37*). This example highlights CIATI as a combination therapy with ICB.

1.2.2 Immunogenic cell injury

Prior to CIATI, mammalian cells respond to environmental stimuli via a myriad of signaling processes to inform cell survival or demise. Several injury signals arise from homeostatic mechanisms intended to promote cell survival. For example, autophagy degrades and recycles effete organelles to meet bioenergetic needs in nutrient deficient environments (*38*). This process is frequently detected by modulation of the protein the light chain 3 (LC3) which facilitates fusion between functional autophagic components to degrade molecular cargo (*39, 40*). Autophagy competence is required for release of specific immunogenic DAMPs and can facilitate metastasis in late-stage cancers (*41*). Therefore, inhibition of autophagy competent cells may prove fruitful for cancer therapy. In addition to surmounting nutritional stress by autophagy, cells can fine tune translation status to manage endoplasmic reticulum (ER) stress when protein synthesis exceeds ER folding capacity by activating the unfolded protein response (UPR), a stop-gap aimed to balance ER folding capacity with unfolded protein load. Specifically, phosphorylation of translation initiation factor EIF2α (p- EIF2α) prevents translation initiation by inducing conformational changes in EIF2B until proteostasis in restored (*42-45*). Unresolved ER stress marked by p-EIF2α imbues a "switch" from pro-survival to injury signal (*43*).

Outside of rouge homeostatic processes, specific forms of cell death also contribute to immunogenicity. Apoptosis is canonically considered tolerogenic form of cell death, essential to cell turnover and embryonic development, that does not emit DAMPs to elicit a productive immune response (*46*). This form of cell death is governed by the proteolytic caspase family of enzymes which are activated by cleavage to ultimately activate the terminal apoptotic caspase enzyme caspase 3 (cCAS3). Morphologically, apoptotic cells are identified by pyknotic nuclei, overall shrinkage, and blebbing of apoptotic bodies which are phagocytosed by tingible body macrophages (*46*). Fortunately, chemically induced apoptosis can be immunogenic. Indeed, inoculation of mice with doxorubicin challenged CT26 colon carcinoma cell line did confer resistance to tumor rechallenge (*33*). Alternative to apoptosis, necroptotic cell death includes cellular swelling followed by membrane rupture to facilitate leakage of cellular components to the extracellular space(*47*). Necroptosis is tightly regulated by phosphorylation of the receptor-interacting protein kinase (RIPK) family of proteins and mixed lineage kinase-domain like (MLKL) protein. Phosphorylation of MLKL at serine 358 in human by p-RIPK3 indicates a necroptotic response (*48-50*). The p-MLKL transverses the cell nucleus and cytosol to arrive at the cell membrane and form oligomers in the plasma membrane resulting in cell lysis and release of immunogenic moieties (*51, 52*). Vaccination with necroptotic cells is sufficiently immunogenic for activation for adaptive immune responses (*53*).

1.2.3 Key damage associated molecular patterns (DAMPs)

DAMPs are critical danger stimuli that draw circulating antigen presenting cells (APCs) into sites of cellular injury and foster maturation. Under healthy conditions DAMPs released by dying cells relay danger signals to maintain organism integrity. In an immunogenic context DAMPs,

particularly ATP, HMGB1 and calreticulin, are emitted in response to intracellular stress and are linked mechanistically to adaptive responses in preclinical models (*32, 54, 55*).

ATP drives recruitment of APCs to dying cells and promotes maturation and capacity for antigen cross presentation. ATP is released to the extracellular space by LAMP1 and PANX1 mediated cellular blebbing as well as anterograde ER-to-golgi transport (*56, 57*). Extracellular ATP induced chemotaxis of immune cells is regulated in part by binding purinergenic receptors P2Y and P2X on the APC cell surface to activate the NLRP3 inflammasome that activates inflammatory cytokine IL-1β (*58*).

HMGB1 contributions to ICD are somewhat convoluted as the oxidation status of HMGB1 is critical to its immunogenicity. Oxidized HMGB1can prompt immunostimulatory functions of an APC cell type known as dendritic cells (DCs) by binding TLR4 surface receptors (*59*). This engages cross-priming in dendritic cells to enhance activation of anti-tumor T cells (*59, 60*). In contrast, reduced HMGB1 is anti-inflammatory and binds RAGE receptors to enhance autophagy and depress apoptosis (*61, 62*). HMGB1 incompetent ICD can be overcome with other TLR4 agonists (*60*).

Endoplasmic reticulum stress stimulates injury mediator p-EIF2α that can lead to translocation of ER resident chaperone proteins to the outer leaflet of the cell membrane. Exposure of certain ER chaperones, including calreticulin, promotes uptake of cellular debris and dying cells by DCs via LDL related receptor protein, CD91. Additionally, DC activation by calreticulin is driven by PI3K/AKT signaling pathway and can increase surface expression of activation markers CD80 and CD86 (*63, 64*) that interact with naïve cells T cells to inform an antigen specific adaptive immune response (*65*).

1.3 Natural product discovery workflows

1.3.1 Sourcing natural products

Microbial natural products form the basis for many human therapeutics against diverse clinical indications. However, the journey from a microbial source, to discovered metabolite, to the clinic, is circuitous and not frequently driven by human biological insights nor clinically relevant endpoints. Hence, it is largely possible that many undiscovered or known scaffolds and/or scaffold analogs possess pharmacological properties in humans that are not revealed by traditional cytotoxicity and target-based discovery paradigms. One goal is to accelerate natural product discovery in the context of precision medicine in a way that takes advantage of the structural diversity and variation between and within classes of secondary metabolites to identify compounds with high potential for clinical development.

To drive discovery of natural product bioeffectors we developed a function-centric (*66*), or phenotypic, screen that leverages single cell methods (*67, 68*) to coordinate stimulus conditions, dose-response data, and fluorescent reporter assays for genetic-free interrogation of microbial extracts from diverse culture collections (Figure 1.5) . The Vanderbilt Laboratory for Biosynthetic Studies actinobacteria collection houses >500 actinomycetes purified by restrictive culturing methods (*69, 70*) from cave ecosystems, an under-utilized source of diverse actinomycete genera (*71, 72*) with nascent biosynthetic potential (*69, 71, 73, 74*).

1.3.2 Fluorescent cell barcoding

Fluorescent cell barcoding is a high-throughput tool to catalog 48 experimental well conditions on a 96-well plate with an eight by six array of NHS succimidyl-ester functionalizd fluorescent dyes that react covalently with primary amines within proteins(*75, 76*). Following barcoding, cells are pooled and stained with a fluorescent cocktail that detects markers of interest

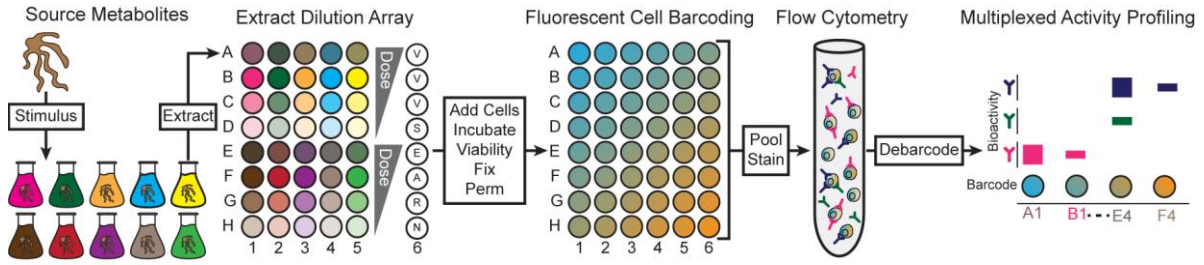

Figure 1.5. Multiplexed activity profiling workflow. Metabolomes of stimulated organisms are extracted and serially diluted to detect dose dependent phenotypes. Cells are plated over the extract dilution array, fluorescently

by flow cytometry (Figure 1.5). Single cell, fluorescent information is acquired with a flow cytometer and quality controlled for viable, intact singlet cells. Viable cells are debarcoded with the R script DebarocdeR to digitally reassign cells to origin plate wells for signal investigation (*77*).

1.3.3 Multiplexed activity profiling

Herein is described a multiplexed activity profiling system (MAP) that simultaneously correlates multiple stimuli of natural product biosynthesis against multiple single cell phenotypic markers of mammalian cell function to rapidly determine productive activation conditions (Figure 1.5). The MAP assay uses fluorescent cell barcoding to screen for dose-dependent bioactivity in crude extracts (Figure 1.5). Chemically dependent responses in single cells are acquired with flow cytometry and the biological data is deconvoluted with the DebarcodeR algorithm to enhance and automate computation of biological activity (*77*). This suite of tools can be used for diverse applications in the discovery of bioeffectors from virtually any source ranging from compound libraries to the products of primary and secondary metabolism.

1.3.4 Multiplexed Activity Metabolomics

To unambiguously link initial biological phenotypes of interest in an extract to a discrete

metabolite, it is typically necessary to isolate and structurally identify a metabolite of interest prior to investigating the scope of its bioactivity. This remains an additional rate determining step in activity-based workflows. Multiplexed activity metabolomics (MAM) can identify known molecular features within active extracts and rapidly prioritize potentially new molecular features for further characterization (Figure 1.6). MAM accelerates the discovery of both previously unreported secondary metabolites and known compounds with novel biological phenotypes with potential for human medicine. Of note, MAM can be practiced with suspended mammalian cell lines or primary cell preparation to provide insight to pharmacological potential, in many cases, even prior to compound isolation. MAM fractions metabolomes with reverse phase high performance liquid chromatography and catalogs metabolomic components with mass spectrometry (MS) (Figure 1.6). To enable discovery of bioactive compounds the retention times of eluate fractions and associated chromatographic features are matched to well plates. For instance, spectral data acquired from retention time 0:01 to 1:00 matches collected eluate in well 1. Fractions are dried *in vacuo* and dissolved in cell containing media for overnight incubation. Cells are processed for fluorescent cell barcoding and stained with fluorescent antibodies to measure chemically induced cell signals with flow cytometry. Acquired cellular data is debarcoded to examine well-specific bioactivity of each fluorescent reporter. Bioactive wells are tracked to MS/UV data to infer well isolated ions and absorbance spectra (Figure 1.6). Bioactive lead secondary metabolites are isolated by varying chromatographic techniques (size exclusion, preparative HPLC, silica plates, etc.) and dereplicated with nuclear magnetic resonance (NMR) and hi-resolution mass spectrometry.

1.4 Statement of Dissertation

Natural products can exhibit profound impacts on biological systems via chemical interactions with specific molecular targets to yield a demonstrable deviation from expected phenotypes. These phenotypic shifts can be as obvious as cyclopia and as subtle as phospho-protein status in single cells.

Actinobacteria are, historically, a rich source of secondary metabolites that interact with distinct molecular targets to impart phenotypic change. The genomes of these bacteria encode biosynthetic enzymes capable of diverse chemical reactions that assemble complex molecular scaffolds; however, engaging biosynthesis of said molecules and gauging their therapeutic potential in eukaryotic systems remains a central challenge in the natural product discovery field. This dissertation attempts to address these gaps by exposing actinobacteria of different genera to a diverse array of chemical and biological stimuli to induce biosynthesis of natural products that are extracted and administered to cancer cells to observe eukaryotic injury signals relevant to cancer therapy. The single cell assay developed herein measures immunogenic cell injury signals in response to bacterial extracts to prioritize isolation of natural products by bioactivity and interrogate therapeutic potential in primary patient samples. Chapter 1 introduced CIATI, ICI and ICD. Chapter 2 is focused on developing an immunogenic module (a composition of fluorescently conjugated antibodies) that measured different forms of ICI. Benchmark secondary metabolites with established chemical-biological mechanisms were applied to optimize induction and detection of injury signal using MAP and MAM. Direct application of this module identified new bioactivity of the natural product narbomycin.

Injury signals induced by benchmark compounds were also correlated to hallmarks of ICD: the release of ATP and ejection of nuclear protein HMGB1 to extracellular space and

externalization of the resident ER protein calreticulin. The correlation of ICI and ICD provide a nascent roadmap for distinguishing optimal intensity, sequence, and number of ICI sufficient to promote CIATI.

In chapter 3, two examples of the MAM discovery workflow are provided. Example one identifies the secondary metabolite siderochelin as the active chemical agent that induces DNA damage injury signal. In example two a family of filipin compounds that exhibited non-specific cytotoxicity were isolated. Additional studies confirmed injury independent cell death and identified a new member of the filipin family of molecules.

Chapter 4 exemplifies an ideal discovery workflow in which MAM identified an isolable bioactive natural product that was advanced to experiments in primary patient cells. The isolated compound, isoquinocycline B, is a member of the anthracycline family of compounds and induced a DNA damage phenotype and enhanced DNA content. This compound was compared to two additional anthracyclines in healthy PBMC and three AML patient samples by measuring cell identity specific functional responses and distribution of cell type populations. The findings illustrate that anthracyclines can modulate distinct molecular pathways in specific cell subsets and patients.

Chapter 5 concludes this dissertation by expanding potential avenues for future work based on the findings in the previous chapters. Some topics include exploration of new biological phenotypes exerted by rediscovered natural products, an opportunity for *ex vivo* immunotherapy, and expanding MAP, MAM, and the ICI module to include surface identity markers for cell specific discovery in primary patient samples as well as assay expansion into additional cell lines.

Some of the findings contained within this dissertation can be attributed to the efforts of colleagues and collaborators. Kathryn Penton isolated and cultured bacterial species that produced

the bioactive extracts in chapters two and four. She also isolated isoquinocycline B. Zhin Zhao performed ATP-luciferase assays in chapter two and assisted with cell culture. Dr. Jordan Froese isolated and cultured bacterial species in chapter three in addition to isolating and deciphering the chemical structures of the filipin family of compounds. Dr. Benjamin Reisman and Dr. Brent Ferrell assisted with designing cytometry experiments described in chapter four and Chad Potts performed Cytof data acquisition. Dr. Jonathan Irish was instrumental for experimental design to validate the ICI module and provided critical feedback during figure generation. Irish lab members Madeliene Hayes and Sierra Barrone facilitated data acquisition by acquiring and processing MAP and MAM data in chapters three and four. Dr. Brian Bachmann elucidated the structure of siderochelin in chapter three and isoquinocycline B in chapter four.

1.5 References

1. W. Binns, E. J. Thacker, L. F. James, W. T. Huffman, A congenital cyclopian-type malformation in lambs. *Journal of the American Veterinary Medical Association* **134**, (1959).
2. L. F. J. Wayne Binns, James L. Shupe, Oxicosis of Veratum Californicum in ewes and its relationship to a congenital deformity in lambs. *Annals New York Academy of Sciences*, (1964).
3. R. F. Keeler, W. Binns, Teratogenic compounds of Veratum californicum. *Canadian Journal of Biochemistry* **44**, (1966).
4. G. William, M. Benson, R. E. Lunding, Carbon-13 and proton nuclearm magnetic resonance spectra of veratum alkaloids *Journal of Natural Products* **49**, (1986).
5. M. K. Cooper, J. A. Porter, K. E. Young, P. A. Beachy, Teratogen-mediated inhibition of target tissue response to Shh signaling. *Science* **280**, (1998).
6. C. Chiang *et al.*, Cyclopia and defective axial patterning in mice lacking Sonic hedgehog gene function. *Nature* **383**, 407-413 (1996).
7. E. Roessler *et al.*, Mutations in the human Sonic Hedgehog gene cause holoprosencephaly. *Nature Genetics* **14**, 357-360 (1996).
8. J. K. Chen, J. Taipale, M. K. Cooper, P. A. Beachy, Inhibition of Hedgehog signaling by direct binding of cyclopamine to Smoothened. *Genes Dev* **16**, 2743-2748 (2002).
9. J. P. Incardona, W. Gaffield, R. P. Kapur, H. Roelink, The teratogenic Veratrum alkaloid cyclopamine inhibits sonic hedgehog signal transduction. *Development* **125**, 3553-3562 (1998).
10. J. Taipale *et al.*, Effects of oncogenic mutations in Smoothened and Patched can be reversed by cyclopamine. *Nature* **406**, 1005-1009 (2000).
11. M. J. R. Desborough, D. M. Keeling, The aspirin story - from willow to wonder drug. *British Journal of Haematology* **177**, 674-683 (2017).
12. M. Fridlender, Y. Kapulnik, H. Koltai, Plant derived substances with anti-cancer activity: from folklore to practice. *Front Plant Sci* **6**, 799 (2015).
13. J. M. S. Van Maanen, J. Retel, J. De Vries, H. M. Pinedo, Mechanism of Action of Antitumor Drug Etoposide: A Review. *JNCI Journal of the National Cancer Institute* **80**, 1526-1533 (1988).
14. A. Fleming, On the antibacterial action of cultures of a penicillium, with special reference to their use in the isolation of *B. influenzae*. *The British Journal of Experimental Pathology* **10**, (1929).
15. R. Quinn, Rethinking Antibiotic Research and Development: World War II and the Penicillin Collaborative. *American Journal of Public Health* **103**, 426-434 (2013).
16. A. K. Davis *et al.*, Effects of Psilocybin-Assisted Therapy on Major Depressive Disorder. *JAMA Psychiatry* **78**, 481 (2021).
17. R. L. Carhart-Harris *et al.*, Psilocybin with psychological support for treatment-resistant depression: six-month follow-up. *Psychopharmacology* **235**, 399-408 (2018).
18. J. Davies, Where Have all the Antibiotics Gone? *Canadian Journal of Infectious Diseases and Medical Microbiology* **17**, 287-290 (2006).
19. N. N. Gerber, Volatile substances from actinomycetes: their role in the odor pollution of water. *CRC Crit Rev Microbiol* **7**, 191-214 (1979).
20. J. Jiang, X. He, D. E. Cane, Biosynthesis of the earthy odorant geosmin by a bifunctional Streptomyces coelicolor enzyme. *Nat Chem Biol* **3**, 711-715 (2007).
21. D. J. Newman, G. M. Cragg, Natural Products as Sources of New Drugs from 1981 to 2014. *Journal of Natural Products* **79**, 629-661 (2016).

22. V. Viswesh, K. Gates, D. Sun, Characterization of DNA Damage Induced by a Natural Product Antitumor Antibiotic Leinamycin in Human Cancer Cells. *Chemical Research in Toxicology* **23**, 99-107 (2010).
23. G. Cassinelli, The roots of modern oncology: from discovery of new antitumor anthracyclines to their clinical use. *Tumori* **2016**, 226-235 (2016).
24. E. A. Barka *et al.*, Taxonomy, Physiology, and Natural Products of Actinobacteria. *Microbiology and Molecular Biology Reviews* **80**, 1-43 (2016).
25. A. Rayan, J. Raiyn, M. Falah, Nature is the best source of anticancer drugs: Indexing natural products for their anticancer bioactivity. *PLOS ONE* **12**, e0187925 (2017).
26. B. J. Reisman *et al.*, Apoptolidin family glycomacrolides target leukemia through inhibition of ATP synthase. *Nature Chemical Biology*, (2021).
27. J. G. Moffat, F. Vincent, J. A. Lee, J. Eder, M. Prunotto, Opportunities and challenges in phenotypic drug discovery: an industry perspective. *Nature Reviews Drug Discovery* **16**, 531-543 (2017).
28. S. Y. Van Der Zanden, X. Qiao, J. Neefjes, New insights into the activities and toxicities of the old anticancer drug doxorubicin. *The FEBS Journal* **288**, 6095-6111 (2021).
29. A. Q. Sukkurwala *et al.*, Screening of novel immunogenic cell death inducers within the NCI Mechanistic Diversity Set. *OncoImmunology* **3**, e28473 (2014).
30. D. J. Klionsky *et al.*, Guidelines for the use and interpretation of assays for monitoring autophagy. *Autophagy* **8**, 445-544 (2012).
31. L. Galluzzi *et al.*, Consensus guidelines for the definition, detection and interpretation of immunogenic cell death. *Journal for ImmunoTherapy of Cancer* **8**, e000337 (2020).
32. D. V. Krysko *et al.*, Immunogenic cell death and DAMPs in cancer therapy. *Nature reviews. Cancer* **12**, 860-875 (2012).
33. N. Casares *et al.*, Caspase-dependent immunogenicity of doxorubicin-induced tumor cell death. *Journal of Experimental Medicine* **202**, 1691-1701 (2005).
34. M. Kawano *et al.*, Dendritic cells combined with doxorubicin induces immunogenic cell death and exhibits antitumor effects for osteosarcoma. *Oncology Letters* **11**, 2169-2175 (2016).
35. A. Ribas, J. D. Wolchok, Cancer immunotherapy using checkpoint blockade. *Science* **359**, 1350-1355 (2018).
36. O. Kepp, L. Zitvogel, G. Kroemer, Clinical evidence that immunogenic cell death sensitizes to PD-1/PD-L1 blockade. *OncoImmunology* **8**, e1637188 (2019).
37. G. Sriram *et al.*, The injury response to DNA damage in live tumor cells promotes antitumor immunity. *Science Signaling* **14**, (2021).
38. D. A. Gewirtz, Cytoprotective and nonprotective autophagy in cancer therapy. *Autophagy* **9**, 1263-1265 (2013).
39. A. Yamamoto *et al.*, Bafilomycin A1 Prevents Maturation of Autophagic Vacuoles by Inhibiting Fusion between Autophagosomes and Lysosomes in Rat Hepatoma Cell Line, H-4-II-E Cells. *Cell Structure and Function* **23**, 33-42 (1998).
40. M. Michaud *et al.*, Autophagy-Dependent Anticancer Immune Responses Induced by Chemotherapeutic Agents in Mice. *Science* **334**, 1573-1577 (2011).
41. I. Martins *et al.*, Premortem autophagy determines the immunogenicity of chemotherapy-induced cancer cell death. *Autophagy* **8**, 413-415 (2012).
42. I. Novoa, H. Zeng, H. P. Harding, D. Ron, Feedback Inhibition of the Unfolded Protein Response by GADD34-Mediated Dephosphorylation of eIF2α. *Journal of Cell Biology* **153**, 1011-1022 (2001).

43. L. Bezu *et al.*, eIF2α phosphorylation is pathognomonic for immunogenic cell death. *Cell Death & Differentiation* **25**, 1375-1393 (2018).
44. H. H. Rabouw *et al.*, Inhibition of the integrated stress response by viral proteins that block p-eIF2–eIF2B association. *Nature Microbiology* **5**, 1361-1373 (2020).
45. M. Schoof *et al.*, eIF2B conformation and assembly state regulate the integrated stress response. *eLife* **10**, (2021).
46. S. Elmore, Apoptosis: A Review of Programmed Cell Death. *Toxicologic Pathology* **35**, 495-516 (2007).
47. Y. K. Dhuriya, D. Sharma, Necroptosis: a regulated inflammatory mode of cell death. *Journal of Neuroinflammation* **15**, (2018).
48. M. Murphy, James *et al.*, The Pseudokinase MLKL Mediates Necroptosis via a Molecular Switch Mechanism. *Immunity* **39**, 443-453 (2013).
49. H. Wang *et al.*, Mixed Lineage Kinase Domain-like Protein MLKL Causes Necrotic Membrane Disruption upon Phosphorylation by RIP3. *Molecular Cell* **54**, 133-146 (2014).
50. D. A. Rodriguez *et al.*, Characterization of RIPK3-mediated phosphorylation of the activation loop of MLKL during necroptosis. *Cell Death & Differentiation* **23**, 76-88 (2016).
51. K. Weber, R. Roelandt, I. Bruggeman, Y. Estornes, P. Vandenabeele, Nuclear RIPK3 and MLKL contribute to cytosolic necrosome formation and necroptosis. *Communications Biology* **1**, (2018).
52. A. L. Samson *et al.*, MLKL trafficking and accumulation at the plasma membrane control the kinetics and threshold for necroptosis. *Nature Communications* **11**, (2020).
53. L. Aaes, Tania *et al.*, Vaccination with Necroptotic Cancer Cells Induces Efficient Anti-tumor Immunity. *Cell Reports* **15**, 274-287 (2016).
54. W. Hou *et al.*, Strange attractors: DAMPs and autophagy link tumor cell death and immunity. *Cell Death & Disease* **4**, e966-e966 (2013).
55. J. I. G. Solari *et al.*, Damage-associated molecular patterns (DAMPs) related to immunogenic cell death are differentially triggered by clinically relevant chemotherapeutics in lung adenocarcinoma cells. *BMC Cancer* **20**, (2020).
56. G. Dahl, ATP release through pannexon channels. *Philosophical Transactions of the Royal Society B: Biological Sciences* **370**, 20140191 (2015).
57. J. Liu, W. Liu, J. Yang, ATP-containing vesicles in stria vascular marginal cell cytoplasms in neonatal rat cochlea are lysosomes. *Scientific Reports* **6**, 20903 (2016).
58. C. Silva-Vilches, S. Ring, K. Mahnke, ATP and Its Metabolite Adenosine as Regulators of Dendritic Cell Activity. *Front Immunol* **9**, 2581 (2018).
59. L. Apetoh *et al.*, The interaction between HMGB1 and TLR4 dictates the outcome of anticancer chemotherapy and radiotherapy. *Immunological Reviews* **220**, 47-59 (2007).
60. T. Yamazaki *et al.*, Defective immunogenic cell death of HMGB1-deficient tumors: compensatory therapy with TLR4 agonists. *Cell Death & Differentiation* **21**, 69-78 (2014).
61. D. Tang *et al.*, HMGB1 release and redox regulates autophagy and apoptosis in cancer cells. *Oncogene* **29**, 5299-5310 (2010).
62. L. Liu *et al.*, HMGB1-induced autophagy promotes chemotherapy resistance in leukemia cells. *Leukemia* **25**, 23-31 (2011).
63. X. Liu *et al.*, Calreticulin acts as an adjuvant to promote dendritic cell maturation and enhances antigen-specific cytotoxic T lymphocyte responses against non-small cell lung cancer cells. *Cellular Immunology* **300**, 46-53 (2016).

64. X. Z. Yue Li, Lijuan He, Hui Yuan, Dendritic cell activation and maturation induced by recombinant calreticulin fragment 39-272. *International Journal of Clinical and Experiemtnal Medicine*, (2015).
65. P. Espinosa-Cueto, A. Magallanes-Puebla, C. Castellanos, R. Mancilla, Dendritic cells that phagocytose apoptotic macrophages loaded with mycobacterial antigens activate CD8 T cells via cross-presentation. *PLoS One* **12**, e0182126 (2017).
66. A. D. Steele, C. N. Teijaro, D. Yang, B. Shen, Leveraging a large microbial strain collection for natural product discovery. *Journal of Biological Chemistry* **294**, 16567-16576 (2019).
67. K. E. Diggins, P. B. Ferrell, Jr., J. M. Irish, Methods for discovery and characterization of cell subsets in high dimensional mass cytometry data. *Methods* **82**, 55-63 (2015).
68. D. C. Earl *et al.*, Discovery of human cell selective effector molecules using single cell multiplexed activity metabolomics. *Nat Commun* **9**, 39 (2018).
69. D. K. Derewacz, B. C. Covington, J. A. McLean, B. O. Bachmann, Mapping Microbial Response Metabolomes for Induced Natural Product Discovery. *ACS Chem Biol* **10**, 1998-2006 (2015).
70. R. Subramani, W. Aalbersberg, Culturable rare Actinomycetes: diversity, isolation and marine natural product discovery. *Appl Microbiol Biotechnol* **97**, 9291-9321 (2013).
71. H. K. Kumar *et al.*, Genomic characterization of eight Ensifer strains isolated from pristine caves and a whole genome phylogeny of Ensifer (Sinorhizobium). *J Genomics* **5**, 12-15 (2017).
72. P. Rangseekaew, W. Pathom-Aree, Cave Actinobacteria as Producers of Bioactive Metabolites. *Front Microbiol* **10**, 387 (2019).
73. B. C. Covington, J. A. McLean, B. O. Bachmann, Comparative mass spectrometry-based metabolomics strategies for the investigation of microbial secondary metabolites. *Nat Prod Rep* **34**, 6-24 (2017).
74. C. R. Goodwin *et al.*, Structuring Microbial Metabolic Responses to Multiplexed Stimuli via Self-Organizing Metabolomics Maps. *Chem Biol* **22**, 661-670 (2015).
75. P. O. Krutzik, G. P. Nolan, Fluorescent cell barcoding in flow cytometry allows high-throughput drug screening and signaling profiling. *Nature Methods* **3**, 361-368 (2006).
76. P. O. Krutzik, M. R. Clutter, A. Trejo, G. P. Nolan, Fluorescent Cell Barcoding for Multiplex Flow Cytometry. *Current Protocols in Cytometry* **55**, (2011).
77. B. J. Reisman, S. M. Barone, B. O. Bachmann, J. M. Irish, DebarcodeR increases fluorescent cell barcoding capacity and accuracy. *Cytometry Part A*, (2021).

CHAPTER 2 – An Immunogenic Module for Natural Product Drug Discovery using the Multiplexed Activity Metabolomics Platform

2.1 Introduction

Small molecule anti-cancer agents are typically discovered via high-throughput target-based approaches or untargeted cytotoxicity screens that reflect essential cellular processes such as DNA replication, cytoskeletal remodeling, and metabolism. Compounds from both discovery paradigms are well represented in the clinic by synthetic compounds and natural products (*1*). For example, imatinib is a synthetic drug developed to treat chronic myelogenous leukemia by blocking nucleotide triphosphate binding pockets of tyrosine kinases, notably BCR/ABL, to stabilize inactive state complexes and prevent downstream signaling (*2*). Anthracyclines and taxanes, initially discovered via cytotoxicity assays, were later observed to interfere with DNA replication and microtubule stability, respectively (*3, 4*). Imatinib, anthracyclines, and taxanes are all featured in the World Health Organization's list of essential medicines, underlining the complementarity of target based and phenotypic discovery modes (*5*).

In addition to tumor toxicity, some chemotherapeutics are thought to be effective because they trigger immunogenic cell death (ICD). ICD is a property of moribund cells that elicits inflammation towards a therapeutically productive adaptive antitumor immune response (*6, 7*) and can instigate more durable treatments or act as an adjuvant to immunotherapy. Notably, combining inflammatory agents inducing live and/or dying cell ICD with checkpoint blockade therapy has been shown to enhance survival in animal models (*8-12*). Examples of studied ICD inducers include widely used chemotherapies, such as the anthracycline daunorubicin, peptide actinomycin D, podophyllotoxin teniposide, and platinum-based antineoplastic oxaliplatin (*6, 13-16*). ICD can activate both innate and adaptive immune responses via expression of damage associated

molecular patterns (DAMPs) including secretion of ATP, release of nuclear protein HMGB1, and surface exposure of endoplasmic reticulum resident protein calreticulin (eCRT) to name a few (*17*). These immunogenic DAMPs comprise 'find me' and 'eat me' signals that trigger recruitment and activation of antigen presenting cells, such as dendritic cells and macrophages, that initiate antigen-specific immune responses (*17*).

Recently, the phenomenon of chemically induced anti-tumor immunity has been broadened to include living cells. In these processes, live injured cells may present DAMPs that stimulate innate and adaptive immunity independent of previous ICD hallmarks, suggesting that additional modes of immunogenic induction remain to be discovered. Herein the term "immunogenic cell injury" (ICI) is used to refer to all types of immunogenic injury responses in injured or dying cancer cells. Based on these and prior studies (*18-20*), it is apparent that the various forms of chemically induced cell death and injury do not yield comparable immunogenic responses. There is a gap in understanding how cell death and injury pathways connect to the display of DAMPs that elicit therapeutically productive immune responses. Thus, an injury cytometric module composed of fluorescent antibodies that detect molecular injury and stress markers was developed.

To expedite the discovery of immunogenic small molecule therapies, the injury module was designed to be compatible with fluorescent cell barcoding (FCB), to enhance sample throughput, and validated on next generation spectral flow cytometers, to broaden detection of molecular injury signals. A multiplexed activity metabolomics (MAM) approach is employed here to establish correlations between intracellular injury and extracellular DAMP exposure induced by natural products, or natural product derivatives. The topoisomerase poison etoposide is an effector molecule that induces DNA double strand breaks detected by phosphorylation of H2AX variant at serine 139 (γH2AX) and has been shown as an adjuvant signal to immunogenicity (*12*). The pan-

kinase alkaloid inhibitor staurosporine, a potent apoptotic agent, prompts cleavage of the caspase-3 zymogen to its active form (cCAS3) (Table 1.1) (*21*). Apoptotic activation is required for doxorubicin induced immunogenicity (*6*). Likewise, autophagy and the unfolded protein response are known to be critical signals for assessing immunogenic potential and are required for ICD (*10, 22*). The autophagy marker LC3 or UPR marker p-EIF2α are specifically inducible with the vacuolar H^+-ATPase (v-ATPase) inhibitor bafilomycin (*23-25*) or SERCA inhibitor thapsigargin, respectively (*26-28*). An alternative, explosive form of cell death known as necroptosis has also gained traction as an immunogenic signal dependent on the RIPK-MLKL signaling pathway and can be detected by p-MLKL. The benzimidazole natural product-inspired molecule nocodazole disrupts microtubule dynamics to retain intracellular p-MLKL to appreciable levels of detection (*29*) and inhibits M-phase measured by expression of p-HH3 at serine 28 (Table 2.1) (*21*).

The complete injury module was applied to aid identification of natural products that bias signaling pathways towards an immunogenic fate. The benchmark bioactive secondary metabolites are evaluated with multiplexed activity profiling (MAP) to identify optimal dose and timing for cell death and injury pathways preceding ICI mediated DAMP induction (*30-33*) and then correlated to immunogenic hallmarks calreticulin, ATP, and HMGB1 by principal component analysis. Benchmark compounds bafilomycin A1, staurosporine, and nocodazole were spiked into an inert metabolic extract and fractioned into plate wells to detect compound-specific activity in the presence of cellular and expired media components (*21*) with the ICI module. Following successful validation, the module was applied using MAP and MAM workflows to identify bioactive metabolites in five untested microbial extracts generated from hypogean actinomycetes, demonstrating the insensitivity of the module to fermentation product interference, and resulting in the discovery of an unexpected injury response profile of the secondary metabolite narbomycin

(*34*), produced by a streptomyces.

The ICI module coupled with fluorescent cell barcoding and viability stain established a ten-color (six ICI, one viability, three barcode) flow cytometry panel that performs 336 individual assays per run (seven functional markers across 48 plate wells). Secondary assays measured the expression of known immunogenic DAMPs: ATP, HMGB1, and eCRT. Assessing injury patterns in microtiter wells with millions of individual cells and comparing them to well characterized benchmark injury control compounds provide insights into the connection between patterns and immunogenicity and affords a discovery platform for compounds that induce ICI hallmarks.

2.2 Results

2.2.1 Antibody validation for UPR and necroptotic markers

To validate phospho-specific antibodies for the ICI module, chemical induction was used to measure injury phenotype in fixed cells following 10 μM challenge for 24 hours in a five-color panel (Figure 2.1A). Vehicle treated cells served as negative control and were labeled with Ax750 fluorescent dye. Etoposide treated cells were included as a positive control for chemical specific duction of DNA damage response sensor γH2AX and labeled with pacific orange fluorescent dye (Figure 2.1A). The γH2AX signal was detected with a fluorescently conjugated mouse primary antibody (Table 2.2). Cell populations challenged with the terpenoid thapsigargin or benzimidazole derivative nocodazole were labeled independently with pacific blue dye and

Compound	Company	Catalog number	Phenotype
Bafilomycin A1	Selleckchem	S1413	Autophagy
Etoposide	Selleckchem	S1225	DNA damage
Nocodazole	Selleckchem	S2775	Mitosis, necroptosis
Staurosporine	Selleckchem	S1421	Apoptosis
Thapsigargin	Selleckchem	S7895	UPR

Table 2.1. Reagents and biometric readouts.

evaluated for UPR and necroptotic signal induction respectively (*10, 29, 35, 36*). Flow cytometry validated antibodies for these ICI signals were unavailable, thus antibodies applied in other techniques (Table 2.1) were utilized to observe chemically induced injury signals. These two markers were targeted with phospho-specific unconjugated rabbit primary antibodies and detected with a fluorescent goat secondary antibody specific to rabbit Fc IgG (Figure 2.1A and Table 2.2). Separate thapsigargin or nocodazole challenged cell populations were mixed with etoposide and vehicle challenged cells and then stained for the ICI marker of interest for detection with a spectral flow cytometer. Cells were gated as viable-singlets and isolated to drug challenged populations by their fluorescent dye label (Figure 2.1B and Figure 2.2). Thapsigargin and nocodazole challenged cells exhibited a right-shifted cell population that was quantified as percent in gate for positive secondary fluorescent antibody signal and compared to etoposide and vehicle controls (Figure 2.1D-G). Positive signal was also compared to a fluorescent secondary control that was absent of primary antibody to confirm measured biological responses was not due to non-specific binding of the fluorescent goat secondary (Figure 2.3). Neither etoposide nor vehicle activated UPR or necroptotic injury signals (Figure 2.1). Moreover, etoposide treated cells were γH2AX positive, while γH2AX levels in thapsigargin and nocodazole challenged populations remained unchanged (Figure 2.4).

Next, the two validated ICI flow antibodies required fluorescent functionalization and confirmation that fluorescent modifications did not abolish target binding. Antibodies targeting p-EIF2α and p-MLKL were fluorescently conjugated with covalent, primary amine reactive Alexa Fluor dyes (Figure 2.1A). Conjugation efficiency was evaluated by fluorescence SDS-PAGE in reducing and non-reducing conditions and exhibited fluorescent signal at molecular weights of 150 kDa, 50 kDa, and 25 kDa consistent with full length, heavy chain, and light chain rabbit antibody

molecular weights (Figure 2.5). Detection of p-EIF2α and p-MLKL were repeated and confirmed covalent modifications of antibodies did not ablate target binding (Figure 1).

2.2.2 Multiplexed Activity Profiling rapidly screens for injury responses in leukemia cell lines

With validated ICI module antibodies in hand, multiplexed activity profiling (MAP) was used to rapidly screen three leukemia cell lines to identify adequate concentrations and challenge times for reliable ICI induction (Figure 2.6 and Figure 2.7) with the compounds bafilomycin A1, etoposide, of nocodazole, staurosporine, and thapsigargin (*21*, *23*, *25*, *36*) (Table 2.1). Heterogeneic leukemia model cell types K562 (chronic myelogenous leukemia), MV-4-11 (B-myelomonocytic leukemia), and Jurkat (T cell leukemia) cells were challenged with 10 uM, 1 uM, .1 uM, and .01 uM of each compound for 4, 24, and 48 hours (Figure2.6A). At each timepoint cells were fixed, permeabilized, fluorescently barcoded, and stained with the ICI module for flow

Reagent	Detect	Clone	Fluorophore	Manufacturer	Catalog number	Validation Panel	Injury Module
Antibody	LC3	D3U4C	Ax488	Cell Signaling Technology	13082		X
Antibody	γH2AX	N1-431	Percp-Cy5.5	BD Biosciences	564718	X	X
Antibody	cCAS3	C92-605	PE	BD Biosciences	550822		X
Antibody	p-MLKL	D6H3V	Ax568	Cell Signaling Technology	91689		X
Antibody	p-HH3	HTA28	Pe-Cy7	Biolegend	641011		X
Antibody	p-EIF2α	119A11	Ax647	Cell Signaling Technology	3597		X
Antibody	Rb FC		Ax488	Invitrogen	A11-034	X	
NHS dye	Primary amines		Pacific Blue	ThermoFisher Scientific	P10163	X	X
NHS dye	Primary amines		Pacific Orange	ThermoFisher Scientific	P30253	X	X
NHS dye	Primary amines		Ax750	ThermoFisher Scientific	A20011	X	X
NHS dye	Primary amines		Ax700	ThermoFisher Scientific	A20010	X	X
Antibody	Calreticulin	D3E6	PE	Cell Signaling Technology	19780		
AnnexinV	Phosphatidylserine		FITC	Cell Signaling Technology	6592S		
Vital Dye	Nucleic acids		DAPI	Cell Signaling Technology	4083S		
Conjugation kit	Primary amines	D6H3V	Alexa 568	ThermoFisher Scientific	A20184		
Conjugation kit	Primary amines	119A11	Alexa 647	ThermoFisher Scientific	A20186		

Table 2.2. Flow cytometry reagents.

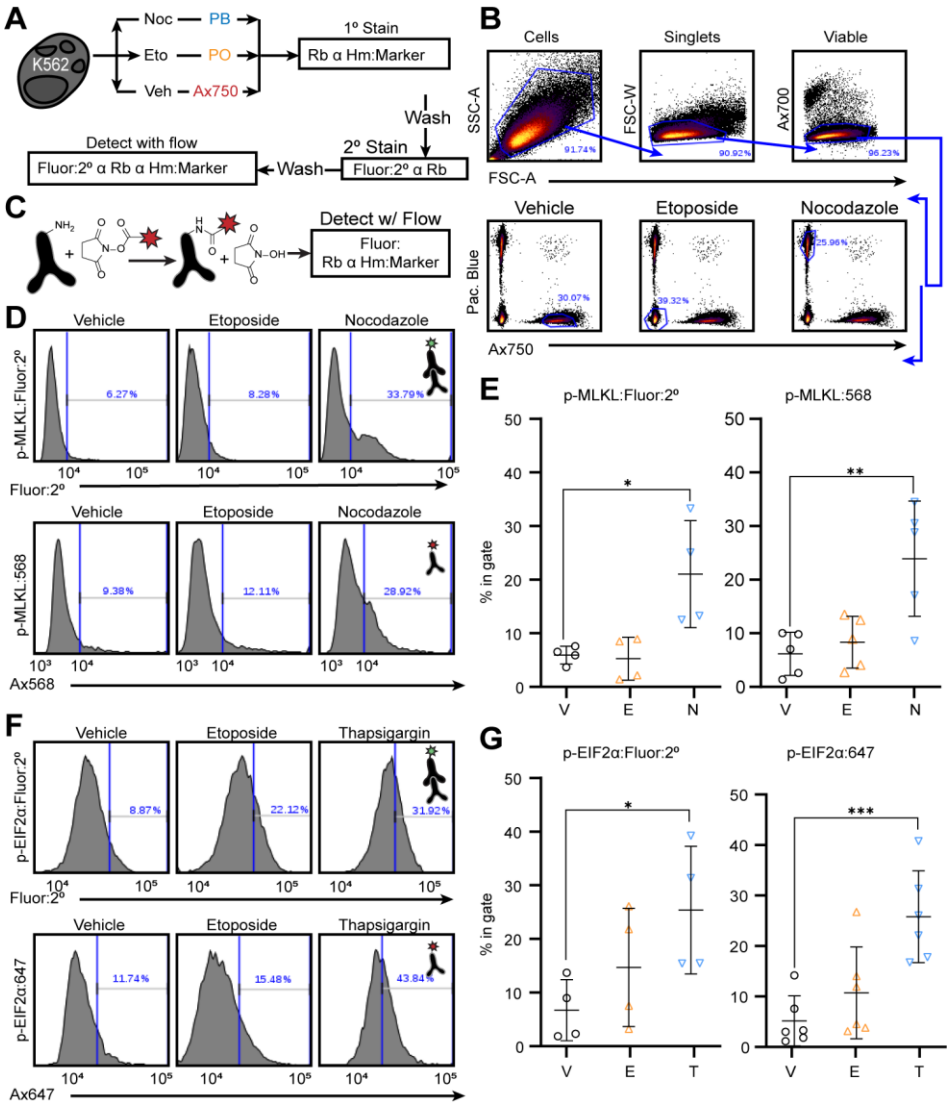

Figure 2.1 Multiplexed activity validation evaluates antibody fidelity by biological signal. (A) Experimental scheme for measuring chemically induced cell phenotypes by barcoded chemical induction conditions in mixed samples with a marker specific antibody raised in rabbit and a rabbit specific fluorescent secondary antibody. (B) Gating strategy for signal deconvolution to assess challenge specific responses. Cells were treated for 24 hours with 10 µM nocodazole or etoposide and vehicle control. After trea tment, cells were viability stained, fixed, permeabilized, and fluorescently labelled by NHS-functionalized fluorescent dyes by compound: Nocodazole - Pacific Blue, Etoposide - Pacific Orange, Vehicle - Ax750. Viable singlet cells were isolated to compound specific population by matched fluorescent signal to distinguish chemically induced cell phenotypes. (C) Conjugation reaction of NHS-functionalized fluorescent dyes to primary amines in antibody peptide sequence for single step marker detection. (D) Representative fluorescent intensity plots of p-MLKL detection with a fluorescent secondary antibody (left) and p-MLKL conjugated to Ax568 (right). (E) Histograms show chemically induced fluorescent signal measured as percent in gate mean ± S.D (n = 4, One way ANOVA with Dunnett's multiple comparisons test) of p-MLKL detection with fluorescent secondary (left) or p-MLKL:568 (right). (F) Procedure in A-C were repeated for p-EIF2α directed antibody with the exception of natural product (thapsigargin) and conjugate fluorophore (Ax647). Representative fluorescent intensity plots of p-EIF2α detection with a fluorescent secondary antibody (left) and p-EIF2α conjugated to Ax647 (right). (G) Histograms show chemically induced fluorescent signal measured as percent in gate mean ± S.D (n = 6, One-way ANOVA with Dunnett's multiple comparisons test) of p-EIF2α detection with fluorescent secondary (left) or p-EIF2α:647 (right). *p* < **.05*, ***.01*, ****.001*, *****.0001*; V = Vehicle, E = Etoposide, N = Nocodazole, T = Thapsigargin

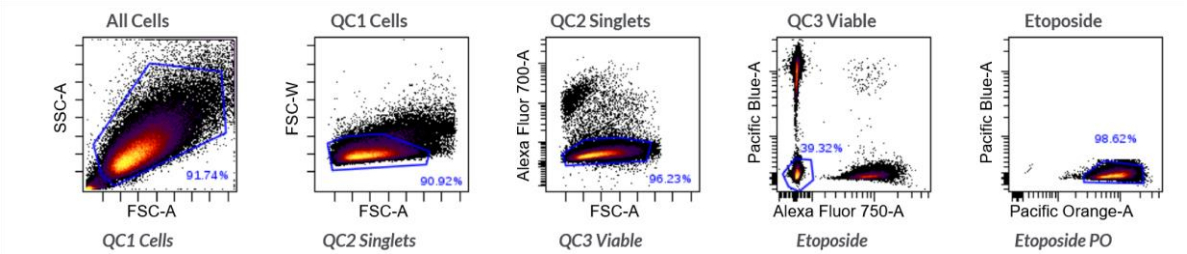

Figure 2.2. Gating strategy for signal deconvolution to assess challenge specific responses. (A) Cells were treated for 24 hours with 10 µM nocodazole or etoposide and vehicle control. After treatment, cells were viability stained, fixed with paraformaldehyde, permeabilized with methanol, and fluorescently coded by NHS-functionalized fluorescent dyes by compound: Nocodazole-Pacific Blue, Etoposide-Pacific Orange, Vehicle-Ax750. Viable-singlet cells were isolated to compound specific population by matched fluorescent signal to distinguish chemically induced cell phenotypes. Double negative Pacific Blue and Ax750 population gated from QC3 viable into etoposide gate. Positive Pacific Orange cells were gated and interpreted as the etoposide challenged cell population.

cytometry. Following data acquisition, samples were quality control gated and debarcoded to evaluate single responses (Figure 2.6B). Each leukemia cell line exhibited unique injury profiles to each challenge condition over time (Figure 2.6C and Figure 2.7) and thus evaluated for the clearest marker responses.

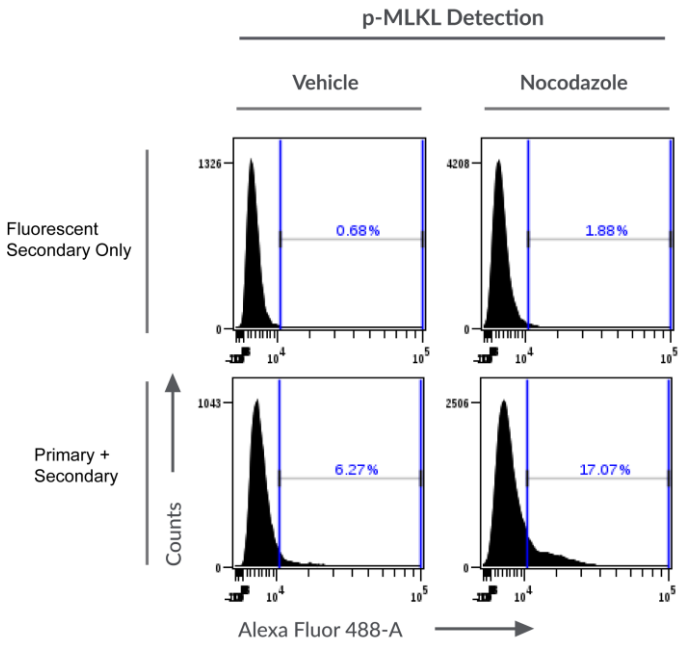

Figure 2.3. Challenged samples stained with fluorescent secondary antibody alone do not exhibit positive signal.

2.2.3 Autophagy marker LC3 is induced by bafilomycin A1 in leukemia models

The three tested leukemia cell lines were all sensitive to LC3 induction by the nanomolar v-ATPase inhibitor bafilomycin A1 across time points and concentrations consistent with literature reports (31-33). MV-4-11 were sensitive to LC3 expression by all compounds at all doses, except for 10 nM nocodazole after 48-hour challenge (Figure 2.7B). LC3 levels in Jurkat were less pronounced but present in bafilomycin A1 and etoposide treatment conditions (Figure 2.7A). The K562 cell line also experienced autophagic flux most prominently in bafilomycin A1 challenge conditions with some activity observed in thapsigargin challenged populations through 24 hours

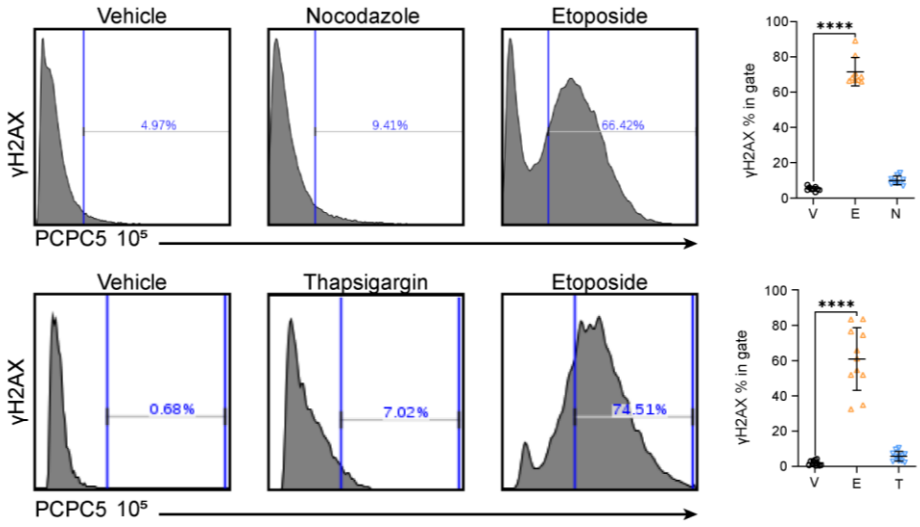

Figure 2.4. Representative fluorescent intensity plots of γH2AX detection following chemical challenge. (A) Representative fluorescent intensity plots for γH2AX that complement figure 1D. Cell populations challenged with 10 µM etoposide, nocodazole, or vehicle equivalent for 24 hours. Cells were then viability stained, fixed with paraformaldehyde, permeated with methanol, and fluorescently coded: Pacific Blue – Nocodazole, Pacific Orange – Etoposide, and Alexa fluor 750 – Vehicle. Coded cells were pooled, stained, flowed, and gated as in Fig. 1 and SF. 1 then evaluated for γH2AX response with a primary antibody conjugated to fluorescent PerCp-Cy5.5 (PCPC5). Signal positive cells were interpreted as percent positive cells in gate (cells to the right of vertical blue bars). Etoposide induced γH2AX DNA damage response in challenged cell populations. Nocodazole and vehicle failed to elicit an injury response. Scatter plots represent the mean percent in gate ± S.D (n = 4, One-way ANOVA with Dunnett's multiple comparisons test) of γH2AX detection. **(B)** Representative fluorescent event counts for γH2AX. Cells were processed and stained as in A with the exception of thapsigargin challenged cells in hanks balanced salt solution were stained with Pacific Blue. Gating and analysis for γH2AX was performed as described above. Scatter plots represent percent in gate mean ± S.D. (n = 6, One-way ANOVA with Dunnett's multiple comparisons test) of γH2AX signal. $p <$ ****.001. V = Vehicle, E = Etoposide, N = Nocodazole, T = Thapsigargin.

(Figure 2.6C). Unlike MV-4-11 and Jurkat, K562 cells did not exhibit elevation of autophagy marker LC3 via off-target compounds and signaling cross talk, but rather remained largely restricted to induction by bafilomycin A1 inhibition of v-ATPase (Figure 2.6D and Figure 2.7).

Since K562 cells best conserved on-target signal specificity over time they were subjected to additional testing to confirm positive assay performance. Challenge with 1 µM bafilomycin A1 significantly elevated LC3 levels in 4 hours and continued signal elevation through 24- and 48-hour timepoints (Figure 2.6D). Additionally, 1 µM thapsigargin increased LC3 after 24- and 48-hour challenge. The thapsigargin induced LC3 phenotype is potentially due to increased autophagy to compensate for enduring ER strain (Figure 2.6D) (39, 83) whereas bafilomycin A1 enhances LC3 levels by inhibiting acidification of LC3 associated autophagic compartments which prevents degradation of the marker and increases its abundance over time (*23, 24*). Thus, positive LC3 signal of unknown compounds may be attributed to inhibition or activation of autophagy and

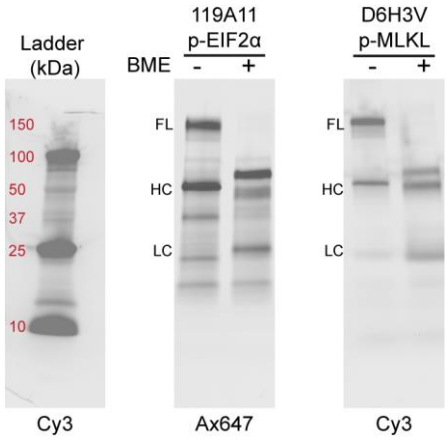

Figure 2.5. Fluorescent intensity of conjugated antibody evaluated by SDS-PAGE in-gel fluorescence. Spin column purified rabbit antibodies were harvested and incubated with specified antibody labeling kit in 100 µL volume of 100 mM sodium bicarbonate for 1 hour in the dark with mixing. Excess dye was removed by purification resin provided by the manufacturer. Antibodies were prepared in Tris/SDS/Glycine running buffer and Laemmli sample buffer +/- BME, loaded onto a 4 – 20 % Tris/Glycine gel and electrophoresed for 30 minutes at 150 volts. All lanes were run on the same gel and imaged simultaneously with Cy3 and Ax647 filters as indicated. Multichannel blot was converted to grayscale, color inverted, and scaled for contrast. The gel was exported and cropped such that relative band position in the raw image was maintained. 119A11 and D6H3V represent respective antibody clones to detect the maker indicated. FL = Full length (150 kDa), HC = Heavy Chain (50 kDa), LC = Light Chain (25 kDa)

require deeper molecular investigation.

Staurosporine and thapsigargin challenge also increased LC3 injury signal by 24- and 48-hours while etoposide and nocodazole failed (Figure 2.6D). The results in Figure 2.6D confirm the bafilomycin A1 induced LC3 phenotype observed in Figure 2.6C and supports staurosporine and thapsigargin signal observed at 1 uM dose at 48 hours (Figure 2.6C-D). Etoposide and nocodazole failed to induce LC3 at 1 µM challenge over 48 hours suggesting the heatmap signal intensity in

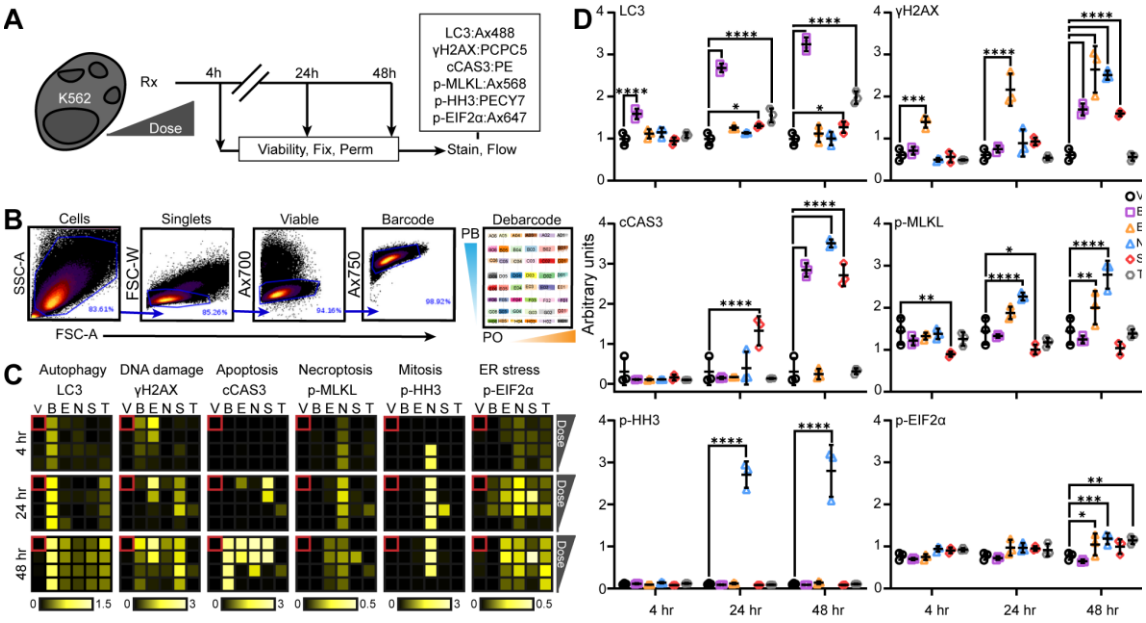

Figure 2.6. Multiplexed activity profiling of cell injury across dose and time. (A) K562 cells were dosed with six compounds from 10 µM to 10 nM by ten-fold serial dilution. Each timepoint, 4, 24, and 48 hours, were viability stained, fixed, permeabilized and fluorescently barcoded. Sets of 48 barcoded wells were pooled by timepoint then stained with a fluorescent antibody cocktail to measure individual well responses to each fluorescent injury signal simultaneously with flow cytometry. (B) Cells were gated as viable-singlets stained with NHS-functionalized Ax750 cell uptake control dye. Cells were then debarcoded, digitally reassigned to origin wells to assess well-by-well marker responses (LC3 = apoptosis, γH2AX = DNA damage, cCAS3 = apoptosis, p-MLKL = necroptosis, p-HH3 = M-phase, p-EIF2α = UPR). (C) Multiplexed activity profiling of injury signals induced by small molecules is represented by a heat map of the 95th percentile of the arcsinh ratio to vehicle control well outlined in red. (D) Compound specific, time dependent injury at 1 µM challenge revealed nascent temporal relationships among injury phenotypes imposed by secondary metabolites with specific mechanisms of action. Raw 95th percentile of fluorescent, marker intensity was graphed as histograms of mean ± S.D and tested for significance against vehicle control of respective timepoints (n = 3, Two-way ANOVA with Dunnett's multiple comparison's test). p < *.05, +.01, % .001, $ .0001; V = Vehicle, B = Bafilomycin A1, E = Etoposide, N = Nocodazole, S = Staurosporine, T = Thapsigargin, PB = Pacific Blue, PO = Pacific Orange

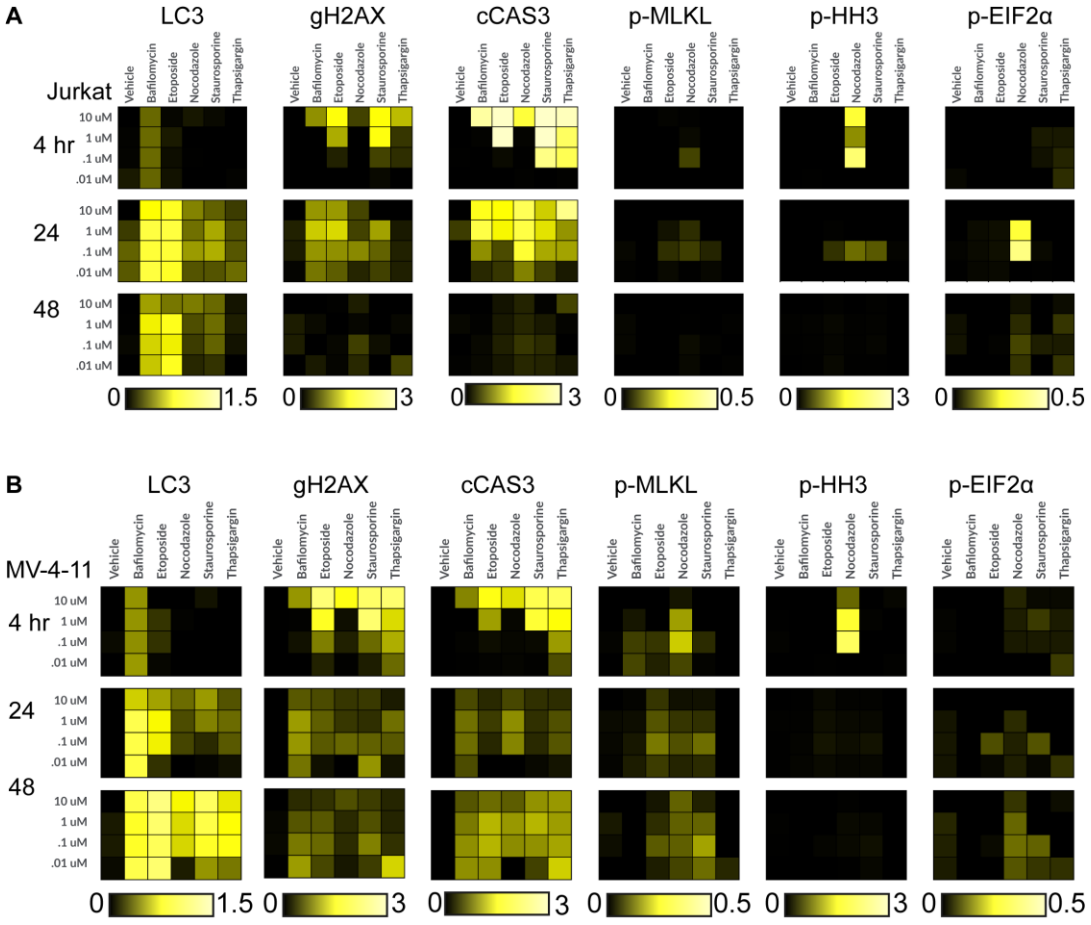

Figure 2.7. Multiplexed activity profiling (MAP) of cell injury across dose and time. Jurkat and MV-4-11 cells were dosed with 5 compounds from 10 µM to 10 nM by $\log_{10}$ dilution and vehicle control. Each timepoint, 4, 24, and 48 hours, were viability stained, fixed with paraformaldehyde, permeabilized with methanol, and fluorescently barcoded. Sets of 48 barcoded wells were pooled by timepoint then stained with a fluorescent antibody cocktail to measure individual well responses to each fluorescent injury signal simultaneously with flow cytometry. MAP of Jurkat and MV-4-11 cell lines for chemically induced ICI to complement Figure 3C. **(A)** Multiplexed activity profiling of injury signals in Jurkat induced by secondary metabolites is represented by a heat map of the 95th percentile of the arcsinh ratio to vehicle control wells. **(B)** Multiplexed activity profiling of injury signals in MV-4-11 induced by secondary metabolites is represented by a heat map of the 95th percentile of the arcsinh ratio to vehicle control wells.

Figure 2.6C was not biologically significant.

2.2.4 DNA damage is triggered by direct and indirect molecular mechanisms

Jurkat γH2AX expression was most notable in etoposide and staurosporine treatments at 4 hours with apparent stress resolution by 48 hours (Figure 2.7A). A similar phenomenon was

observed in MV-4-11 cells (Figure 2.7B). On the other hand, K562 cells presented a direct DNA damage response over time when challenged with 10 µM and 1 µM of the topoisomerase inhibitor etoposide and also responded indirectly to staurosporine in a dose dependent fashion and increased marker response from 24 to 48 hours (Figure 2.6D). The K562 DNA damage phenotype that was maintained through 48 hours was confirmed with a 1 µM challenge over 48 hours (Figure 2.6D). Etoposide successfully induced DNA damage at all timepoints (Figure 6). Additionally, enhanced γH2AX levels were observed with non-DNA damaging bafilomycin A1, nocodazole, and staurosporine following 48-hour challenge suggesting autophagy inhibition, microtubule catastrophe, and prolonged kinase blockade can yield double stranded breaks via indirect molecular mechanisms if the stress is not resolved by 48 hours (Figure 2.6D).

2.2.5 Apoptosis can be elicited by prolonged secondary metabolite challenge

Jurkat and MV-4-11 cells were sensitive to cCAS3 induction at 4 hours by all compounds, particularly staurosporine and thapsigargin at nanomolar concentrations (Figure 2.7). Increased sensitivity to apoptotic induction over 48 hours resulted in diminished cCAS3 activity as an artifact

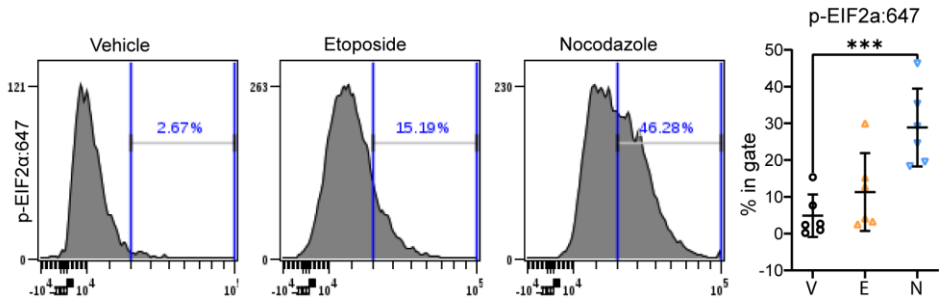

Figure 2.8. **Detection of p-EIF2α following nocodazole challenge in K562 cell line.** Cells were treated for 24 hours with 10µM nocodazole or etoposide and vehicle control. After treatment, cells were viability stained, fixed with paraformaldehyde, permeabilized with methanol, and fluorescently coded by NHS-functionalized fluorescent dyes by compound: Nocodazole-Pacific Blue, Etoposide-Pacific Orange, Vehicle-Ax750. Viable-singlet cells were isolated to compound specific population by matched fluorescent signal to distinguish chemically induced cell phenotypes. Nocodazole induction of p-EIF2α shown as percent in gate following QC gating scheme as in Fig 1. Scatter plots of percent in gate mean ± S.D (n = 6, One-way ANOVA with Dunnett's multiple comparisons test) ***$p<.01$. V = Vehicle, E = Etoposide, N = Nocodazole

of viable cell loss by gating (Figure 2.6B) rather than stress resolution (Figure 2.7). The K562 cells manifested a staurosporine specific cCAS3 phenotype in response to dose at 24 hours and maintained this phenotype through 48 hours (Figure 2.6D). At 48 hours bafilomycin A1, etoposide, and nocodazole initiated cCAS3 response suggesting prolonged cellular stress of autophagy, DNA double strand breaks, or microtubule disruption will engage the apoptotic death effector pathway in K562 cell model (Figure 2.6D). Due to the staurosporine specific cCAS3 phenotype observed at 24 hours and overall resilience to enduring chemical challenge accompanied by a cCAS3 phenotype (Figure 2.6D), the K562 line was subjected to 1 µM time course challenge to confirm MAP screening results. The pan-kinase inhibitor staurosporine increased cCAS3 signal to biologically significant levels at 24 and 48 hours (Figure 2.6D). Bafilomycin A1 and nocodazole cCAS3 induction was also apparent by 48 hours keeping with initial screening data (Figure 2.6C) and suggest extended challenge with secondary metabolites may reveal additional pro-apoptotic chemical agents with biorthogonal molecular targets.

2.2.6 Necroptotic marker p-MLKL is sensitive to induction by nocodazole

Nocodazole challenged K562 displayed escalated levels of the necroptotic effector p-MLKL across time points and doses (Figure 2.6D). The necroptotic marker p-MLKL was amplified by nocodazole challenge at 24 hours and 48 hours (Figure 2.6D) in line with validation (Figure 2.1D-E) and initial screening (Figure 2.6C). Etoposide also stimulated p-MLKL presentation following 48-hour challenge (Figure 2.6D). It is important to consider nocodazole challenged cells with enhanced p-MLKL is likely not necroptotic death but rather an accumulation of intracellular p-MLKL that fails to translocate from the nucleus to other cellular compartments over time due to nocodazole induced microtubule catastrophe (*37, 38*). Notably, staurosporine inhibited p-MLKL signal at 4 and 24 hours with signal recovery by hour 48 (Figure 2.6D) which

may be the result of crosstalk between apoptotic and necroptotic signaling pathways (*39, 40*). Jurkat and MV-4-11 were more sensitive to induction of apoptotic effector cCAS3 than necroptotic effector p-MLKL (Figure 2.7) and reflect cell type specific responses with respect to leukemia subtypes.

2.2.7 Thapsigargin and nocodazole induce UPR signal p-EIF2α

The UPR marker p-EIF2α was activated in K562 cells by thapsigargin consistent with SERCA inhibition (*26-28*) while Jurkat and MV-4-11 cells remained unresponsive and inconsistent with dosing (Figure 2.6 and Figure 2.7). In line with Figure 2.1 validation data and Figure 2.6C screening data, 1 μM thapsigargin induced p-EIF2α after 48-hour challenge in K562 (Figure 2.6D). Nocodazole and etoposide also increased UPR marker p-EIF2α to statistically significant values in 48-hour challenge conditions (Figure 2.6D). The observed p-EIF2α activation phenotype in nocodazole treated cells was unexpected and not previously reported, thus nocodazole challenge was repeated as in Figure 1 to confirm nocodazole does impart a statistically significant increase in p-EIF2α in K562 (Figure 2.8). It is also worth noting that bafilomycin A1 promoted LC3 and failed to enhance p-EIF2α in contrast to thapsigargin activating p-EIF2α and LC3. This observation indicates that ER strain may indirectly activate autophagy to compensate for cellular energetic requirements and that the UPR is unresponsive to autophagy inhibition in this model system (Figure 2.6D).

In all, MAP screening provided a high-throughput and robust format for confirming panel fidelity and identification of chemically sensitive cell lines. The initial MAP screen in Figure 6 and 7 indicated Jurkat and MV-4-11 were more sensitive to injury by inhibition of molecular targets outside canonical signaling pathways (e.g., thapsigargin activates cCAS3 in Figure 2.7). K562, however, first activated injury signals consistent with molecular inhibition of specific

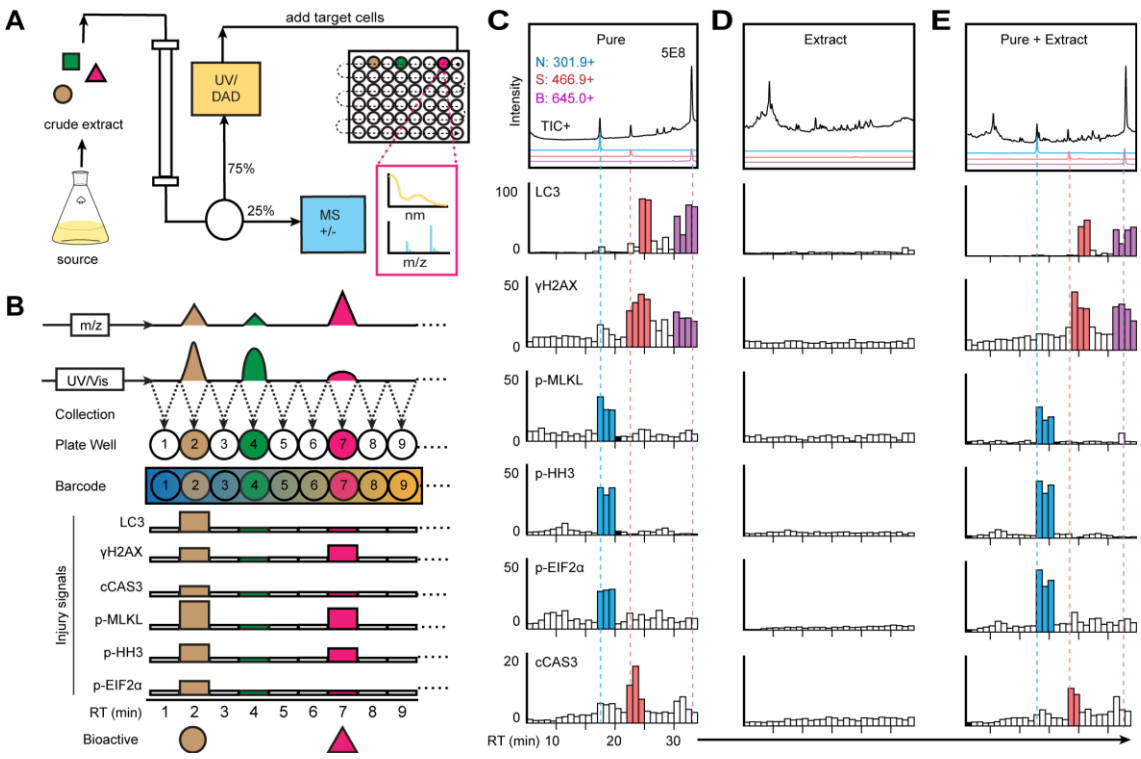

Figure 2.9. Multiplexed activity metabolomics aligns bioactivity with mass spectra. (A) HPLC/MS fractionation of crude metabolomic extracts by reverse phase, split flow HPLC/UV/MS with polarity switching mass scanning to associate metabolite spectral data to well eluates by retention time. Collected metabolic fractions were lyophilized and plated under cell containing culture media. (B) Cells were fluorescently barcoded to origin wells, pooled, and stained with fluorescent antibody cocktail. Barcode and biological signal were detected for all wells simultaneously by flow cytometry. Cells were debarcoded to original well positions and evaluated for well-specific signal. (C) Proof of principle signal detection of pure, known bioactive components on inert metabolomic sample. Pure compounds induced bioactive signal in plate wells aligned to mass spectra by retention time. (D) Extract only displays no significinact bioactivity. (E) Pure compounds mixed with inert extract exerted bioactivity in wells containing known compounds and repeated bioactivity of pure compounds shown in C. Positive ion currents and correlated well activity is distinguished by color. N = Nocodazole (m/z ,301.9 [M+1]+), blue. S = Staurosporine (m/z 466.9 [M+1]+), red. B = Bafilomycin A1 (m/z 645.0 [M+1]+), purple.

targets prior to exerting off-target injury phenotypes (Figure 2.6). The consistency and reliability of chemically induced K562 injury signals offered a model for unraveling ICI biomarker relationships to ICD signals in leukemia models.

2.2.8 Multiplexed Activity Metabolomics aligns injury phenotypes to bioactive compounds

The MAM discovery workflow is a system for overlaying multiplexed single cell chemical biological measurements onto characterized metabolomic arrays. Metabolomic extracts are

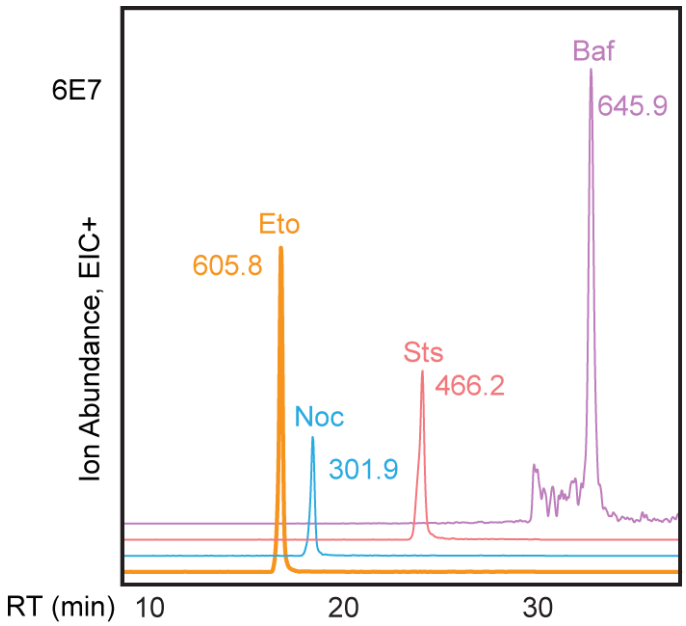

Figure 2.10. EIC+ traces from single, independent compound injections. Orange = Etoposide, 605.8 $[M + H]^+$, Blue = Nocodazole, 301.9 $[M + H]^+$, Red = Staurosporine, 466.2 $[M + H]^+$, Purple = Bafilomycin A1, 645.9 $[M + H]^+$. RT = retention time in minutes. The retention times of nocodazole, staurosporine and bafilomycin A1 indicated these compounds would not elute into the same wells. Etoposide and nocodazole retention times may have resulted in multiple compounds in a single well, thus etoposide was excluded from pure compound injections.

chromatographically fractionated by high performance liquid chromatography (HPLC). One part of the eluate is diverted to MS and three parts are diverted to UV/Vis and collected in 96 well microtiter plates. Each plate well contains one-minute fractions of eluate that correspond to retention times of collected MS/UV/Vis spectra (Figure 2.9A). Fractioned metabolomes are dried *in vacuo* and resuspended in culture media with cells and incubated at 37 °C. Each well population is fixed, permeabilized, barcoded, pooled, stained with the fluorescent ICI module and acquired on Cytek spectral flow cytometer for downstream analysis of biological signal. Plate wells with bioactivity are referred to the corresponding spectra to identify potentially bioactive metabolite(s) by correlation of negative and/or positive electrospray *m/z* and UV/VIS peaks with immunoassay

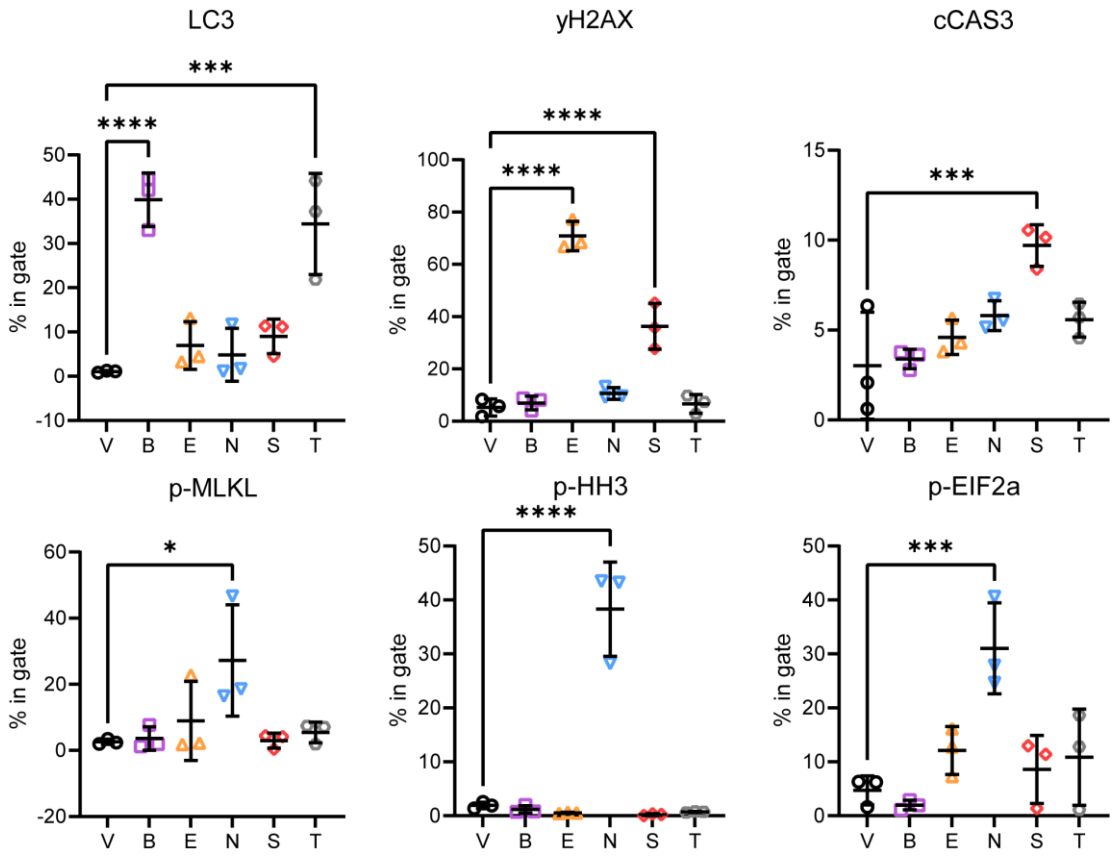

Figure 2.11. Marker signal shown as percent in gate of manually added MAM control compounds across three test plates. To each MAM experiment, control compounds are added to known wells and processed along with experimental wells. Following debarcoding, control wells are evaluated for bioactivity to control for run-to-run variation and serve as a benchmark to determine if any experimental wells displayed bioactivity. Percent in gate of fluorescent, marker intensity is shown as scatter plots of mean ± S.D. and tested for significance against vehicle control of respective timepoints (n = 3, Two-way ANOVA with Dunnett's multiple comparison's test). *p < *.05, **.01, ***.001, ****.0001* V = Vehicle, B = Bafilomycin A1, E = Etoposide, N = Nocodazole, T = Thapsigargin

trends (Figure 2.9B).

To test for specific activity of ICI markers with MAM individual chromatographic runs of injury control compounds were performed for etoposide, nocodazole, staurosporine, and bafilomycin A1 to verify chromatographic separation into separate wells and to guarantee ICI signals were attributed to only one spiked compound (Figure 2.10). Thapsigargin was excluded from evaluation as it displayed modest injury signals in MAP conditions (Figure 2.6D) Bafilomycin A1, nocodazole, and staurosporine were selected for the positive control array since

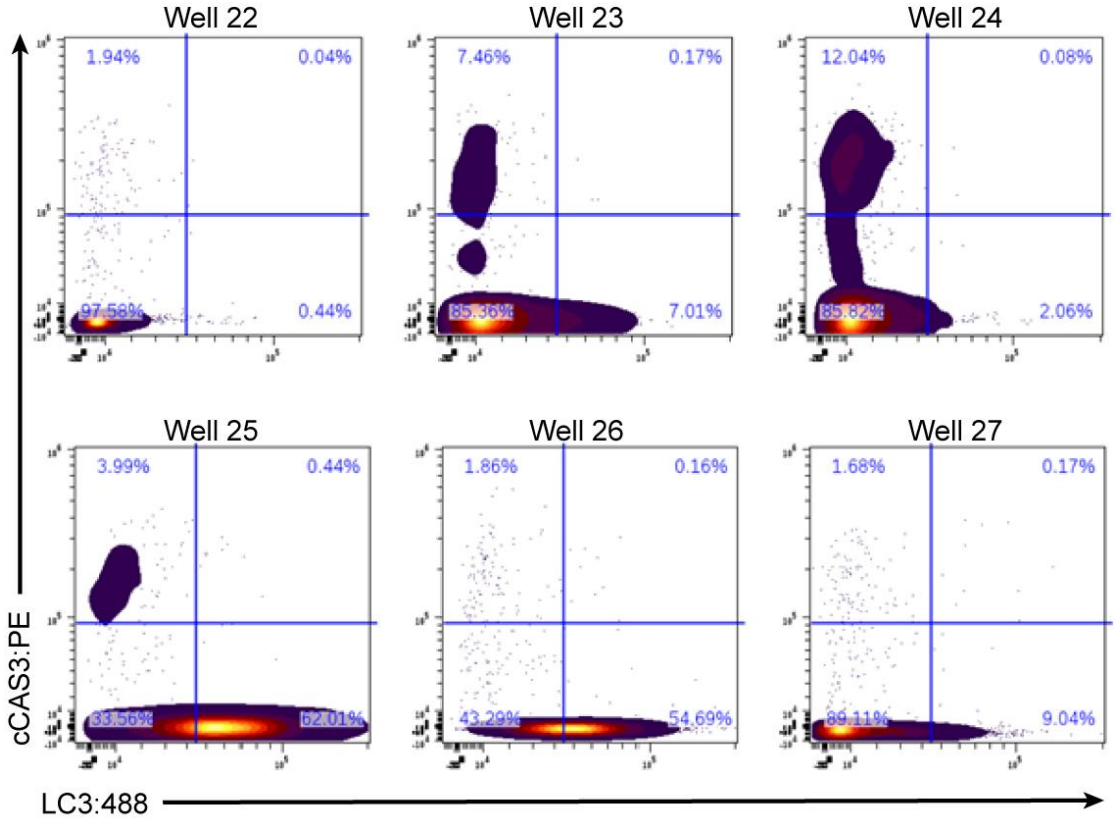

Figure 2.12. Biaxial gates of wells 23-27 to examine staurosporine induced cCAS3:PE and LC3:488 signal across wells. Queried wells were isolated and gated as contour density plots by quadrant to observe percent positive cells for both, one, or no markers. Positive and negative marker status of single cells is: upper left quadrant, cCAS3 +; upper right quadrantcCAS3 + and LC3 +; lower right quadrant, LC3 +, lower left quadrant, cCAS3 – and LC3 -. Staurosporine induced cCAS3 activity is most activated in wells 23, 24, and 25 consistent with peak elution times. Staurosporine induced LC3 activity is most activated in wells 25 and 26 consistent with elution time and diminished staurosporine concentration over 48.

each compound eluted into separate wells (Figure 2.9C and Figure 2.10). K562 cells were challenged with the positive control array for 48 hours and investigated for injury signal as percent positive cells in gate (Figure 2.9C). Each MAM experiment included positive control wells containing pure control compounds as a reference for 'hit' bioactivity in addition to vehicle negative controls (Figure 2.11). The positive extracted ion currents for nocodazole (*m/z* 301.9, $[M + H]^+$), staurosporine (*m/z* 466.9, $[M + H]^+$), and bafilomycin A1 (*m/z* 645.0, $[M + H]^+$) and complementary retention times aligned to wells positive for fluorescent signal (Figure 2.9C). Nocodazole positive wells showed induction of p-MLKL, p-HH3, and p-EIF2α but not cCAS3 nor

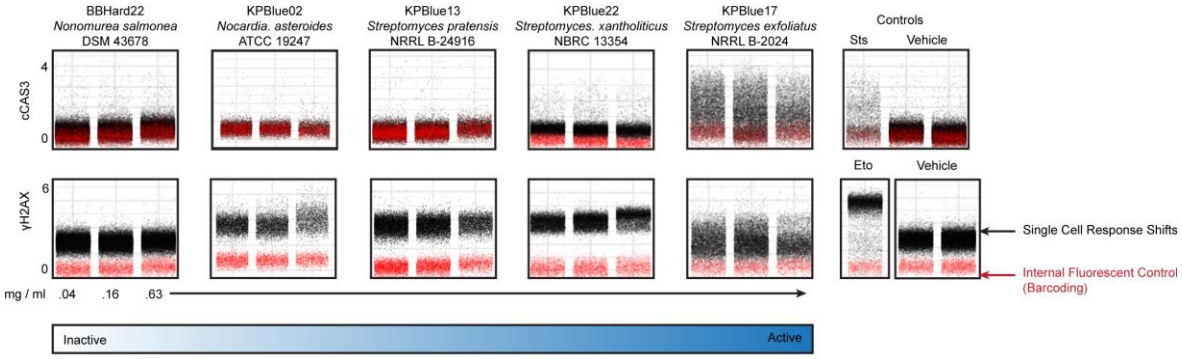

Figure 2.13. Dose dependent extract activity for apoptosis (top) and DNA damage markers (bottom) in MV-4-11 cells. The strain identifier, closest relative, and culture collection are indicated on top. Black dots indicate individual responses of single cells. Red dots represent an internal assay control for background fluorescence. Extracts exhibited increased activity from left to right judged by fluorescent intensity of single cells for each injury marker.

γH2AX (Figure 2.9C). Staurosporine elution corresponded to an elevated cCAS3 signature along with γH2AX and LC3 consistent with observations in Figure 2.6D). However, maximal staurosporine induced LC3 marker response did not precisely correlate with cCAS3 signal and occurred in wells immediately following. Thus, the cell responses in wells 22 - 27 were investigated for single cell responses for cCAS3 and LC3 simultaneously to evaluate marker signal at 48 hours (Figure 2.12). The elution peak, and thus highest concentrations, of staurosporine was split between wells 23 and 24 then diminished, and thus decreased in concentration, from wells 25-27 (Figure 2.9C and Figure 2.10). These observations were consistent with marker responses in Figure 2.6. Concentrations of staurosporine in excess of 1 µM rapidly induced cCAS3 without a corresponding LC3 signal (Figure 2.6C) and LC3 injury is present after 48 hours in sub-1 µM concentrations. Bafilomycin A1 containing wells are positive for LC3 and γH2AX consistent with Figure 2.6 (Figure 2.9C).

The success of MAM depends on high-fidelity fluorescent cell status marker responses to bioactive components in the presence of potentially confounding primary metabolites, cell wall, membrane, and spent growth media components in typical microbial extracts. Thus, five extracts

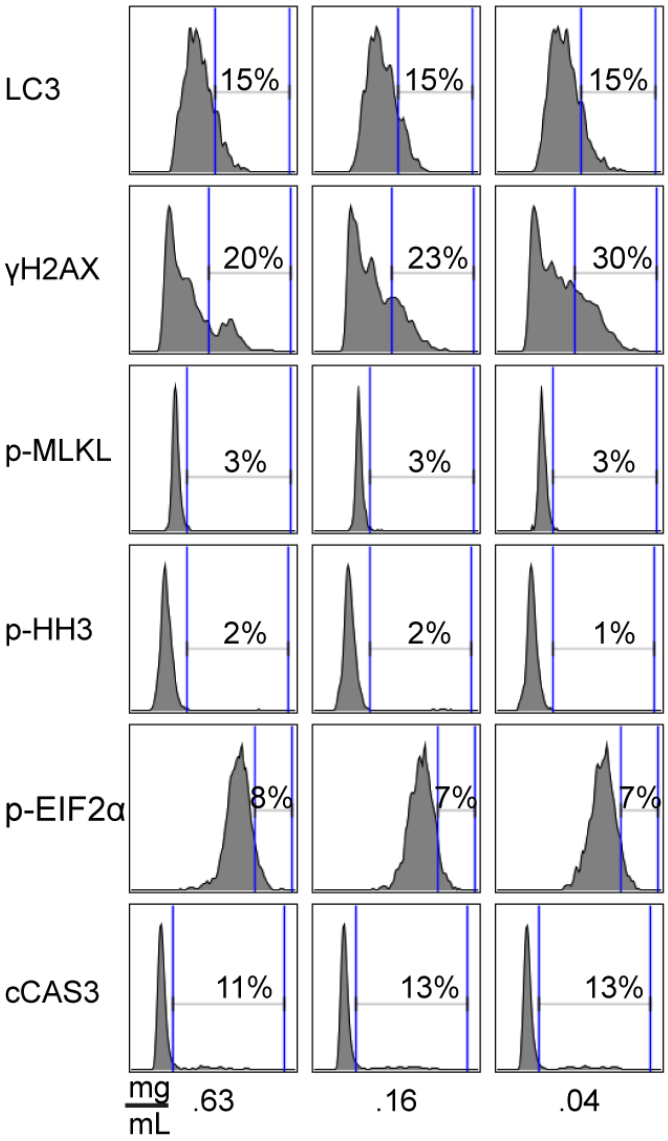

Figure 2.14. Dose response of KPBlue17 extract in K562 cells. Data shown as percent in gate for respective marker signal

of actinomycete genera were cultured in ISP2 and evaluated for apoptosis and DNA damage by serial dilution in MV-4-11 cell line (Figure 2.13). The KPBlue17 (99% 16S identity *Streptomyces exfoliatus*, NRRL B-2024) extract induced cCAS3 and γH2AX markers at all challenged doses (Figure 2.13). Extract KPBlue22 (99% 16S identity *Streptomyces xantholiticus*, NBRC 13354) demonstrated single cell signal shifts for DNA damage response, γH2AX, at the highest dose of

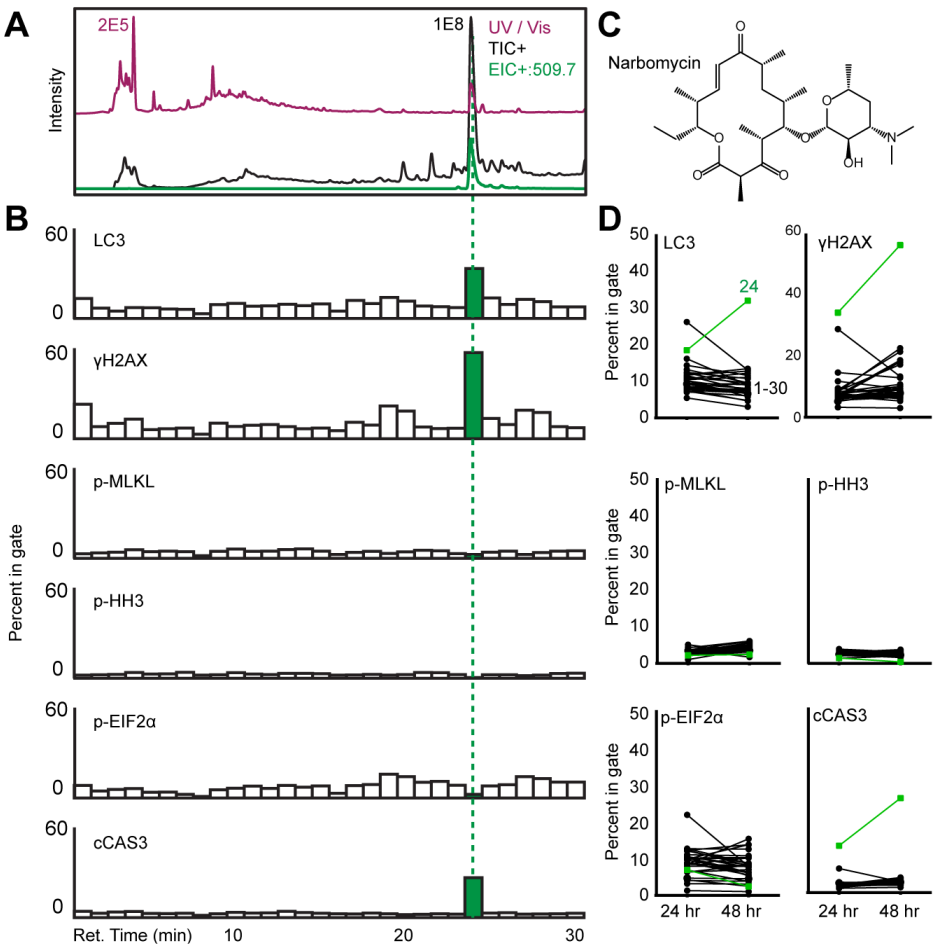

Figure 2.15. Multiplexed activity metabolomics informs isolation of secondary metabolites by injury signatures. (A) KPBlue17 crude extract was fractioned by reverse phase, split flow HPLC/UV/MS with polarity switching mass scanning to associate metabolite spectral data to well eluates by retention time. UV/Vis absorbance spectra is shown in purple, total positive ion current is shown in black, and positive extracted ion is shown in green (m/z 509.7 [M+H]+) (B) Percent positive cells for each injury signal was aligned to chromatograms to identify spectral regions with a bioactive component. Green bars indicate a hit for the respective marker. (C) Chemical structure of the isolated active component, narbomycin. (D) Biological response to metabolomic challenge increased from 24 to 48 hours in wells containing narbomycin (green 24). All other wells identified in black, 1-30, were negative for biological signal.

.63 mg/mL and failed to induce a cCAS3 response (Figure 2.13). Several inert extracts exhibited in Supporting Figure 13 failed to activate both injury signals regardless of dose. The inert extract KPBlue13 (99% 16S identity *Streptomyces pratensis,* NRRL B-24916*)* was arbitrarily selected from tested inactive extracts to confirm the ICI module for application using MAM (Figure 2.13). Two metabolomic arrays were generated for evaluation: 1) fractioned KPBlue13 and 2) fractioned

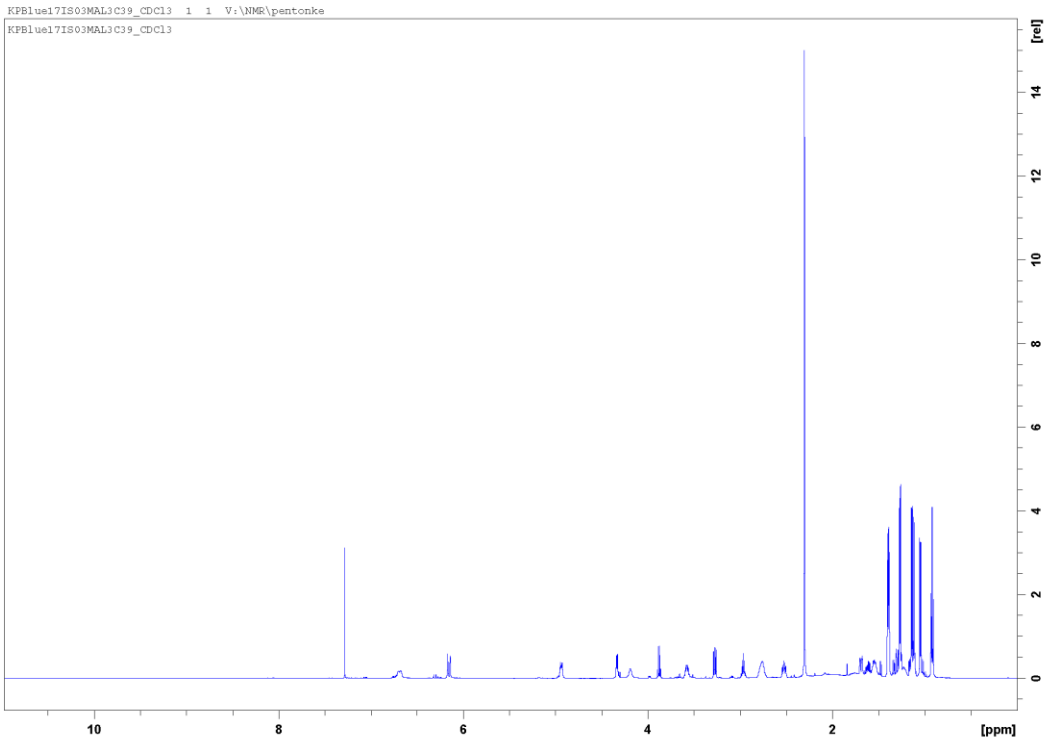

Figure 2.16. Narbomycin ^{1}H NMR 600 MHz

KPBlue13 spiked with bafilomycin A1, nocodazole, and staurosporine (Figure 2.9D-E). The metabolomic array generated from the crude extract induced no significant marker changes in K562 cells (Figure 2.9D), indicating minimal interference from media or cell associated metabolites in the extract and conservation of negative activity between leukemia cell lines. The spiked extract, however, demonstrated marker shifts in K562 cells matched to bafilomycin A1, nocodazole, and staurosporine containing wells that aligned to retention times of their respective extracted ion currents (Figure 2.9E). The specific activity observed in the spiked MAM were consistent with injury control compound retention times and mirrored results from pure injury control injections (Figure 2.9C-E). Taken together, this data demonstrates a robust system for simultaneous identification of bioactive metabolite-associated *m/z* features within a chemically

complex metabolome that impact a diverse array of terminal stress effectors in a high-throughput fashion.

2.2.9 MAM identifies activity of the secondary metabolite narbomycin in an unknown extract

The hypogean actinomycete designated KPBlue17 demonstrated bioactivity across all serial dilutions at concentrations as low as 0.04 mg/mL in MV-4-11 and K562 cell lines (Figure 2.13 and Figure 2.14). Conservation of activity at these dilutions predicts sufficient specific activity to facilitate identification of a metabolite using MAM. Therefore, the extract was subjected to MAM to challenge cells for 24 and 48 hours. Enhanced marker shifts for autophagy, DNA damage, and apoptosis were observed in well 24 that aligned to a positive ion peak with an extracted current of *m/z* 509.7 $[M + H]^+$ (Figure 2.15A-B). A second peak of the same *m/z* was evident at a later

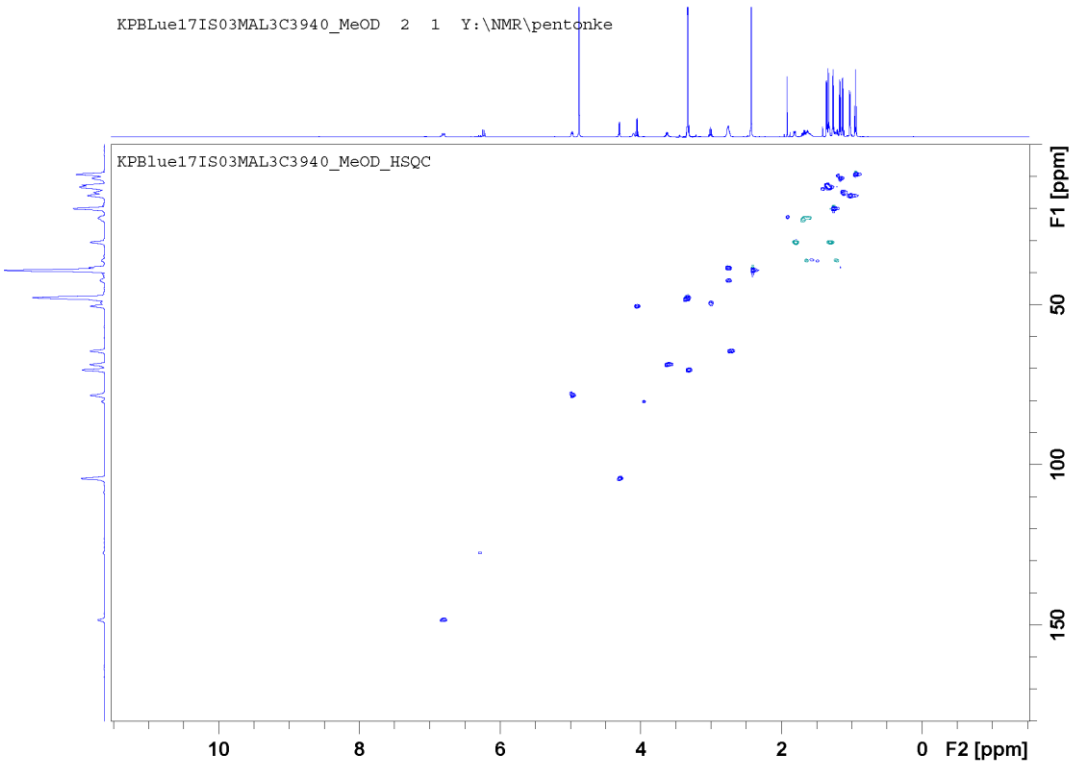

Figure 2.17. Narbomycin HSQC 600 MHz.

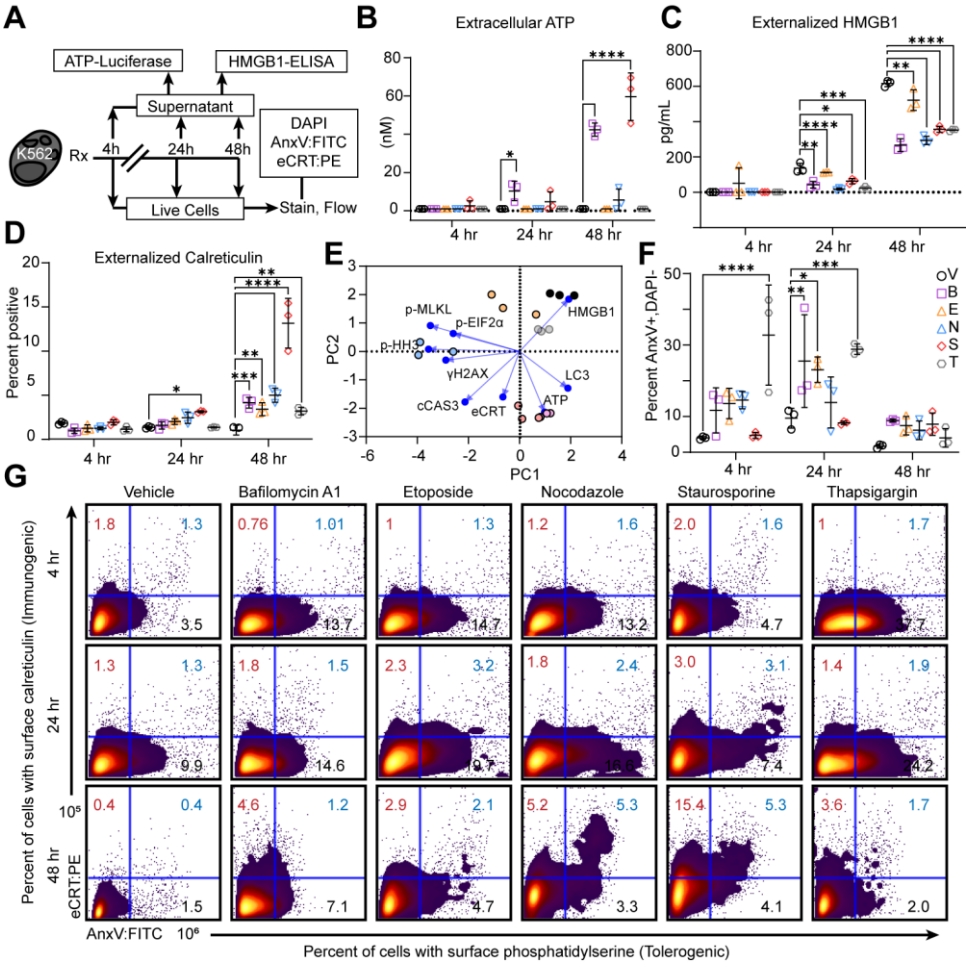

Figure 2.18. Secondary metabolites orient immunogenic hallmark intensity in leukemia model. (A) K562 cells were challenged with 1 μM of compound or vehicle and sampled at 4, 24, and 48 hours for detection of canonical immunogenic signals ATP, HMGB1, and eCRT. (B) Extracellular ATP concentrations were determined from cell supernatant at each timepoint with Steady-Glo® Luciferase Assay system. Scatter plots represent mean ± S.D. (n = 3, Two-way ANOVA with Dunnett's multiple comparison test). (C) Extracellular HMGB1 concentrations were determined form cell supernatant at each timepoint with colorimetric HMGB1 ELISA. Scatter plots represent mean ± S.D. (n = 3, Two-way ANOVA with Dunnett's multiple comparison test). (D) Externalized calreticulin (eCRT) was measured on live cells with fluorescent anti-calreticulin antibody at each timepoint and assessed as percent in gate of calreticulin positive cells. Scatter plots show chemically induced fluorescent signal measured as percent in gate mean ± S.D . (n = 3, Two-way ANOVA with Dunnett's multiple comparison test). (E) Nine continuous variables, six flow markers and three DAMPs, were standardized for parallel analysis with Monte Carlo simulations to calculate the eigenvalues of resulting principle components (PCs). PCs with eigenvalues that exceeded the 95th percentile of 1000 randomly seeded simulations were selected. Biplot revealed correlation among secondary metabolite influence on cell injury responses. (F) Annexin-V:FITC positive, DAPI negative cells. Scatter plots show chemically induced fluorescent signal measured as percent in gate mean ± S.D. Percent positive eCRT indicated in red, double positive eCRT and AnxV in blue, and AnxV positive in black. (n = 3, Two-way ANOVA with Dunnett's multiple comparison test). (G) At each timepoint, live cells were stained for eCRT followed by staining with annexin-V:FITC and the vital dye 4,6-diamidino-2-phenylindole (DAPI). Representative contour plots of biaxial gating for eCRT and annexin-V. p *<.05, +<.01, %<.001, $<.0001 V = Vehicle, B = Bafilomycin A1, E = Etoposide, N = Nocodazole, S = Staurosporine, T = Thapsigargin

retention time; however, no bioactivity was observed to be associated with this peak. The isolation

of the active peak was prioritized and dereplicated to the macrolide antibiotic narbomycin by *m/z* (Fig. 2.15C) and NMR (^{1}H and HSQC, Figure 2.16 and 2.17) (*34*). Injury signals in narbomycin containing wells increased from 24 to 48 hours via prolonged exposure to the bioactive agent (Figure 2.15D). All other wells remained inactive (Figure 2.15B). The narbomycin induced injury phenotype is consistent with the macrolide family of natural products, including azithromycin and clarithromycin, that are reported inhibitors of autophagic flux and capable of modulating apoptotic responses (*41-43*). The induction of DNA damage response maker γH2AX by narbomycin has never been reported and is not well documented overall in macrolides. Following implementation of the cell injury module, the relationships between chemically induced cell injury patterns to reported immunogenic DAMPs were investigated, namely ATP, HMGB1, and eCRT. Injury control compounds were used to challenge K562 cells to evaluate extracellular release of ATP and HMGB1 to the cell supernatant and eCRT on the cell surface (Figure 2.18A). Extracellular ATP release was first observed at 24 hours by the autophagy inhibitor bafilomycin A1 (Figure 2.18B). This persisted to 48 hours and more than doubled extracellular ATP concentrations (Figure 2.18B). Pan-kinase inhibition by staurosporine required 48 hours to promote ATP release to the supernatant (Figure 2.18B). In contrast to ATP secretion, no general trend from injury controls enhanced HMGB1 ejection to the supernatant (Figure 2.18C). Rather, all compounds, except etoposide, reduced HMGB1 detection in the supernatant at 24 and 48 hours compared to vehicle control (Figure 2.18C). In K562 CML model surface exposure of calreticulin was first detected at 24 hours in staurosporine challenged cells (Figure 2.18D). By 48 hours all cell populations demonstrated a statistically significant increase of calreticulin surface expression compared to vehicle control (Figure 2.18D).

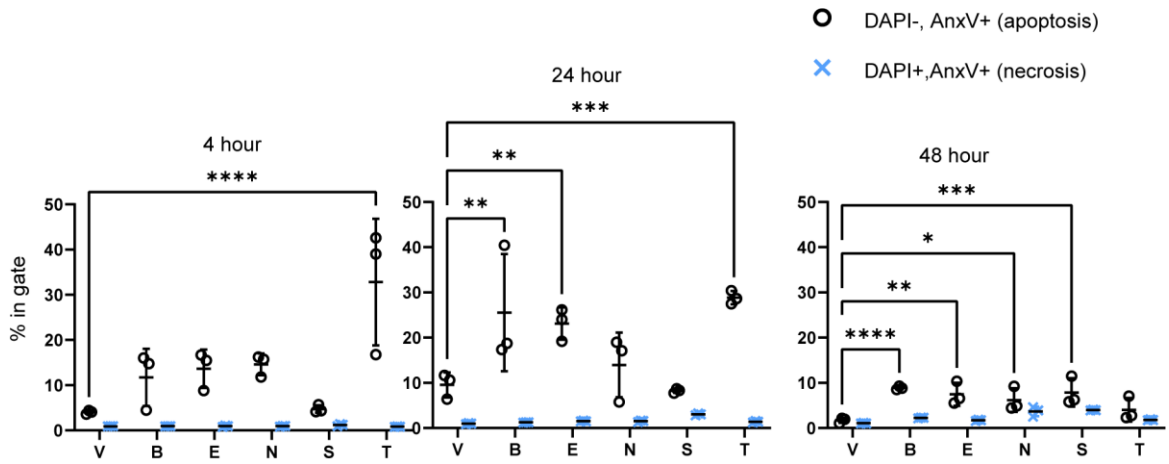

Figure 2.19. Detection of apoptotic and necrotic cells over time. Live K562 cells were stained with AnnexinV-FITC and the vital dye DAPI to evaluate phosphatidylserine exposure and membrane permeabilization respectively by percent in gate for positive signal. Early apoptotic cells are AnxV + only (black circles) while necrotic cells are AnxV + and DAPI + (blue X). Error bars represent mean ± S.D. (n = 3, Two-way ANOVA with Dunnett's multiple comparison test). *p* < *.05, **.01, ***.001, ****.0001 V = Vehicle, E = Etoposide, N = Nocodazole, S = Staurosporine, T = Thapsigargin.

2.2.10 Detection of immunogenic hallmarks in a leukemia cell line

Intracellular injury and extracellular immunogenic hallmarks were analyzed in conjunction by principal component analysis (Figure 2.18E). Cells positive for cCAS3 and LC3 coincided with ATP release and calreticulin externalization based on magnitude of negative correlation in PC2 by loadings analysis (Figure 2.18E). On the other hand, markers p-MLKL, p-EIF2α and p-HH3 were positively correlated with PC2 and failed to elevate ATP release as shown in Figure 2.18. Remarkably, no compounds selectively enhanced release of HMGB1 to the supernatant (Figure 2.18C) and it is the only readout with positive correlation to PC1 and PC2 (Figure 2.18E). Based on this report, staurosporine challenged cells are most likely to elicit cCAS3, eCRT, and ATP which all presented strong negative correlations to PC2 in loadings analysis (Figure 2.18E). Finally, nocodazole treated cell populations were strongly linked to changes in p-EIF2α, p-MLKL, and p-HH3 revealed by the largest positive values in PC2 (Figure 2.18E) Etoposide and thapsigargin by comparison are most likely to modulate HMGB1 while posing little effect on other injury signals (Figure 2.18E). It is notable that not all ICD signals shared positive signal correlation

nor that any singular ICI guarantees induction of ICD hallmarks.

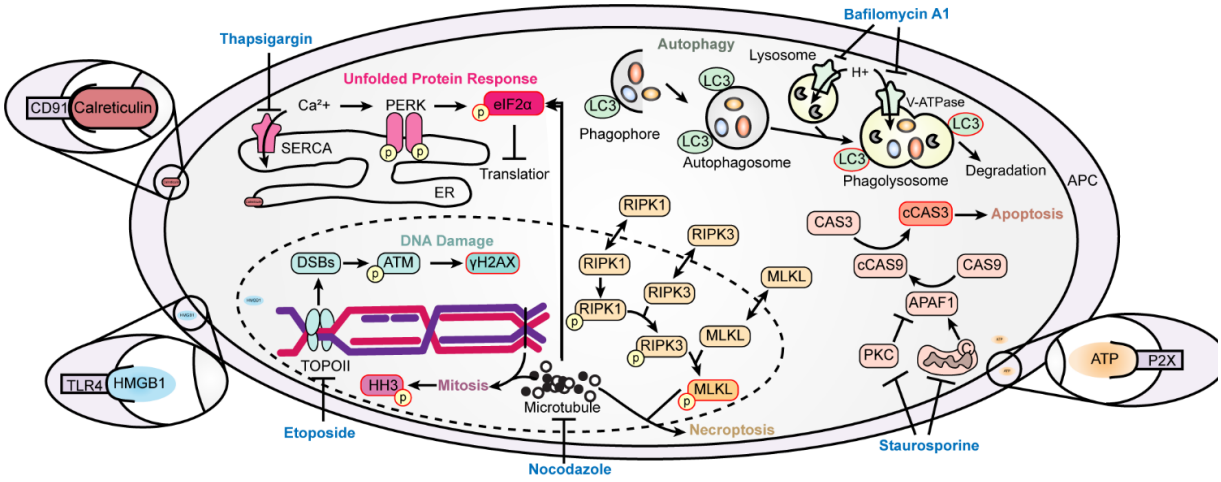

Figure 2.20. Secondary metabolite directed cell injury model. Depiction of the six ICI mechanisms measured (color-coded pathways, e.g., unfolded protein response), highlights the key readout for each (pink highlighted boxes, e.g., EIF2α), and indicates a control compound characterized as a positive effector of the pathway (blue text, e.g., thapsigargin). Thapsigargin inhibition of Ca-ATPase SERCA in the endoplasmic reticulum increases free calcium in the cytosol to trigger ER stress response pathways including the ER resident transmembrane protein kinase, PERK, which phosphorylates eIF2α to inhibit translation until ER stress resolution. Bafilomycin A1 inhibits autophagy by inhibitng V-ATPase on the lysosome and phagolsoysome membranes thus hindering lumen acidification and subsequent activation of serine hydrolases therein. In turn, this prevents LC3 protein degradation on autophagic structures yielding increased levels of LC3. Staurosporine is canonically considered a pan-kinase inhibitor that blocks ATP binding pockets. Staurosporine inhibition of PKC and mitochondria localized enzymes result in in disinhibition of APAF1 an apoptosome related protein that facilitates conversion of CAS9 to its active form cCAS9 which then cleaves CAS3 to activate apoptotic hallmark cCAS3. Nocodazole binds beta-tubulin to prevent microtubule elongation. This prevents cellular division leading to enhanced levels of phosphorylated histone H3 protein. Additionally, microtubule inhibition can increase resident levels of the necroptotic execution protein p-MLKL. MLKL is phosphorylated following signal transduction via phosphorylation of RIPK1 and RIPK3 after exiting nuclear-cytosol cycling in response to stress. p-MLKL is trafficked to the cell membrane for oligomerization and insertion into the cell membrane leading to cell lysis. Etoposide forms a ternary complex with DNA and topoisomerase II to prevent re-ligation of DNA yielding double strand breaks sensed by ATM. ATM then phosphorylates histone variant H2AX (γH2AX) which activates the DNA damage response to resolve double strand breaks. Literature evidence indicates inhibition and/or activation of these pathways can be pro-immunogenic, however the relative temporal relationship of these signals to enhance immunogenic cell death remains under investigated. To measure downstream cellular functions following ICI signaling mechanisms, three mechanisms of immunogenic cell death can be measured, namely calreticulin, HMGB1, and ATP. Each DAMP is shown interacting with respective surface receptors on an antigen presenting cell in purple.

In addition to measuring immunogenic eCRT, tolerogenic exposure of phosphatidyl serine (sPS) in the outer leaflet of the plasma membrane was also examined (*44, 45*). The sPS on live cells was measured with annexin V:FITC and the vital dye DAPI was used to label necrotic cells (*46, 47*) (Figure 2.18F and Figure 2.19). Thapsigargin treated cells displayed high levels of sPS at

4 and 24 hours, as did etoposide, and remained DAPI negative with minimal calreticulin externalization (Figure 2.18G) suggesting thapsigargin and etoposide induced sPS is not predictive of early apoptotic death nor necrosis under these conditions. Conversely, staurosporine failed to induce significant sPS and was the most positive for eCRT after 48-hour challenge and supports staurosporine induced apoptosis may be immunogenic (Figure 2.18G). Bafilomycin A1 induced sPS at 24 hours and limited calreticulin externalization through 48 hours (Figure 2.18G).

In total, the primary multiplexed assays of MAP and MAM with addition of the cell injury module provided a workflow for the discovery of small molecule and natural product effectors of ICI. In turn, ICI signature were used as a tool to advance active fractions to secondary DAMP assays and prioritize isolation of bioactive components. The compounds tested here both as pure compounds and spiked into extracts interact with cellular processes that are conserved across cell types (e.g., kinases, microtubules, SERCA, autophagy) and should ease application into other model systems without requiring specialized stimulation conditions or genetic modifications.

2.3 Discussion

It is unknown if current therapeutic regiments in the clinic optimally elicit immunogenicity in part because the relationship between cell injury, death, and immunogenicity is not completely defined. Moreover, successful immunogenic therapies are largely confined to secondary metabolites (*48*). Analogs of established immunogenic compounds and scaffolds are evident in putative encoding biosynthetic gene clusters in genome sequenced organisms (*49*, *50*); however, accessing these compounds is an incredibly labor and time-intensive process. The vast chemical reservoir confounds selection of producing organisms, which may fail to synthesize the compound of interest under laboratory conditions, and prioritization of compounds for isolation. The fluorescent module presented here combined with MAP and MAM offer a high-throughput

phenotypic screen for ICI signals. In turn, compounds for isolation can be prioritized by bioactivity in specific injury pathways rather than overt cytotoxicity as a prerequisite for anti-tumor potential.

A common feature of chemically induced immunogenicity is activation of damage response and cell stressor signaling pathways including modulation of autophagy (*8, 9, 11, 51*), activation of the PERK arm of the UPR (*10, 22, 51*), DNA stress (*12, 52*), and certain death modalities (Figure 2.20) (*39, 53, 54*) Inhibition of basal autophagy with the natural product bafilomycin A1 suspends degradation of effete cellular organelles by preventing acidification and fusion of autophagosomes and lysosome via v-ATPase blockade (Figure 2.20) (*25, 55*). The inhibition of autophagy competent cells is required for ICD but is not sufficient (*56, 57*). An additional necessary but insufficient ICD prerequisite is phosphorylation of translation initiation factor EIF2α at serine 51, which then stabilizes the inactive congener of EIF2B to prevent translation initiation (*58-60*). DNA damage is also a powerful immunogenic adjuvant in animal models (*10*). Inhibition of autophagy, prolonged ER stress, or DNA damage can injure a cell such that apoptosis yields an immunogenic, rather than tolerogenic, response. Alternatively, necroptosis is an explosive form of ICI that can release DAMPs and promotes anti-tumor immunity in murine models (*11*). This form of programmed cell death requires phosphorylation of mixed lineage kinase domain like pseudokinase (MLKL) at serine 358 (p-MLKL) by the receptor-interacting protein kinase family of proteins (Figure 2.20) (*61-63*). Once phosphorylated, p-MLKL transverses the cell nucleus and cytosol along the microtubule network to form oligomers in the plasma membrane that promote cation influx to drive the final stages of necroptosis (*36, 61*). There is growing evidence that these injury signals, in addition to canonical DAMPs ATP, HMGB1 and eCRT, can indicate immunogenic potential prior to advancing to animal and primary cell models.

By way of antibody validation, chemical induction, and barcoding, we achieved detection

of apoptotic, necroptotic, autophagic, mitotic, UPR and DNA damage effectors in tandem for the first time in an unmodified cell system to found nascent chemically induced ICI profiles. Together, these central death and damage response processes exemplified several pathways that contribute to immunogenic DAMP presentation. The secondary metabolite mediated cell injury profiles presented here established benchmark control compounds for application of the ICI module to qualify and quantify bioactivity of unknown molecular agents in a discovery setting (Figure 2.20). This discovery scheme identified new biological activity of the secondary metabolite narbomycin (Fig. 2.15) and will facilitate isolation of bioactive secondary metabolites that induce cellular injury relevant to downstream ICD.

Specific to the compound standards utilized here, early patterns corroborating ICI to ICD begin to emerge. For example, bafilomycin A1 and staurosporine enhanced LC3 and cCAS3 in varied time-dependent fashions which confirmed natural products can modulate specific injury responses in sequence. Additionally, staurosporine competes for binding pockets of ATP dependent enzymes thus diminishing ATP hydrolysis (*64, 65*) while bafilomycin A1 prevents ATP turnover by rotational blockade of v-ATPase. Given these natural products inhibit two different cellular processes yet both elevated ATP secretion suggest ATP hydrolysis blockade facilitated transference of ATP to the extracellular space, potentially as a consequence of elevated basal intracellular ATP levels. In addition to autophagy and apoptotic injury, cells can also engage the UPR to fine tune translation status as reaction to endoplasmic reticulum stress. However, the inability of thapsigargin to elicit DAMPs ATP and HMGB1 indicate p-EIF2α alone is not sufficient to induce a robust immunogenic response in this model (Figure 2.18B-C). This insufficiency is further supported by elevated detection of sPS in thapsigargin treated cells as sPS can function as a tolerogenic signal (Figure 2.18E-F) (*66, 67*). Finally, Disruption of the

microtubule network by nocodazole inhibits p-MLKL trafficking yielding an intracellular accumulation of the necroptotic effector without inducing necroptosis (*29, 36, 68*).

In summary, the workflow described herein simultaneously detects multiple markers of cell injury status that are pre-requisite for an immunogenic death in multiplexed samples of pure compounds or metabolomic fractions. This work describes a new multiplexed panel entailing extensive optimization and development of two new antibody reagents for single cell detection, and their optimization for fluorescent cell barcoding, balancing 10 fluorophores into the debarcoding workflow. This advanced prior work by transitioning FCB from traditional cytometry instruments to state-of-the-art spectral flow cytometers (Cytek Aurora) and expanded this assay's detection capacity into three biological processes (autophagy, necroptosis, and UPR) in addition to apoptosis, DNA damage, and mitosis. This work also built upon pioneering work in the ICD field (*8, 10, 69, 70*) to introduce the first cell-based assay to measure six ICI signals to accelerate evaluation of immunogenic agents and explored time-dependent signal onset to chemical challenge and offered proof of principal for detection and discovery of new biologically active compounds in a chemically complex metabolomic sample. Indeed, the identification of narbomycin as a modulator of mammalian cell injury response from an extract of a previously uncharacterized microorganism illustrated discovery of new biological function in known compounds. The ICI module of the MAM platform will be applied to test injury specific bioactivity in extracted actinobacteria metabolomes to inform natural product dereplication, isolation of new ICI mediators, and fast-track interpretations of ICD that result in more durable antitumor immune responses. This will accelerate discovery of new compounds with immunogenic potential or elucidate novel immunogenic character of known compounds that may direct future pharmacological studies. In total this work demonstrates a fluorescent high-throughput, high-

fidelity assay that captures cell injury phenotype patterns in unmodified cells to focus discovery of novel chemical agents with therapeutic and immunogenic potential.

2.4 Material & Methods

Processing: Cell viability and fixation

Following treatment of cells with compounds, vehicle or metabolomic fractions, 200 µl of cells (1 million cells/mL), were stained with 20 µL of Ax700 (Thermo A20010, stock concentration 20 µg/mL) to a final concentration of 0.04 µg/mL 37 °C for 20 min at and protected from light. Cells were then transferred 96 well V-bottom polypropylene plate with 20 µL of 20 % PFA (Alfa Aesar 47340) for a final PFA concentration of 1.6 % for 10 min. at room temperature, protected from light. Plate was centrifuged at 800 g for 5 min, supernatant decanted by plate inversion and dabbed dry on a Kimwipe (Kimtech 34155). The plate was then vortexed, and cells permeabilized with 200 µl ice-cold MeOH for at least twenty minutes at - 20 °C. After permeation and prior to FCB, cells were centrifuged at 800 g for 5 min, decanted by inversion, vortexed, and resuspended in 200 µL PBS (Gibco 10010-023).

Processing: Fluorescent cell barcoding

Eight 1:1.7 serial dilutions serial dilutions of Pacific Blue (Thermo P10163) were prepared in DMSO at concentrations ranging from 10 µg/mL to 0.24 µg/mL. Six 1:1.7 serial dilution stock concentrations of Pacific Orange (Thermo P30253) were prepared in DMSO at concentrations ranging from 40 µg/mL to 2.82 µg/mL. Alexa750 (Thermo A20011) 500 µg/mL stock solution in DMSO was prepared at 5 µg/mL. All three dyes were combined on a single V-bottom polypropylene master plate as follows: 50 µL of Pacific Blue were added to plate rows with the highest concentration in row A and the lowest concentration in row H; 50 µL of Pacific Orange were added to columns with the highest concentration in column 1 and lowest concentration in

column 6; 50 µL of Alexa 750 were added to all wells. Master plates were then aliquoted in 15 µL volumes to 96 well V-bottom propylene plates and stored at – 20 °C. An aliquot of 185 µL of fix/permed cells in PBS were added to 15 µL of barcode dyes and stained for 15 minutes at room temperature, protected from light. Barcoding reactions were quenched with 70 µl 2% BSA in PBS, centrifuged at 800 g for 5 min, decanted by inversion, vortexed, washed with 200 µl 2% BSA in PBS, centrifuged at 800 g for 5 min. decanted by inversion, and vortexed. Wells in column 1 were then resuspended in 200 µL of 2% BSA in PBS then transferred to column 2 and repeated to column 6. All rows in column 6 were then pooled into 1 FACS tube.

Processing: Flow cytometry data acquisition

Flow cytometry data was acquired on four laser (405 nM, 488 nM, 561 nM, and 640 nM) Cytek Biosciences Aurora spectral flow cytometer following spectral unmixing with single color reference controls. Data was uploaded and stored in Cytobank for gating, compensation, and analysis of unmixed cytometry data files (.FCS file format). Quality control (QC) gating consisted of QC1: FSC-A vs. SSC-A for cell bodies, QC2: FSC-A vs. FSC-W for singlets, and FSC-A vs. Ax700 for viable cells. Unmixed FCB samples were QC gated with addition of QC4: FSC-A vs. Ax750 for barcode uptake control, compensated then debarcoded with DebarcodeR to produce one FCS file per well and uploaded to Cytobank for storage and further analysis.

Multiplexing: Validation panel

K562 cells were challenged with a final concentration of 10 µM of thapsigargin in hanks balanced salt solution (Corning 21-021-CV) or 10 µM etoposide, or nocodazole in cRPMI for 24 hours or DMSO vehicle control. Cells were fixed in a final concentration of 1.6 % PFA, permeabilized with ice-cold MeOH, and stained with NHS-functionalized Pacific Blue, Pacific Orange, or Alexa 750 dyes (1 color/condition) pooled (3 conditions) into a single FACS tube and stained with antibody

cocktail of γH2AX:Percp-Cy5.5 (BD 564718, 2.5:100) and p-MLKL (CST 91689S 5:100) or p-EIF2α (CST 3597L 5:100), in 100 µL of 2 % BSA in PBS for thirty minutes in the dark. Staining was quenched with 1 mL of 2 % BSA in PBS, centrifuged at 800 g for 5 min., and decanted by inversion. FACS tube was vortexed and washed with 1 mL of 2 % BSA in PBS, centrifuged at 800 g for 5 min., decanted by inversion, vortexed and resuspended in 200 µL 2% BSA in PBS. Rabbit antibodies p-MLKL and p-EIF2α were detected with Gt α Rb:488 fluorescent secondary antibody at 1:5000 by staining for 30 minutes at room temperature in the dark in a final volume of 400 µL. Cells were washed with 2 % BSA in PBS as described above prior to analysis. This process was repeated following antibody conjugation with the exception of Gt α Rb Ax488 fluorescent secondary antibody and addition of p-MLKL:568 or p-EIF2α:647 (5:100).

Multiplexing: Antibody conjugation

Antibody p-MLKL was conjugated to Ax568 with Thermofisher antibody labeling kit A20184 adapted from manufacturer's instruction. Antibody p-EIF2α was conjugated to Ax647with Thermofisher antibody labeling kit A20186 adapted from manufacturer's instructions. In brief, antibody storage solution was removed by 10 kDa M.W. concentrator tubes (Pierce 88513) with 100 mM sodium bicarbonate. Tubes were spun at 11,000 g for 3 minutes, flow through discarded, and 100 µL of 100 mM sodium bicarbonate added to concentrator tube. This process was repeated thrice. Pure antibodies were harvested and incubated with specified antibody labeling kit in 100 µL volume of 100 mM sodium bicarbonate for 1 hour in the dark with mixing. Excess dye was removed by purification resin provided by the manufacturer. Antibodies were stored in antibody storage solution consistent with manufacturer's recommendation. Fluorescent intensity of conjugated antibody was evaluated by SDS-PAGE fluorescence gel in reduced and non-reduced condition. Antibodies were prepared in Tris/SDS/Glycine running buffer and Laemlli sample

buffer +/- BME incubated at room temperature for 5 min and heated to 95 °C for 5 min then centrifuged. Samples were loaded onto a 4 – 20 % Tris/Glycine gel and electrophoresed for 60 min at 175 volts. Gels were imaged with a Biorad Chemidoc MP Imaging System.

Multiplexing: Injury panel

Cells were stained with fluorescent antibodies LC3:Ax488 (CST 13082, 1:100), γH2AX:Percp-Cy5.5 (BD 564718, 2.5:100), cCAS3:PE (10:100), p-MLKL:Ax568 (CST 91689S 5:100), p-HH3:Pe-Cy7 (Biolegend 6410, 1:1000), p-EIF2α:Ax647 (CST 3597L 5:100) in 100 µL of 2% BSA in PBS for 30 min in the dark. Staining was quenched with 2 % BSA in PBS, sample centrifuged at 800 g for 5 minutes, decanted by inversion, repeated once, and resuspended in 200 µL 2% BSA in PBS prior to analysis.

Multiplexing: Live cell panel

Cells were treated with 1 µM of control compounds for 4, 24, or 48 hours. At each timepoint cells were viability stained with Ax700 then stained with Calreticulin:PE (CST 19780, 1:50) for 30 min in the dark on ice. Cells were washed with 2 % BSA in PBS then stained with Annexin-V:FITC and a final concentration of 1 µM DAPI in annexin binding buffer on ice. Annexin-V:FITC and DAPI were not washed prior to live cell data acquisition consistent with manufacturer's instructions (CST 6592). DAPI was used to replace PI.

Profiling: Cell culture

K562, Jurkat, and MV-4-11 cell lines were a generous gift from the Ferrell lab and confirmed to be mycoplasma negative. K562 and Jurkat were cultured in complete RPMI (cRPMI) consisting of RPMI 1640 (Gibco 22400-089) supplemented to a final concentration of 10 % heat inactivated fetal bovine serum (Gibco 16140-071), 1 mM sodium pyruvate (Gibco 11360-070), and 1 % penicillin/streptomycin cocktail (Gibco 15140-122). MV-4-11 were cultured in IMDM (Gibco

12440-053) supplemented to a final concentration of 10 % fetal bovine serum. Cells were incubated in a water jacketed 5 % CO_2 incubator at 37 °C. Cells were maintained at densities between 100 thousand and 1 million cells per mL of culture media, fed every other day, and passaged every four days.

Profiling: MAP for signal specificity

Control compounds bafilomycin A1, etoposide, nocodazole, staurosporine, and thapsigargin were acquired from Selleckchem as noted in supporting information. Compound stock solutions were prepared at 200 x and diluted $\log_{10}$ across four wells for final concentration ranging from 10 µM to 10 nM. 1 µL of 200 x of each compound concentrations were added to respective wells and resuspended in 200 µL of cell containing media. At each timepoint cells were fix, permeabilized, fluorescently barcoded, and stained as described above. K562 CML, MV-4-11 B-myelomonocytic leukemia, and Jurkat T lymphoblastic leukemia cell models were treated with $\log_{10}$ series dilution from 10 µM to 10 nM and incubated for 4, 24, or 48 hours (Fig. 2A, Fig. S4). At each timepoint, cells were stained for viability with Ax700, fixed, and permeabilized as described above. Cells were FCB by well coordinates with an array of eight NHS-PB concentrations by six NHS-PO concentrations as well as one dye uptake control NHS-Ax750 concentration then pooled for homogenous staining with a fluorescent antibody cocktail consisting of 6 unique target:fluorophore combinations including: LC3:488, γH2AX:PCPC5, cCAS3:PE, p-MLKL:568, p-HH3:PEC7, and p-EIF2α:647, to yield a ten color fluorescent injury panel (Fig. 2A, Table S2). Barcoding and pooling reduces sample-to-sample staining variability and processing by incubating all samples with the same fluorescent antibody cocktail over equivalent time intervals and temperatures while also saving on costly antibody reagents and decreasing instrument use time. Secondary metabolite induced injury phenotype data were acquired on single cells on a Cytek

Aurora spectral flow cytometer and uploaded to Cytobank for storage and processing (*71*). Collected cellular events were quality control gated for viable singlets and control NHS-Ax750 barcode dye uptake (Fig. 2B). Barcoded cells were digitally reassigned to origin plate wells with the DebarcodeR (*32*) algorithm (Fig. 2B). Cells were processed and stained for analysis as described above (Fig. 2D) with the exception of dose variability.

Profiling: Crude microbial extract preparation

Laboratory isolate strain KPBlue13 (99% 16S sequence identity *S. pratensis*) and KPBlue17 (99% 16S sequence identity *S. exfoliates*) were isolated from Blue Spring Cave in Sparta, TN) was maintained on ISP2 agar (yeast extract 4 g/L, malt extract 10 g/L, glucose 4 g/L, and agar 17.5 g/L, pH 7.2). Loops of mycelia were used to inoculate 25 mL seed cultures in ISP2 medium (yeast extract 4 g/L, malt extract 10 g/L, and glucose 4 g/L, pH 7.2) incubating for 2 days at 30 °C. Seed cultures were then transferred to 250-mL Erlenmeyer flasks containing 25 mL of ISP2 and grown for 7 days at 30 °C with shaking. Aqueous fermentation broth was extracted by shaking with Diaion HP20 synthetic absorbent resin (Alfa Aesar) (125 mL of HP20 bead/H_2O slurry per 500 mL of aqueous broth) for 2 h. Fermentation broth was then centrifuged (3700 × g, 30 min) and the supernatant was decanted. Metabolites were eluted from absorbent resin and cells with methanol (250 mL of methanol/125 mL of HP20 bead/H2O slurry) by shaking for 1.5 h, followed by centrifugation (3700 × g, 30 min) and decanting the methanol extract. Further extraction was performed with acetone (250 mL of acetone/125 mL of HP20 bead/H2O slurry) by shaking for 1.5 h, followed by centrifugation (3700 × g, 30 min) and decanting the acetone extract. Methanol and acetone extracts were combined and lyophilized with Series 3 HT 6 Genevac with manufacturer's HPLC-Lyo method and stored at – 20 °C.

Profiling: Generation of metabolomic arrays

Mass spectrometry was performed by using a TSQ Triple Quantum mass spectrometer equipped with an electrospray ionization source and Surveyor PDA Plus detector. For positive ion mode, the following settings were used: capillary temperature 270 °C; spray voltage 4.2 kV; spray current 30 mA; capillary voltage 35 V; tube lens 119 V; and skimmer offset 15 V. For negative ion mode, capillary temperature 270 °C; spray voltage 30 kV; spray current 20 mA; capillary voltage 35 V; tube lens 119 V; and skimmer offset 15 V. Fractionated plates were prepared by injecting 20 µL of purified compounds in HPLC-grade methanol or concentrated extract via a Thermo PAL auto injector onto a Phenomenex Luna 5 µm C18(2) reverse-phase C_{18} HPLC column. The sample was fractionated using a gradient of 100% Buffer A (95% H_2O, 5% acetonitrile) to 100% Buffer B (5% acetonitrile, 95% H_2O) over 30 min at a flow rate of 1 mL/min and split in a 3:1 ratio with three parts going to the photodiode array detector and fraction collector and one part going to the MS. Fractions were collected in 1-min intervals in a 96 deep well plate. A volume of 150 µL of eluent from each well was transferred to four replica 96 well plates and dried in vacuo using a Series 3 HT-6 Genevac system with manufacturer's HPLC-Lyo protocol.

Profiling: MAM with internal standards

Dimethyl sulfoxide stock solutions of nocodazole (1 µL, 20 mM), staurosporine (1 µL, 20 mM) and bafilomycin A1 (4 µL, 5 mM) were added to 44 µL of crude extract at 100 mg/mL in HPLC-grade methanol and fractionated and lyophilized as described above. Wells were resuspended in 200 µL of media containing cells, incubated, and processed for flow cytometry as described above.

Assay: Luciferase ATP

Extracellular ATP was evaluated with Cell Titer-Glo 2.0 Luciferase Assay System (Promega G9241) adapted from manufacturer's instructions. Briefly, at each timepoint, cell supernatant from

treated cells was mixed 1:1 with Cell Titer-Glo reagent, in an opaque, white bottom plate, incubated at room temperature for 10 min then signal for total luminescence was acquired with a Biotek Synergy H4 Hybrid reader. Standard curves were generated for calculation of ATP concentrations. Samples below the limit of detection were assigned a unit value of 1. K562 were challenged cells with 1 µM of injury controls and incubated for 4, 24, and 48 hours (Fig. 4A). At each time point cell supernatants were harvested and split to evaluate ATP release with a recombinant luciferase (Promega, E2510) or HMGB1 ejection by ELISA (NovusBio, NBP2-62766) in accordance with manufacturers protocols (Fig. 4A).

Assay: HMGB1 ELISA

Extracellular HMGB1 was evaluated with Human HMGB1/HMG-1 colorimetric ELISA kit (Novus #NBP2-62766) adapted from manufacturer's instructions with the exception that harvested cell supernatants at each timepoint were diluted 1:9 in PBS prior to plating. Absorbance data was acquired a Biotek Synergy H4 Hybrid reader. Standard curves were generated for back calculation of HMGB1 concentrations. Samples below the limit of detection were assigned a unit value of 1.

Data: Statistical analysis and figure generation

Data was input to Graph Pad Prism (9.2.0) and analyzed with one-way or two-way ANOVA according to figure legends. All data is reported as mean +/- standard deviation (S.D.) of at least 3 biological replicates. Prism, Adobe Illustrator 2021, Microsoft Excel 2016 were used for figure generation. Principal component analysis was performed on nine continuous variables that were standardized for parallel analysis with Monte Carlo simulations to calculate the eigenvalues of resulting PCs. PCs with eigenvalues that exceeded the 95th percentile of 1000 randomly seeded simulations were selected for PC axes.

2.5 References

1. D. J. Newman, G. M. Cragg, Natural Products as Sources of New Drugs from 1981 to 2014. *J Nat Prod* **79**, 629-661 (2016).
2. M. Miura, Therapeutic Drug Monitoring of Imatinib, Nilotinib, and Dasatinib for Patients with Chronic Myeloid Leukemia. *Biological & Pharmaceutical Bulletin* **38**, 645-654 (2015).
3. J. W. Lown, Discovery and development of anthracycline antitumour antibiotics. *Chemical Society Reviews* **22**, 165 (1993).
4. S. B. Horwitz, Taxol (paclitaxel): mechanisms of action. *Annals of oncology.* **5 Suppl 6**, S3-S6 (1994).
5. G. W. H. O. World Health Organization Model List of Essential Medicines – 22nd List, World Health Organization Model List of Essential Medicines. (2021).
6. N. Casares *et al.*, Caspase-dependent immunogenicity of doxorubicin-induced tumor cell death. *Journal of Experimental Medicine* **202**, 1691-1701 (2005).
7. L. Minute *et al.*, Cellular cytotoxicity is a form of immunogenic cell death. *Journal for ImmunoTherapy of Cancer* **8**, e000325 (2020).
8. I. Martins *et al.*, Premortem autophagy determines the immunogenicity of chemotherapy-induced cancer cell death. *Autophagy* **8**, 413-415 (2012).
9. M. Michaud *et al.*, Autophagy-Dependent Anticancer Immune Responses Induced by Chemotherapeutic Agents in Mice. *Science* **334**, 1573-1577 (2011).
10. L. Bezu *et al.*, eIF2α phosphorylation is pathognomonic for immunogenic cell death. *Cell Death & Differentiation* **25**, 1375-1393 (2018).
11. L. Aaes, Tania *et al.*, Vaccination with Necroptotic Cancer Cells Induces Efficient Anti-tumor Immunity. *Cell Reports* **15**, 274-287 (2016).
12. G. Sriram *et al.*, The injury response to DNA damage in live tumor cells promotes antitumor immunity. *Science Signaling* **14**, (2021).
13. J. Aurelius *et al.*, Anthracycline-based consolidation may determine outcome of post-consolidation immunotherapy in AML. *Leukemia & Lymphoma* **60**, 2771-2778 (2019).
14. M. Lecciso *et al.*, ATP Release from Chemotherapy-Treated Dying Leukemia Cells Elicits an Immune Suppressive Effect by Increasing Regulatory T Cells and Tolerogenic Dendritic Cells. *Front Immunol* **8**, 1918 (2017).
15. S. J. Park *et al.*, Cisplatin and oxaliplatin induce similar immunogenic changes in preclinical models of head and neck cancer. *Oral Oncol* **95**, 127-135 (2019).
16. S. J. Bains *et al.*, Immunogenic cell death by neoadjuvant oxaliplatin and radiation protects against metastatic failure in high-risk rectal cancer. *Cancer Immunology, Immunotherapy* **69**, 355-364 (2020).
17. L. Galluzzi *et al.*, Consensus guidelines for the definition, detection and interpretation of immunogenic cell death. *Journal for ImmunoTherapy of Cancer* **8**, e000337 (2020).
18. P. Liu *et al.*, Identification of pharmacological agents that induce HMGB1 release. *Scientific Reports* **7**, (2017).
19. C. Sansone *et al.*, Natural Compounds of Marine Origin as Inducers of Immunogenic Cell Death (ICD): Potential Role for Cancer Interception and Therapy. *Cells* **10**, (2021).
20. B. Xie *et al.*, High-throughput screening identified mitoxantrone to induce death of hepatocellular carcinoma cells with autophagy involvement. *Biochemical and Biophysical Research Communications* **521**, 232-237 (2020).

21. D. C. Earl *et al.*, Discovery of human cell selective effector molecules using single cell multiplexed activity metabolomics. *Nat Commun* **9**, 39 (2018).
22. L. Bezu *et al.*, eIF2α phosphorylation: A hallmark of immunogenic cell death. *OncoImmunology* **7**, e1431089 (2018).
23. C. Mauvezin, T. P. Neufeld, Bafilomycin A1 disrupts autophagic flux by inhibiting both V-ATPase-dependent acidification and Ca-P60A/SERCA-dependent autophagosome-lysosome fusion. *Autophagy* **11**, 1437-1438 (2015).
24. A. Yamamoto *et al.*, Bafilomycin A1 Prevents Maturation of Autophagic Vacuoles by Inhibiting Fusion between Autophagosomes and Lysosomes in Rat Hepatoma Cell Line, H-4-II-E Cells. *Cell Structure and Function* **23**, 33-42 (1998).
25. R. Wang *et al.*, Molecular basis of V-ATPase inhibition by bafilomycin A1. *Nature Communications* **12**, (2021).
26. P. Sehgal *et al.*, Inhibition of the sarco/endoplasmic reticulum (ER) Ca2+-ATPase by thapsigargin analogs induces cell death via ER Ca2+ depletion and the unfolded protein response. *Journal of Biological Chemistry* **292**, 19656-19673 (2017).
27. C. Xu, H. Ma, G. Inesi, M. K. Al-Shawi, C. Toyoshima, Specific Structural Requirements for the Inhibitory Effect of Thapsigargin on the Ca2+ ATPase SERCA. *Journal of Biological Chemistry* **279**, 17973-17979 (2004).
28. J. Lytton, M. Westlin, M. R. Hanley, Thapsigargin inhibits the sarcoplasmic or endoplasmic reticulum Ca-ATPase family of calcium pumps. *Journal of Biological Chemistry* **266**, 17067-17071 (1991).
29. T. Frank *et al.*, Cell cycle arrest in mitosis promotes interferon-induced necroptosis. *Cell Death & Differentiation* **26**, 2046-2060 (2019).
30. P. O. Krutzik, M. R. Clutter, A. Trejo, G. P. Nolan, Fluorescent Cell Barcoding for Multiplex Flow Cytometry. *Current Protocols in Cytometry* **55**, (2011).
31. J. H. Boyce, B. J. Reisman, B. O. Bachmann, J. A. Porco, Jr., Synthesis and Multiplexed Activity Profiling of Synthetic Acylphloroglucinol Scaffolds. *Angew Chem Int Ed Engl* **60**, 1263-1272 (2021).
32. B. J. Reisman, S. M. Barone, B. O. Bachmann, J. M. Irish, DebarcodeR increases fluorescent cell barcoding capacity and accuracy. *Cytometry Part A*, (2021).
33. P. O. Krutzik, G. P. Nolan, Fluorescent cell barcoding in flow cytometry allows high-throughput drug screening and signaling profiling. *Nature Methods* **3**, 361-368 (2006).
34. T. Hori, I. Maezawa, I. Nagahama, N. Suzuki, Isolation and structure of narbonolide, narbomycin aglycone, from Streptomyces venezuelae and its biological transformation into picromycin via narbomycin. *Journal of the Chemical Society D: Chemical Communications*, 304 (1971).
35. G. Amodio *et al.*, PERK-Mediated Unfolded Protein Response Activation and Oxidative Stress in PARK20 Fibroblasts. *Frontiers in Neuroscience* **13**, (2019).
36. A. L. Samson *et al.*, MLKL trafficking and accumulation at the plasma membrane control the kinetics and threshold for necroptosis. *Nature Communications* **11**, (2020).
37. E. A. Perez, Microtubule inhibitors: Differentiating tubulin-inhibiting agents based on mechanisms of action, clinical activity, and resistance. *Molecular Cancer Therapeutics* **8**, 2086-2095 (2009).
38. R. J. Vasquez, B. Howell, A. M. Yvon, P. Wadsworth, L. Cassimeris, Nanomolar concentrations of nocodazole alter microtubule dynamic instability in vivo and in vitro. *Molecular Biology of the Cell* **8**, 973-985 (1997).

39. M. Sauler, I. S. Bazan, P. J. Lee, Cell Death in the Lung: The Apoptosis–Necroptosis Axis. *Annual Review of Physiology* **81**, 375-402 (2019).
40. K. Moriwaki, F. K.-M. Chan, in *International Review of Cell and Molecular Biology*. (Elsevier, 2017), pp. 253-275.
41. K. Toriyama *et al.*, Azithromycin enhances the cytotoxicity of DNA-damaging drugs via lysosomal membrane permeabilization in lung cancer cells. *Cancer Science* **112**, 3324-3337 (2021).
42. K. Hirasawa *et al.*, Macrolide Antibiotics Exhibit Cytotoxic Effect under Amino Acid-Depleted Culture Condition by Blocking Autophagy Flux in Head and Neck Squamous Cell Carcinoma Cell Lines. *PLOS ONE* **11**, e0164529 (2016).
43. S. Mukai *et al.*, Macrolides sensitize EGFR-TKI-induced non-apoptotic cell death via blocking autophagy flux in pancreatic cancer cell lines. *International Journal of Oncology* **48**, 45-54 (2016).
44. M. B. Naeini, V. Bianconi, M. Pirro, A. Sahebkar, The role of phosphatidylserine recognition receptors in multiple biological functions. *Cellular & Molecular Biology Letters* **25**, (2020).
45. I. Shlomovitz, M. Speir, M. Gerlic, Flipping the dogma – phosphatidylserine in non-apoptotic cell death. *Cell Communication and Signaling* **17**, (2019).
46. F. Wallberg, T. Tenev, P. Meier, Analysis of Apoptosis and Necroptosis by Fluorescence-Activated Cell Sorting. *Cold Spring Harb Protoc* **2016**, pdb prot087387 (2016).
47. I. Martins *et al.*, Chemotherapy induces ATP release from tumor cells. *Cell Cycle* **8**, 3723-3728 (2009).
48. L. Menger *et al.*, Cardiac Glycosides Exert Anticancer Effects by Inducing Immunogenic Cell Death. *Science Translational Medicine* **4**, (2012).
49. B. O. Bachmann, S. G. Van Lanen, R. H. Baltz, Microbial genome mining for accelerated natural products discovery: is a renaissance in the making? *Journal of Industrial Microbiology and Biotechnology* **41**, 175-184 (2014).
50. E. Kenshole, M. Herisse, M. Michael, S. J. Pidot, Natural product discovery through microbial genome mining. *Curr Opin Chem Biol* **60**, 47-54 (2021).
51. A. Popat, A. Patel, G. Warnes, A Flow Cytometric Study of ER Stress and Autophagy. *Cytometry Part A* **95**, 672-682 (2019).
52. V. Viswesh, K. Gates, D. Sun, Characterization of DNA Damage Induced by a Natural Product Antitumor Antibiotic Leinamycin in Human Cancer Cells. *Chemical Research in Toxicology* **23**, 99-107 (2010).
53. R. Tang *et al.*, Ferroptosis, necroptosis, and pyroptosis in anticancer immunity. *Journal of Hematology & Oncology* **13**, (2020).
54. W. Han *et al.*, Autophagy Inhibition Enhances Daunorubicin-Induced Apoptosis in K562 Cells. *PLoS ONE* **6**, e28491 (2011).
55. C. Mauvezin, P. Nagy, G. Juhász, T. P. Neufeld, Autophagosome–lysosome fusion is independent of V-ATPase-mediated acidification. *Nature Communications* **6**, 7007 (2015).
56. Y. Wang *et al.*, Autophagy induction by thiostrepton improves the efficacy of immunogenic chemotherapy. *J Immunother Cancer* **8**, (2020).
57. G. Runwal *et al.*, LC3-positive structures are prominent in autophagy-deficient cells. *Scientific Reports* **9**, (2019).

58. M. Schoof *et al.*, eIF2B conformation and assembly state regulate the integrated stress response. *eLife* **10**, (2021).
59. T. Adomavicius *et al.*, The structural basis of translational control by eIF2 phosphorylation. *Nature Communications* **10**, (2019).
60. Y. Gordiyenko, J. L. Llácer, V. Ramakrishnan, Structural basis for the inhibition of translation through eIF2α phosphorylation. *Nature Communications* **10**, (2019).
61. K. Weber, R. Roelandt, I. Bruggeman, Y. Estornes, P. Vandenabeele, Nuclear RIPK3 and MLKL contribute to cytosolic necrosome formation and necroptosis. *Communications Biology* **1**, (2018).
62. M. Murphy, James *et al.*, The Pseudokinase MLKL Mediates Necroptosis via a Molecular Switch Mechanism. *Immunity* **39**, 443-453 (2013).
63. D. A. Rodriguez *et al.*, Characterization of RIPK3-mediated phosphorylation of the activation loop of MLKL during necroptosis. *Cell Death & Differentiation* **23**, 76-88 (2016).
64. F. Meggio *et al.*, Different Susceptibility of Protein Kinases to Staurosporine Inhibition. Kinetic Studies and Molecular Bases for the Resistance of Protein Kinase CK2. *European Journal of Biochemistry* **234**, 317-322 (1995).
65. I. M. Smith, N. Hoshi, ATP Competitive Protein Kinase C Inhibitors Demonstrate Distinct State-Dependent Inhibition. *PLoS ONE* **6**, e26338 (2011).
66. F. Y. Glassman *et al.*, Phosphatidylserine Is Not Just a Cleanup Crew but Also a Well-Meaning Teacher. *Journal of Pharmaceutical Sciences* **107**, 2048-2054 (2018).
67. J. L. Schneider, S. V. Balu-Iyer, Phosphatidylserine Converts Immunogenic Recombinant Human Acid Alpha-Glucosidase to a Tolerogenic Form in a Mouse Model of Pompe Disease. *Journal of Pharmaceutical Sciences* **105**, 3097-3104 (2016).
68. S. Yoon, A. Kovalenko, K. Bogdanov, D. Wallach, MLKL, the Protein that Mediates Necroptosis, Also Regulates Endosomal Trafficking and Extracellular Vesicle Generation. *Immunity* **47**, 51-65 e57 (2017).
69. A. Q. Sukkurwala *et al.*, Screening of novel immunogenic cell death inducers within the NCI Mechanistic Diversity Set. *OncoImmunology* **3**, e28473 (2014).
70. I. Martins *et al.*, Molecular mechanisms of ATP secretion during immunogenic cell death. *Cell Death & Differentiation* **21**, 79-91 (2014).
71. N. Kotecha, P. O. Krutzik, J. M. Irish, Web-Based Analysis and Publication of Flow Cytometry Experiments. *Current Protocols in Cytometry* **53**, 10.17.11-10.17.12 (2010).

CHAPTER 3 - Bioactivity Guided Isolation of Secondary Metabolites

3.1 Introduction

An array of techniques has been empirically determined to substantially increase cryptic and/or relatively silent secondary metabolite biosynthesis in actinomycetes. It has long been recognized that varying media composition effects production of secondary metabolites. Subsequently it was demonstrated that discrete chemical and biological stimuli can be used to encourage transcription of typically quiescent biosynthetic gene clusters towards translation of the enzymes necessary for synthesis of unique secondary metabolites. These stimulations include

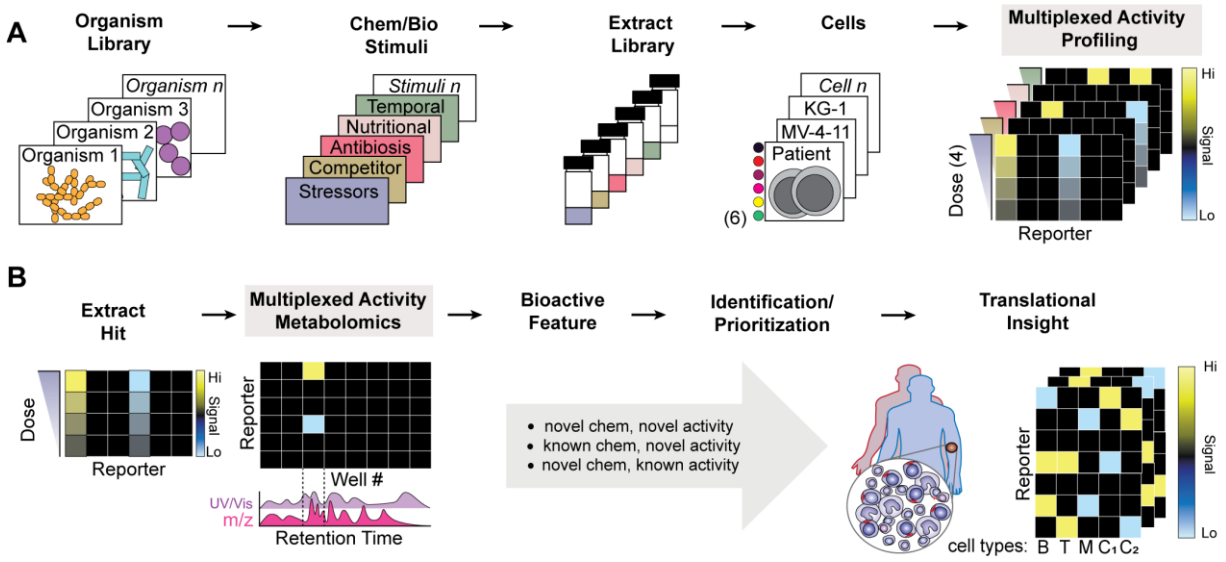

Figure 3.1. Natural product bioeffector discovery informed by mammalian cell phenotypes prioritizes interrogation of secondary metabolites. (A) Actinobacteria are cultured in diverse chemical and biological stimuli to potentiate secondary metabolite biosynthesis. Metabolites are extracted for challenge in human primary cell samples or cancer cell lines. Samples are hyper-multiplexed via fluorescent cell barcoding (FCB) to simultaneously acquire extract-specific, dose-dependent activity in six fluorescence reporter assays (6) to detect phenotypic shifts in single cell populations. This enables hyper-multiplexing of 288 discrete experiments in a single test tube. **(B)** Extracts presenting titrable, reporter activity are fractioned and collected in plate wells by split flow HPLC-MS-UV/Vis to multiplex fluorescent reporters with salient metabolomic features (Multiplexed Activity Metabolomics - MAM). MAM coordinates well number associated fractions with HPLC retention time. MAM active extracts are prioritized for identification of the assay sensitive natural product. New and known scaffolds are prioritized by literature precedent for advancement to patient primary cell assays for interrogation of bioeffector potential in healthy donor and cancer patient cell subsets. B = B cells, T = T cells, M = Monocytes, C1/C2 = Cell subtype 1/2.

culturing actinomycetes with sub-inhibitory concentrations of antibiotics (*1, 2*), rare earth elements, co-culture with competing organisms, and de-repression via selection of antibiotic resistance. Development of high throughput methodologies has enabled the screening of hundreds of culture conditions for the ability to induce secondary metabolism and comparative metabolomics has facilitated the rapid assessment of differences among perturbed systems to aid in identification of novel secondary metabolites in an activity-independent fashion (*3-6*). In these abundance-first isolation workflows, determination of activity occurs after the isolation of upregulated, abundant, chromatographically tractable chemical species.

This work provides a methodology for discovery of bioactive secondary metabolites by measuring biological responses in single cells to the presence of complex chemical metabolomes. The quantitative single cell chemical biological analytical tools described herein leveraged fluorescent flow cytometry to efficiently identify microbial extracts, metabolomic fractions, and compounds that impact critical cellular processes in addition to causing overt cytotoxicity in human-derived cell lines. These assays, termed multiplexed activity profiling (MAP) (*7*) and multiplexed activity metabolomics (MAM) (*8*), evaluate single cell responses to metabolite challenge with fluorescent cell barcoding (FCB) (*9, 10*) and fluorescent functional readouts. The MAP assay screens for dose-dependent bioactivity in crude extracts while the MAM assay fractions the bioactive extract into a comprehensive metabolomic array to reveal the bioactive component(s) within the complex chemical mixture. Chemically dependent responses in single cells are acquired with flow cytometry and the biological data is deconvoluted with the DebarcodeR algorithm to enhance and automate computation of biological activity (*11*). This suite of tools can be used for diverse applications in the discovery of bioeffectors from virtually any source ranging from compound libraries to the products of primary and secondary metabolism. As

part of a survey of hypogean-sourced actinomycetes, organisms were sourced from a local cave, isolated by culture with selective media (*12*, *13*), and cultivated in the presence of chemical and biological stimuli to encourage secondary metabolite biosynthesis (*1*, *3*, *14*, *15*). The resulting metabolomes were extracted to determine the efficacy of stimulus specific bioactivity in an array of serially diluted extracts with MAP. Follow up analysis of a growth conditions possessing dilutable activity in extracts was performed using MAM to identify bioactive components for isolation and dereplication. This workflow identified the pyridine-pyrrolidine siderochelin by DNA damage response markers and a family of natural products was identified that did not exhibit

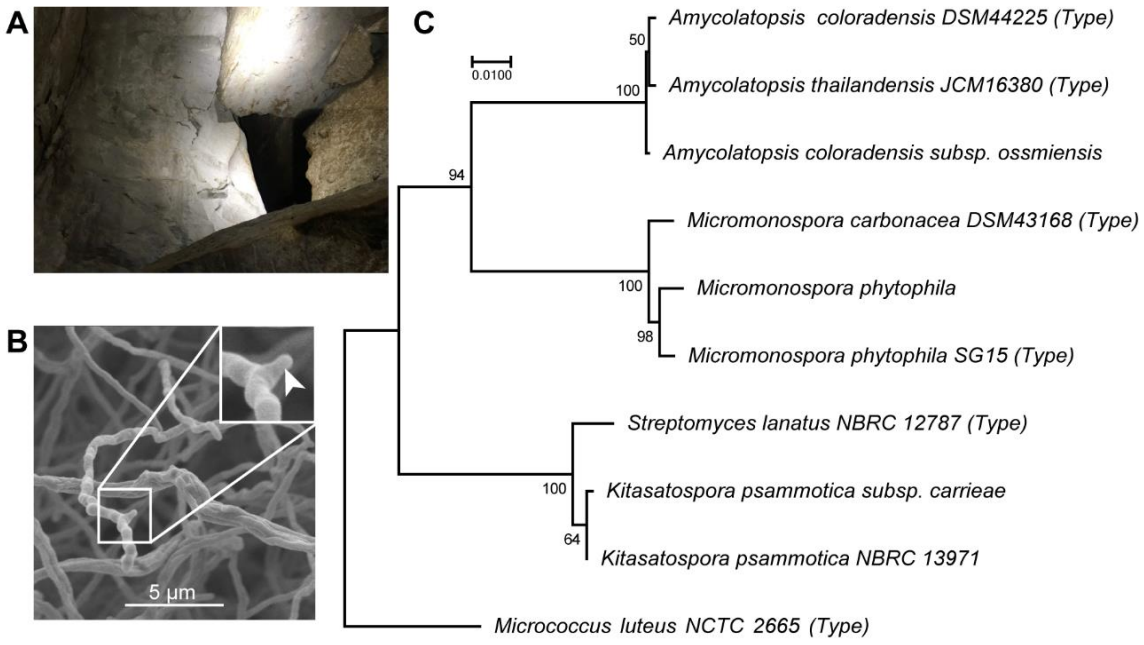

Figure 3.2. Caves are an ecological niche for new actinomycetes. (A) Passage within Blue Springs Cave. (B) Scanning electron micrograph of aerial hyphae and smooth tendrils with dull protrusions that lack clearly defined sporangia. White arrowhead in inset B indicates dull protrusion. (C) The evolutionary history was inferred by using the Maximum Likelihood method and Tamura-Nei model. The tree with the highest log likelihood (-3932.17) is shown. Initial tree(s) for the heuristic search were obtained automatically by applying Neighbor-Join and BioNJ algorithms to a matrix of pairwise distances estimated using the Maximum Composite Likelihood (MCL) approach, and then selecting the topology with superior log likelihood value. The tree is drawn to scale, with branch lengths measured in the number of substitutions per site. This analysis involved ten nucleotide sequences. There were a total of 1537 positions in the final dataset. Evolutionary analyses were conducted in MEGA 7.

a shift in diagnostic injury markers but did enhance cytotoxicity. Isolation and structure elucidation identified three chemically active compounds belonging to the filipin family as well as a novel filipin not previously reported. Flow cytometry confirmed filipin cytotoxicity occurs independently of the apoptotic maker cleaved caspase (cCAS3) and fluorescent imaging illuminated that the known cholesterol mediated membrane-disrupting mechanism of filipin macrolides can be ablated by hydroxylation of the pendant alkyl chain.

3.2 Results

3.2.1 Prioritizing bioeffector isolation from complex metabolic extracts

To drive discovery of natural product bioeffectors a function-centric (*16*), or phenotypic, screen that leverages single cell methods (*8, 17*) to coordinate stimulus conditions, dose-response data, and fluorescent reporter assays for genetic-free interrogation microbial extracts from diverse culture collections (Figure 3.1A) was developed .The Vanderbilt Laboratory for Biosynthetic Studies actinobacteria collection houses >500 actinomycetes purified by restrictive culturing methods (*18, 19*) from cave ecosystems, an under-utilized source of diverse actinomycete genera (*20, 21*) with nascent biosynthetic potential (*18, 20, 22, 23*). Following phylogenetic assessment

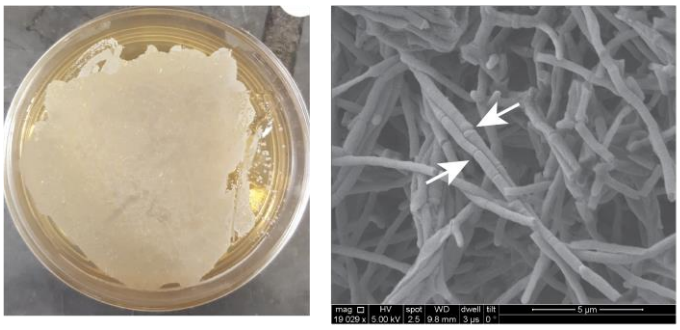

Figure 3.3. *A. coloradensis* ssp. *ossimia* cultured on ISP-2 agar is white and opaque. Scanning electron microscopy reveals rod-like spores with clear segmentation.

by 16s DNA sequences, microbes are engaged by chemical and biological stimulus (Figure 3.1A) in liquid cultures to unlock stimulus sensitive secondary metabolite biosynthesis (*18, 22, 24-29*). Broth and biomass were extracted with HP20/Methanol/Acetone and cataloged in extract libraries (Figure 3.1A). Extracts were serially diluted sixty-four-fold on ninety-six well plates, dried *in vacuo*, and dissolved in cancer cell line containing culture media (Figure 3.1A) for overnight incubation. Cells were then prepared for fluorescent cell barcoding and flow cytometry to acquire dose-dependent shifts in functional response markers with respect to extract using MAP (Figure 3.1B). Bioactive compounds detected by MAP were advanced to MAM to detect well specific bioactivity and identify candidate compounds for isolation with complementary mass spectrometry and UV/Vis spectra. Identified compounds are prioritized by scaffold novelty. For example, a new scaffold with biological activity would undergo immediate evaluation in patient or healthy donor primary cell samples to elucidate cell subset specific phenotypic augmentations. Additionally, novel or rediscovered analogs of known chemical scaffolds are compared to literature precedents of established utility and prioritized for downstream applications dependent on activity. As example, an anthracycline analog that induced a unique biological phenotype would be prioritized over an iron chelating compound on the precedent that anthracyclines are a mainstay chemotherapy across clinical indications (Figure 3.1B).

In doing so, cell type specificity and phenotypic endowment via natural products in specific cell subsets of heterogeneous patient cell populations was established. The first organism, *Amycolatopsis coloradensis* synthesized the pyridine-pyrrolidine alkaloid siderochelin (*30, 31*) which impacted DNA damage and translation response pathways. The second organism, *Streptomyces psammoticus* synthesized new members of the filipin family (*32-34*) of polyene macrolides.

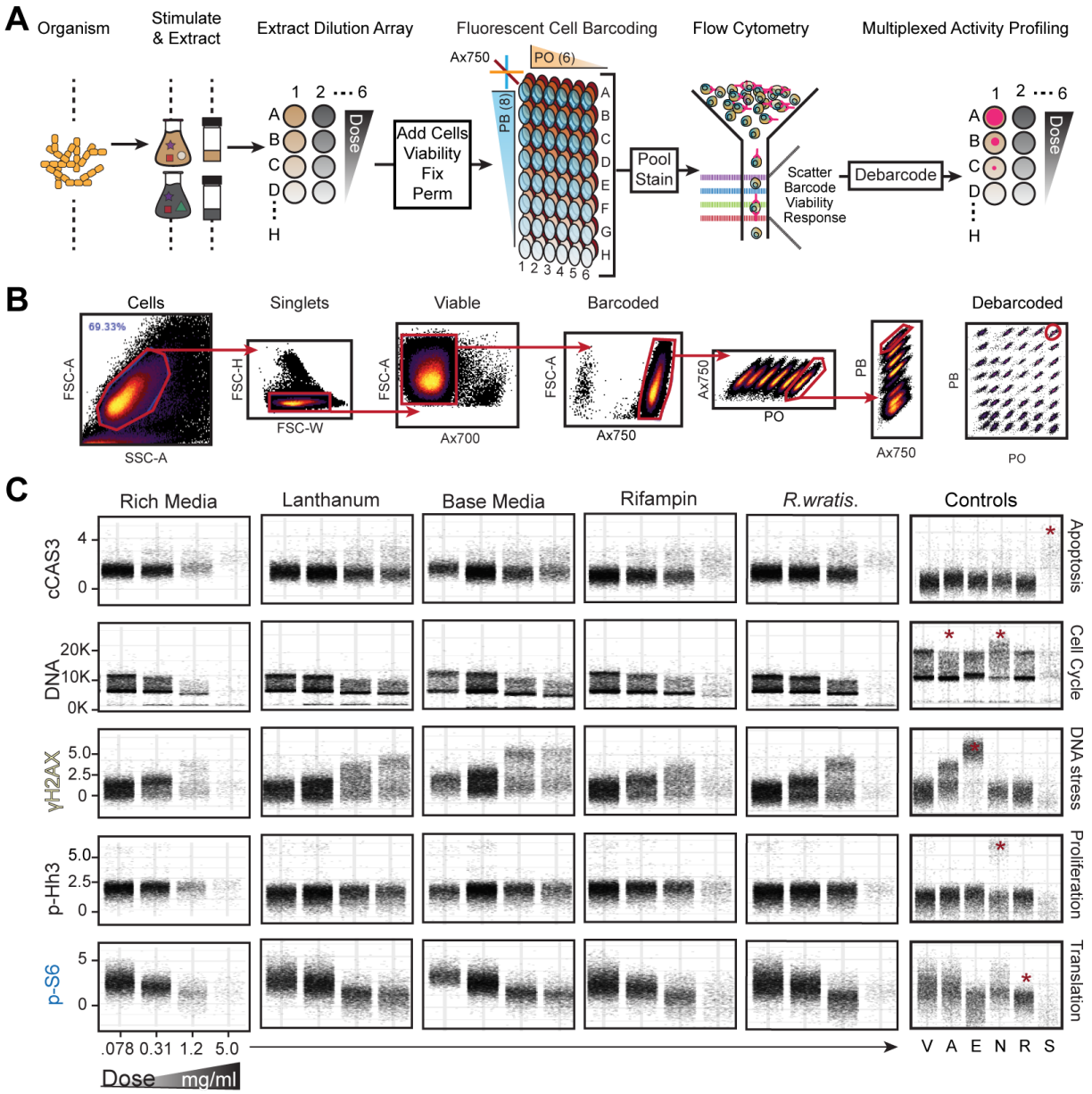

Figure 3.4. Multiplexed activity profiling identifies novel activity of siderochelin synthesized by *A. colordensis*. (A) Organisms are stimulated by media additions for one week, extracted, dose titrated, and dried in vacuo. Extracts are resuspended in cell containing media for overnight challenge. Cells are stained for viability then fixed, permeabilized and fluorescently barcoded. Barcoded cells are pooled, and stained with fluorescent reporter cocktail for signal acquisition by flow cytometry. Cell populations are digitally reassigned to origin wells by fluorescent barcode and assessed for dilutable bioactivity. (B) Fluorescent cell barcodes and reporters are assessed for all experimental conditions simultaneously by flow cytometry. Intact, single cell populations are gated for and non-viable cells (Ax700+) excluded from analysis. As shown, cells are separated by six levels of pacific orange, each embedded with eight levels of pacific blue. Cells are digitally reassigned to plate wells by debarcoding using the R script debarcodeR. Red gating highlights isolation of a singly barcoded cell population. (C) Hyperplexed data is evaluated as single cell (black dots) dose response (X axis) plots of measured fluorescent intensity (left y axis) of each reporter assay (right y axis). A hit is exhibited in γ-H2AX (yellow text) in lanthanum and base media extracts evidenced by enhanced γ-H2AX fluorescent detection consistent with increased dose. Additionally, p-S6 (blue text) fluorescent intensity is suppressed in a dose dependent fashion. Assay fidelity is evaluated by internal compound controls that stimulate at least one bioactivity marker indicated by red asterisks. V = Vehicle, A = Aphidicolin, E = Etoposide, N = Nocodazole, R = Rapamycin, S = Staurosporine

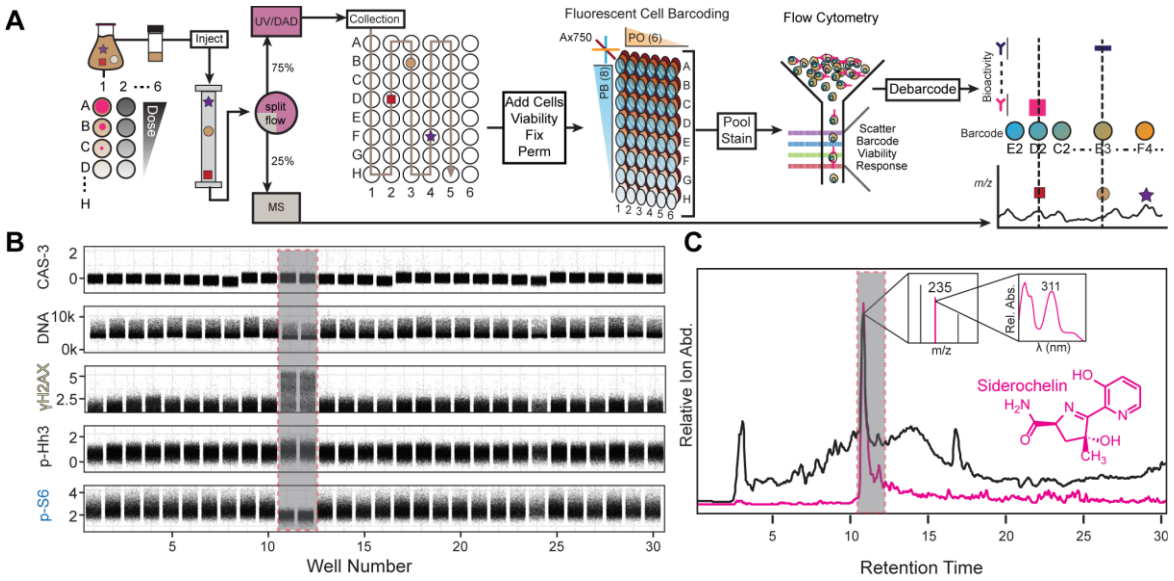

Figure 3.5. MAM aligns bioactivity in fractioned metabolotmes with spectral data to inform secondary metabolite isolation. (A) Hit extracts are fractioned by split flow HPLC-MS-UV to acquire mass spectra with tandem UV spectra localized to individual wells consistent with retention time (e.g. Well 11 contains all eluates from time 10:00 - 10:59). Fractioned metabolomes are dried in vacuo, resuspended in cell containing media, and processed. Cells are viability stained, fixed, permeabilized, fluorescently barcoded, pooled, stained, and aquired by flow cytometry. (B) Cell populatinos are debarcoded to assess bioactivity cooridinated with spectral data to prioritize bioactive secondary metabolites for isolation. A hit extract from A. coloradensis tested with MAM resolved specific activity in wells 11 and 12 via increased γH2AX and diminished p-S6. (C) Wells expressing fluorescent reporter shifts in cell populations are referenced to retention time for spectral features to prioritize bioeffectors for dereplication. Total ion current (black trace) presents a large peak aligned with observed reporter activity. Positive extracted ion current (magenta trace) of m/z 235.# and absorbance maxima of 311 nm were isolated and dereplicated to the natural product siderochelin.

3.2.2 Different genera of actinobacteria were isolated from a cave environment

Actinobacteria species were isolated from cave sediment obtained from Blue Springs Cave, Tennessee (Figure 3.2A) via dilution plating on agar media. One isolated actinobacteria developed into an orange lawn with white puncta on ISP-2 agar and formed cylindrical aerial hyphae with smooth spore chains dotted with protruding nodules (Figure 3.2B) and another developed into a white lawn with segmented spores (Figure 3.3). The 16S ribosome gene sequence was used to infer the evolutionary history of this species by bootstrapping 1000 maximum likelihood projections in MEGA 7 (*35*) of 16S ribosomal DNA sequence alignment with closest relatives predicted by EZBiocloud's 16S-based (*36*) ID search algorithm and 16S sequences of genera type strains from *Streptomyces*, *Micromonospora*, and *Amycalatopsis* (Figure 3.2C). EZBioCloud identified

Kitasatospora psammotica (99.93 % similarity, basonym *Streptomyces psammotica*) (*37, 38*) as the closest evolutionary relative consistent with the phylogenetic tree (Figure 3.2C).

3.2.3 Isolation of siderochelin from *A. colorodensis*

This organism was cultured in diverse media conditions to encourage biosynthesis of genetically encoded natural products. Following incubation, secondary metabolites were harvested and prepared for MAP (Figure 3.4A). Following data acquisition, viable, singlet cells were reassigned to their original well coordinates by fluorescent barcode (Figure 3.4B). The phenotypic marker for DNA damage responses, y-H2AX (*39*), exhibited elevated single-cell fluorescent shifts consistent with increased dose across stimuli (Figure 3.4C). Additionally, S6 phosphorylation was steadily suppressed with increasing dose (Figure 3.4C). In all, this single cell data indicated *A. coloradensis* synthesized a natural product across chemical and biological stimulus that effected DNA damage response and translation status in MV-4-11 cell line (Figure 3.4C). We confirmed these interpretations by comparing experimental samples to known bioeffector natural product positive controls (Figure 3.4C).

Following discovery by MAP activity the *A. colordensis* extract was advanced to MAM for identification of bioactivity in specific plate wells and align that activity to the mass spectra to search for compounds for isolation that may the active component in the whole extract. Figure 3.5 demonstrates typical coordination of single cell fluorescent data to associated mass spectra and UV/Vis absorbance. MAM of hit extract from *A. coloradensis* (Figure 3.5) revealed isolated increase of γH2AX and decrease of p-S6 fluorescent intensities in wells 11 and 12 (Figure 3.5B) consistent with preliminary screening data (Figure 3.4C). Extract mass chromatograms highlighted an abundant total ion current peak residing across retention times 10:00-11:59 (Figure 3.5C). A number of ions were present in any given well; therefore, candidate *m/z* ion currents were extracted

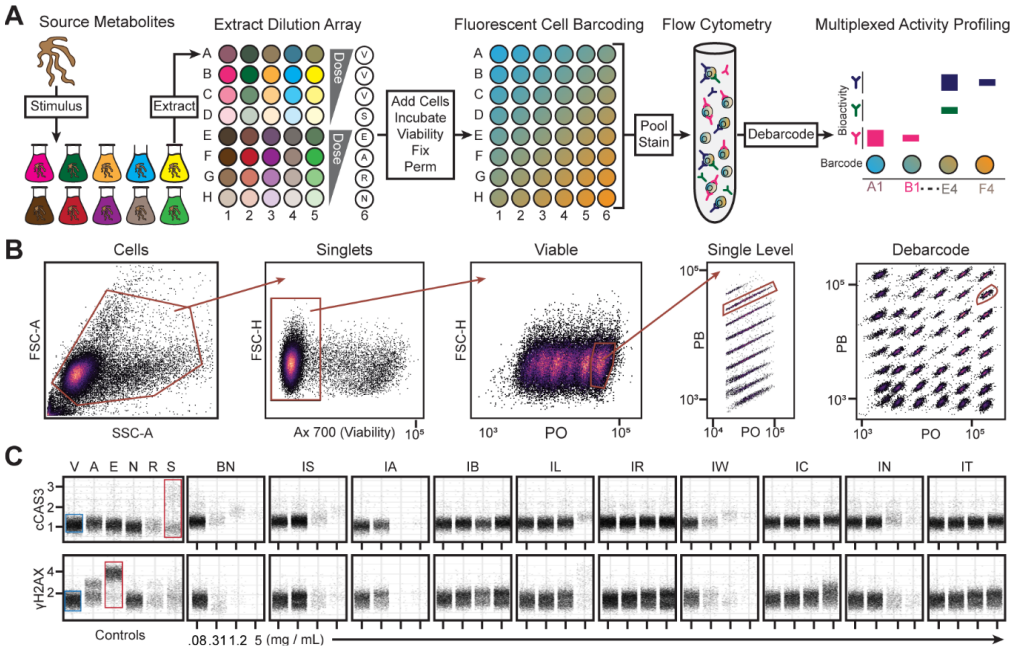

Figure 3.6. Multiplexed activity profile of single cells challenged with metabolomes from actinomycetes cultured in diverse stimuli. (A) Harvested actinomycetes were incubated in the presence of diverse stimuli and then secondary metabolites extracted for bioactivity dose response in MV-4-11 cell line. Following incubation, cells were viability stained with Ax700, fixed with PFA, permeabilized with methanol, and fluorescently barcoded. Fluorescent cell barcoding is used to conserve well position through processing and analysis with NHS-functionalized, primary amine reactive Pacific Blue and Pacific Orange fluorescent dyes. Eight concentrations of PB are arrayed with six concentrations of PO to create 48 unique fluorescent identities that encode each well position. Barcoded cells are pooled and stained with a fluorescent antibody cocktail to measure molecular readouts with flow cytometry. Cells are digitally reasssinged to well position via fluorescent barcode with DebacodeR algorithm. Extracts, well position, fluorescent barcode, and molecular readouts are combined to produce a multiplexed activity profile to assess bioactivity. (B) Quality control gating scheme of MAP assay. Collected events were gated by forward and side scatter to identify cells, forward scatter height for single cells, and Ax700 for viability. Six concentrations of pacific orange are encoded in the viable, singlets cells and each pacific orange concentration encodes eight pacific blue concentrations to identify cell populations by fluorescent barcode. A single cell population is tracked by the red gates and is identified in the debarcoded cell populations. (C) Multiplexed activity profile of S. psammotiucs ssp carrie cultured in diverse stimuli. Each black dot represents a single cell response at the observed dose and are compared to specific positive control compounds (red box) to infer single cell marker shifts versus vehicle control (blue box). This organism produced a cytotoxic compound that did not increase the number of apoptotic cells measured as the arcsinh ratio of median fluorescent intensity versus vehicle control but exhibited cytotoxic effects visualized by decreased viable cell populations. V = Vehicle, A = Aphidicolin, E = Etoposide, N = Nocodazole, R = Rapamycin, S = Staurosporine, PB = Pacific Blue, PO = Pacific Orange, BN = Bennet's media, IS = ISP2, IA = ISP2-agar, IB = ISP2-B. subtilus, IL = ISP2-LaCl3, IR = ISP2-Rifampin, IW = ISP2-Rhodococcus wratislaviensis, IC = ISP2-Escherchia coli, IN = ISP2-Streptomycin, IT = ISP2-Tsukamorella pneumonia.

to confirm localized secondary metabolites consistent with bioactivity data and then inspected for UV/Vis absorbance (Figure 3.5C). Extracted ion current of *m/z* 235 from *A. coloradensis* aligned to wells 11 and 12 and exhibited a local UV/Vis absorbance maximum of ~311 nm (Figure 3.5C). The active chemical agent responsible for phenotypic shifts in figure 5 was purified by combination of LH20 and preparative & analytical HPLC, then identified as the known natural

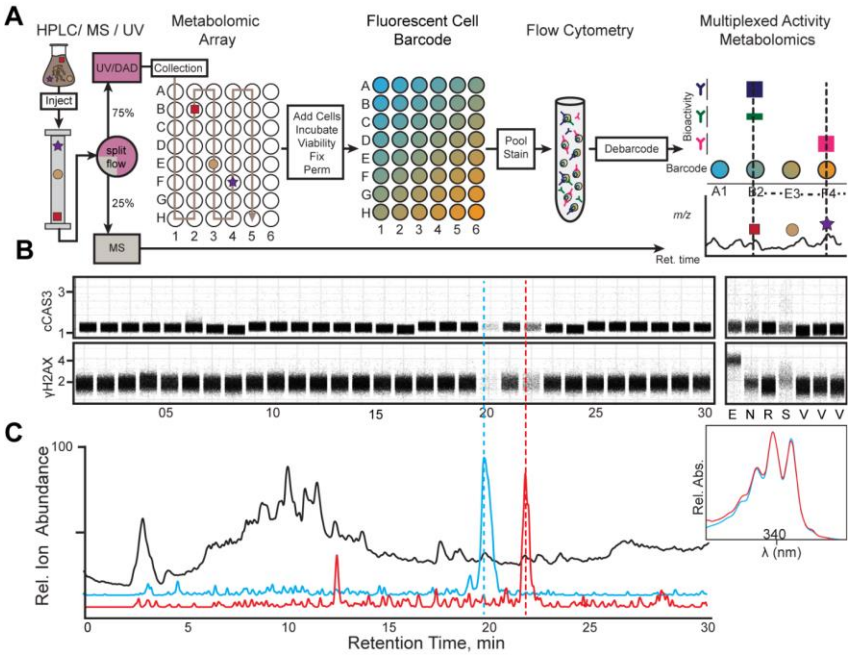

Figure 3.7. Multiplexed activity metabolomics identifies candidate bioactive compounds from single cell data. (A) Whole metabolomes from active MAPs are fractionated into a metabolomic array with split flow (3:1) HPLC/UV/MS system. One-minute metabolomic fractions are collected in 48 wells, dried in vacuo, and resuspended in media containing cells. Cells are incubated, fixed in PFA, permeabilized in methanol, fluorescently barcoded, pooled, stained, flowed, and debarcoded and compared to marker shifts and spectral data to determine well fractions with potential for isolating a bioactive secondary metabolite. The single cell response profile of S. carrieae metabolomic fractions reveals cells loss in fractions 20 and 22. (C) Active metabolomic fractions are cross referenced against complementary mass spectral data (total ion current – orange trace) to identify candidate natural products for isolation. Candidate ion currents are extracted to observe temporal relationships to observed bioactivity. Extracted ion currents of 625.39 (blue trace) and 661.39 (red trace) highlight candidate bioactive compounds that elute at minutes 20 (blue trace) and 22 respectively.

product siderochelin (Figure 3.5C). The first of the siderochelin family of compounds was isolated from Nocardia and described as a ferrous ion chelating agent with weak antibiotic activity (*40*). Additional analogs with similar metal chelating properties have been isolated; however, reported antibiotic properties are consistently weak (*40-42*). To our knowledge, this is the first report of any siderochelin analog imposing diverse phenotypic changes in mammalian cancer cell models, let alone at the post-translational modification level.

3.2.4 Cytotoxicity can occur without marker shift

The MAP method was used to test a dilution series of crude metabalomic extracts from *K. psammotica* cultured under chemical and biological stimuli to identify dose-dependent responses of diverse cell status markers (Figure 3.6). *K. psammotica* was cultivated under ten distinct stimulus conditions, including solid and liquid media (ISP-2 and Bennett's media), in the presence of competitive microorganisms (*B. subtilus*, *R. wratislavensis*, *T. pneumonia* and *E. coli*), in the presence of sub-inhibitory concentrations of antibiotics (rifampin and streptomycin) and in the presence of lanthanide salts ($LaCl_3$) (*1, 3, 14, 15, 23*). The resultant metabolomes were extracted, diluted 64-fold across four wells in microtiter plates, and lyophilized to yield an extract dilution array (Figure 3.6A). Metabolites were resuspended in cell culture media containing MV-4-11 AML cells at a density of 1 million/mL and incubated overnight for 16 hours. After incubation cells were stained with a fluorescent Alexa 700 dye to label non-viable cells and measure overt

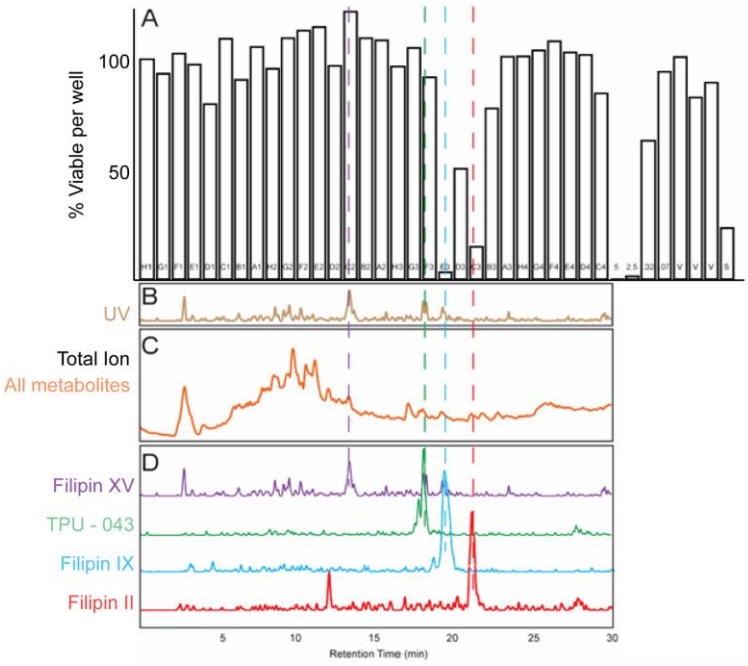

Figure 3.8. MAM Alignment of extracted ion currents of filipin compounds with plate well. (A) Viable percent of cells per well normalized to vehicle control. (B) UV absorbance spectra. (C) Total ion current of all detected metabolites. (D) Extracted ion currents of each filipin family membered aligned with total ion current, UV, and well position.

cytotoxicity, then fixed in paraformaldehyde to memorialize cell status, and finally permeabilized in methanol to enable fluorescent antibody and fluorescent dye infiltration for detection of intracellular targets including cCAS3 (apoptosis), γH2AX (DNA damage), DNA (cell cycle), p-S6 (translation) and p-Hh3 (proliferation). Cells were fluorescently barcoded with an array of *N*-hydroxy succinimide ester-functionalized amine reactive fluorescent dyes composed of eight concentrations of Pacific Blue (one per row, A-H) and six concentrations of Pacific Orange (one per column, 1-6) to yield 48 well-specific fluorescently labeled cell populations (Figure 3.6A). The barcoded cells were pooled and stained with a fluorescent module composed of antibodies and a DNA intercalator to detect bioactivity. Barcode and marker signal intensity are then acquired simultaneously with flow cytometry (Figure 3.6A). Following signal acquisition, intact cells and singlet cell populations were gated for by forward and side scatter parameters then gated for viable, Ax700 negative cells (Figure 3.6B). Cells were debarcoded with the DebarcodeR algorithm to coordinate FCB cell populations by fluorescent intensity of each barcode dye for digital reassignment to the original plate well (Figure 3.6B). Conventional, non-viable cells are excluded from analysis due to inconsistent reactions with fluorescent NHS-dyes and fluorescent antibodies that confound debarcoding and overall data interpretation. Cells were phenotypically evaluated by inspecting bioactivity trends to determine bioeffector potential of each extract. *K. psammotica* extracts markedly reduced viable cell populations in the absence of functional marker shifts cross-referenced to bioactivity observed in positive control conditions: Staurosporine – cCAS3, Etoposide – gH2AX, Aphidicolin – DNA(G1) Rapamycin – p-S6, Nocodazole – p-HH3, DNA (G2) (Figure 3.6C). For example, metabolites harvested from ISP-2 liquid culture exhibited cell loss at 1.2 mg/mL and 5 mg/mL extract doses as a consequence non-viable cell removal (Figure 3.6C) but failed to enhance fluorescent signal of cell status markers comparable to staurosporine

or etoposide controls (Figure 3.6C). Moreover, extracts taken from certain stimuli conditions failed to invoke overt cytotoxicity including co-culture with *B. subtilis* and exposure to sub-lethal doses of rifampin antibiotic (Figure 3.6C). It is worth noting that the control compound staurosporine elicits an apoptotic cCAS3 response that can exhibit diminished cell populations relative to other compound controls as apoptotic cells with advanced membrane degradation are labeled non-viable by Ax700 and excluded from analysis (Figure 3.6C). Conversely, etoposide challenged cells exhibited robust γH2AX DNA damage response without concomitant cell loss due to membrane disruption (Figure 3.6C). Taken together, selective media can stimulate or abolish synthesis of cytotoxic agents by *K. psammotica* that permeabilized cell membranes within 16 hours of challenge (Figure 3.6C). Additionally, the effect was observed at extract doses as minimal as 0.31 mg/mL (Figure 3.6C), which emboldened the decision to isolate and elucidate the bioactive agent(s) from *K. psammotica*.

3.2.5 Multiplexed activity metabolomics detects bioactivity in discrete metabolic fractions

To identify the secondary metabolite(s) responsible for cytotoxic cell phenotypes, the *K. psammotica* metabolome was fractioned by reverse phase chromatography connected to a split-flow polarity-switching electrospray mass spectrometric analyzer (ESI-MS) and a UV/ VIS photodiode array detector (Figure 3.7A). The ESI-MS portion is sacrificed to acquire mass bioactive fractions with complementary spectral data to inform isolation of active secondary metabolites. The *K. psammotica* metabolomic array was lyophilized and resuspended in cell-containing media for incubation and subsequent processing with FCB, fluorescent staining, and debarcoding to identify well-specific bioactivity aligned with coordinated, discrete regions of the mass spectra (Figure 3.7A). Two compounds were detected that exhibited striking cytotoxicity in fractions 20 and 22 inferred by reduced viable (Ax700 negative) cell populations to 4.4 % and 17.2

% respectively yet failed to induce a measurable shift in cCasp3, DNA, γ-H2AX, p-Hh3, or p-S6 marker relative to controls in MV-4-11 cell line following 16-hour incubation (Figure 3.6 and Figure 3.7B). The bioactivity profiles were compared to liquid chromatography/mass spectrometry (LC/MS) data to identify and extract well-localized ion currents to observe relative abundance of metabolites for isolation. This yielded discovery of two secondary metabolites with an *m/z* 625.4 in fraction 20 and *m/z* 639.4 in fraction 22 (Figure 3.7C and Figure 3.8A). The UV/Vis spectral data of these secondary metabolites showed local UV maxima from 320 - 360 nm consistent with the family of polyene antibiotics (Figure 3.8B). Inspection for compounds with similar UV spectra identified two additional inactive polyenes in fractions 14 and 19 with positive extracted ion currents of *m/z* 627.4 and *m/z* 611.4 respectively (Figure 3.8C-D).

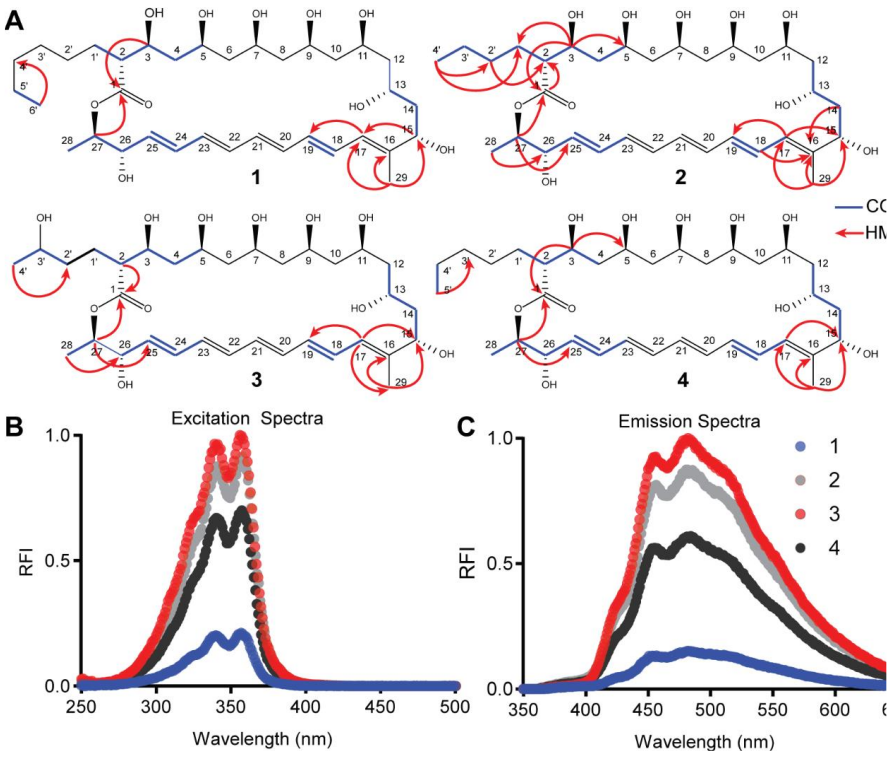

Figure 3.9. Structural assignment, exact mass, and spectral profiles of isolated filipin metabolites. (A) (1) Filipin II; 639.41082 (2) TPU-043; 611.37952 (3) Filipin XV; 627.37444 (D) Filipin IX; 625.39517. (E) Excitation spectra of isolated filipin compounds. (B) Excitation spectra of isolated filipin compounds. (C) Emission spectra of isolated filipin compounds. Blue = COSY correlation, Red = HMBC correlation, Purple = COSY and HMBC correlation.

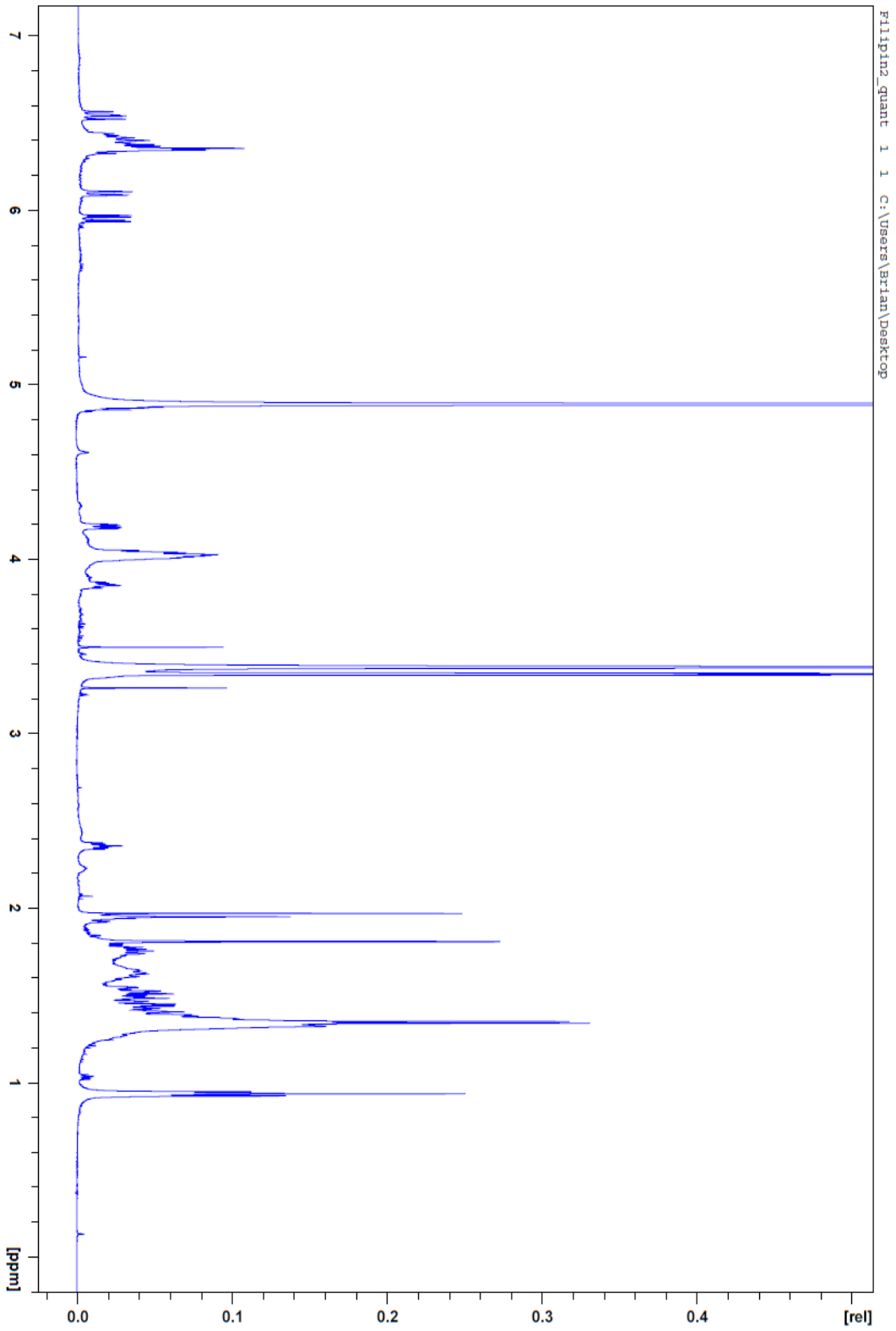

Figure 3.10. Filipin II ^{1}H NMR

Pos.	Proton	Carbon	COSY	HMBC
1	N/A	174		2, 27
2	2.35 (m)	52.9	3, 1'	
3	3.85 (m)	72	2,4	1
4	1.43 (m)	41.1	3, 5	
5	4.04 (m)	71.8		
6	1.34-1.52 (m, 2H)	41-43.5		
7	4.04 (1H, m)	71.8		
8	1.34-1.52 (m, 2H)	41-43.5		
9	4.04 (1H, m)	71.8		
10	1.34-1.52 (m, 2H)	41-43.5		
11	4.04 (1H, m)	69.5		
12	1.75, 1.49 (2H, m)	43.6		
13	3.35 (1H, m)	66.1	14, 12	
14	1.76, 1.93 (2H, m)	41.2	15, 13	
15	4.19 (1H, dd, 4.3, 10.3)	74.2	14	
16	N/A	139.4		29
17	6.10 (1H, d, 11.2)	126.6	18, 29	29, 15, 19
18	6.54 (1H, dd, 11.3, 14.4)	128.1	19, 17	
19	6.36 (1H, m)	132.7	18	
20	6.35-6.43 (1H, m)	132.7		
21	6.35-6.43 (1H, m)	132.7		
22	6.35-6.43 (1H, m)	132.7		
23	6.34 (1H, m)	132.7		
24	6.41 (1H, m)	132.3	25, 23	25, 23
25	5.95 (1H, dd, 5.8, 14.8)	132.7	26, 24	26, 24
26	4.04 (m)	72.8		
27	4.86 (1H, m)	73.1	28, 26	1, 26
28	1.33 (m, 3H)	16.9	27	
29	1.80 (3H, s)	10.1	17	15, 17, 16
1'	1.61, 1.72 (m)	28.8	2	
2'	1.25-1.34 (m, 2H)	26.9		
3'	1.35 (2H, m)	28.8		
4'	1.31 (2H, m)	31.4		
5'	1.39 (2H, m)	22.2		
6'	0.8 (3H, t, 7.1)	13	5'	5', 4'

Table 3.1. Filipin II correlation table

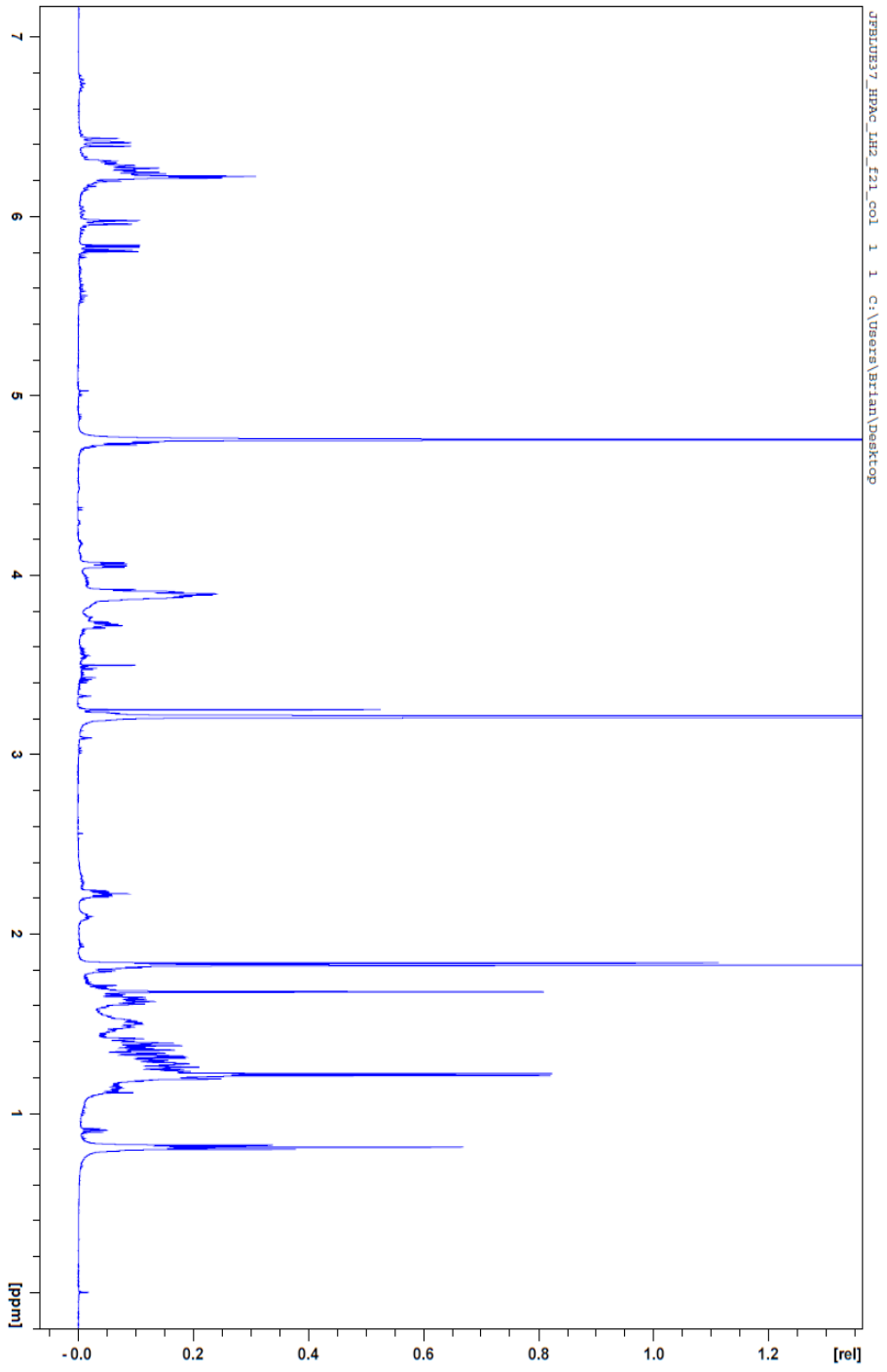

Figure 3.11. TPU-0043 ^{1}H NMR

Pos	Proton	Carbon	COSY	HMBC
1	N/A	174		2, 3, 27
2	2.35 (m)	52.9	3, 1'	1, 1'
3	3.85 (m)	72	2, 4	1, 5, 1'
4	1.43 (m)	41.1	5	
5	4.04 (m)	71.8		
6	1.34-1.52 (m, 2H)	41-43.5		
7	4.04 (1H, m)	71.8		
8	1.34-1.52 (m, 2H)	41-43.5		
9	4.04 (1H, m)	71.8		
10	1.34-1.52 (m, 2H)	41-43.5		
11	4.04 (1H, m)	69.5		
12	1.75, 1.49 (2H, m)	43.6		
13	3.35 (1H, m)	66.1	12, 14	
14	1.76, 1.93 (2H, m)	41.2	13, 15	
15	4.19 (1H, dd, 4.3, 10.1)	74.2	14	
16	N/A	139.4		18, 29
17	6.10 (1H, d, 11.3)	126.6	18, 29	15, 19, 29
18	6.54 (1H, dd, 11.2, 14.2)	128	19, 17	16, 17, 19
19	6.36 (1H, m)	132.7	18	
20	6.35-6.43 (1H, m)	132.7		
21	6.35-6.43 (1H, m)	132.7		
22	6.35-6.43 (1H, m)	132.7		
23	6.34 (1H, m)	132.7		
24	6.41 (1H, m)	132.3	25, 23	25, 23
25	5.95 (1H, dd, 5.9, 15.1)	132.7	26, 24	26, 24
26	4.04 (m)	72.8		
27	4.86 (1H, m)	73.1	26, 28	1, 25, 26
28	1.33 (m, 3H)	16.9	27	26
29	1.80 (3H, s)	10.1	17	13, 15, 16, 17
1'	1.60, 1.72 (m)	28.8		
2'	1.35 (2H, m)	31.2		
3'	1.39 (2H, m)	22.2		
4'	0.8 (3H,m)	13	3'	3', 2', 1'

Table 3.2. TPU-0043 correlation table

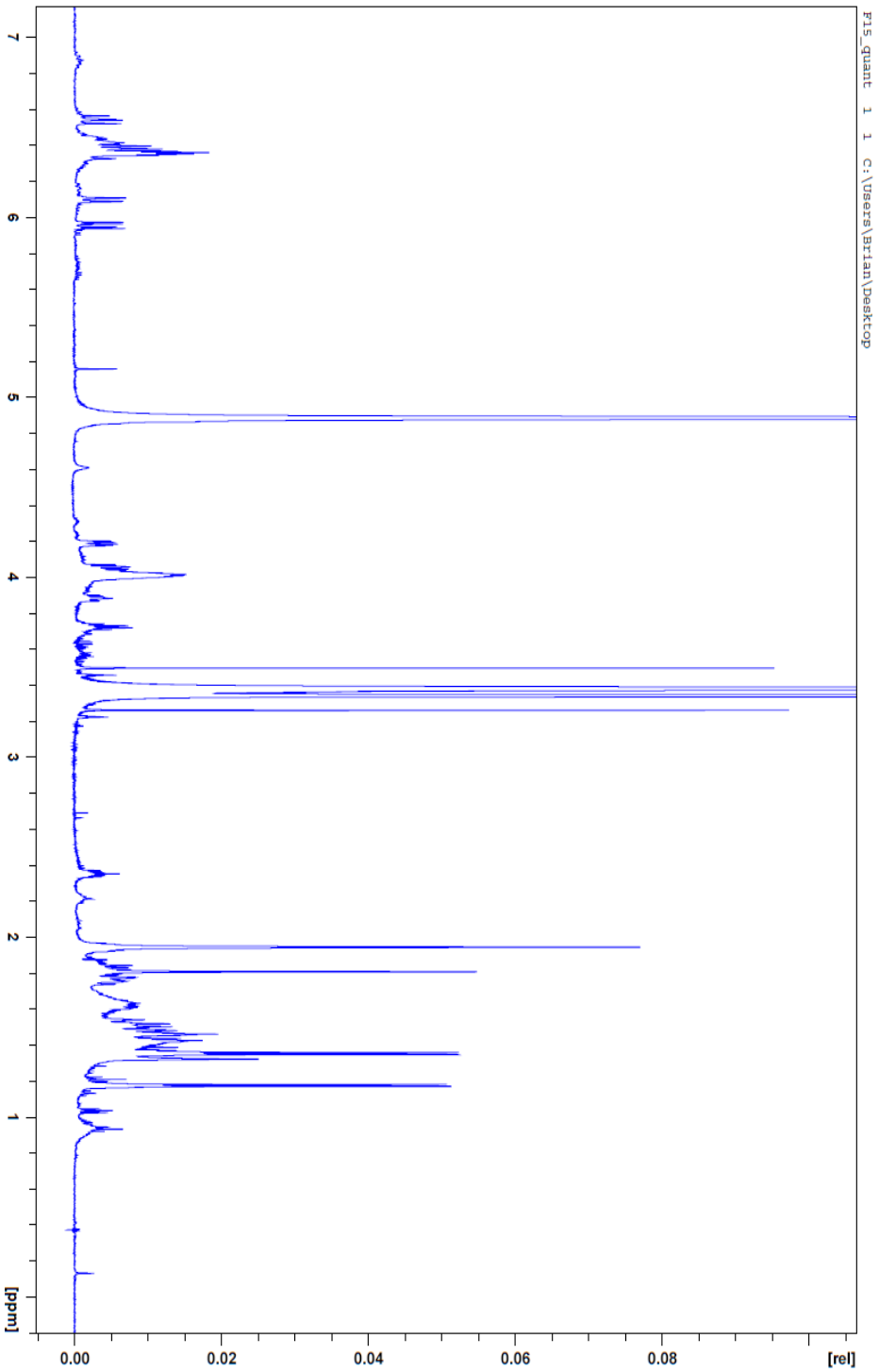

Figure 3.12. Filipin XV ^{1}NMR

Pos.	Proton	Carbon	COSY	HMBC
1	N/A	173.7		27
2	2.35 (m)	52.9	3, 1'	1,
3	3.85 (m)	72	2, 4	
4	1.43 (m)	41.1	3, 5	
5	4.04 (m)	71.8		
6	1.34-1.52 (m, 2H)	41-43.5		
7	4.04 (1H, m)	71.8		
8	1.34-1.52 (m, 2H)	41-43.5		
9	4.04 (1H, m)	71.8		
10	1.34-1.52 (m, 2H)	41-43.5		
11	4.04 (1H, m)	69.5		
12	1.73, 1.49 (2H, m)	43.6		
13	3.35 (1H, m)	66.1	12, 14	
14	1.77, 1.93 (2H, m)	41.2	13, 15	
15	4.19 (1H, dd, 4.3, 10.1)	74.2	14	
16	N/A	139.4		16
17	6.10 (1H, d, 11.3)	126.6	18	15, 19, 29
18	6.54 (1H, dd, 11.2, 14.2)	128	17, 19	19
19	6.36 (1H, m)	132.7		
20	6.35-6.43 (1H, m)	132.7		
21	6.35-6.43 (1H, m)	132.7		
22	6.35-6.43 (1H, m)	132.7		
23	6.34 (1H, m)	132.7		
24	6.41 (1H, m)	132.3	23, 25	23, 25
25	5.95 (1H, dd, 5.9, 15.1)	132.7	24, 26	24, 26
26	4.04 (m)	72.8		
27	4.86 (1H, m)	73.1	26, 28	1, 25, 26
28	1.33 (m, 3H)	16.9	27	27, 26
29	1.80 (3H, s)	10.1	17	15, 16, 17
1'	1.62 (m)	30.3		
2'	1.42 (2H, m)	36.2		
3'	3.71 (1H, m)	66.8	4', 2'	
4'	1.16 (3H,m)	22.1	3'	3', 2'

Table 3.3. Filipin XV correlation able

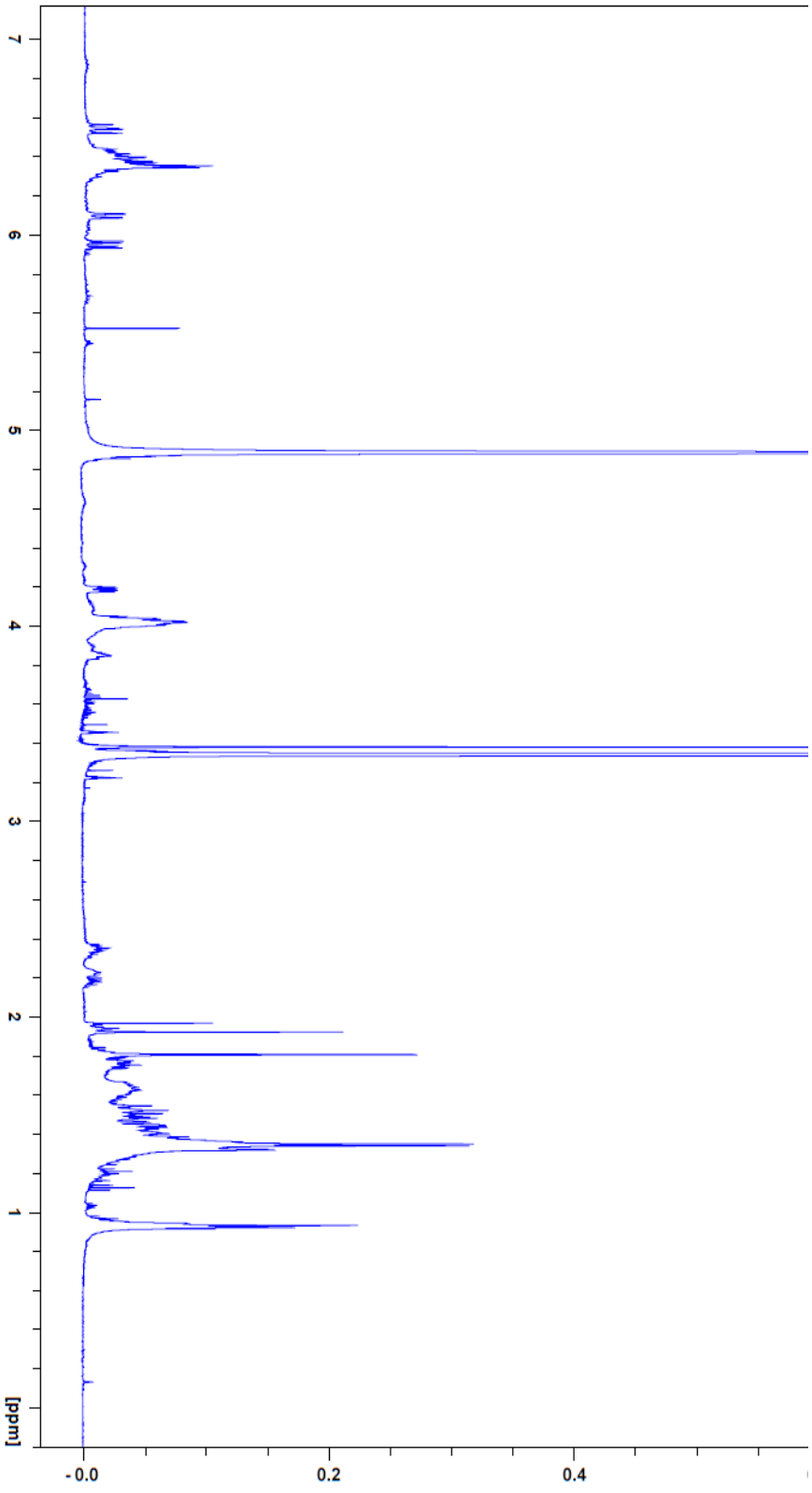

Figure 3.13. Filipin IX ^{1}H MR

Pos.	Proton	Carbon	COSY	HMBC
1	N/A	174		27
2	2.35 (m)	52.9	3, 1'	
3	3.85 (m)	72	2, 4	1, 5
4	1.43 (m)	41.1	5	
5	4.04 (m)	71.8		
6	1.34-1.52 (m, 2H)	41-43.5		
7	4.04 (1H, m)	71.8		
8	1.34-1.52 (m, 2H)	41-43.5		
9	4.04 (1H, m)	71.8		
10	1.34-1.52 (m, 2H)	41-43.5		
11	4.04 (1H, m)	69.5		
12	1.75, 1.49 (2H, m)	43.6		
13	3.35 (1H, m)	66.1	14, 12	
14	1.76, 1.93 (2H, m)	41.2	13, 15	
15	4.19 (1H, dd, 4.3, 10.1)	74.2	14	
16	N/A	139.4		29
17	6.10 (1H, d, 11.3)	126.6	29, 18	29, 15, 19
18	6.54 (1H, dd, 11.2, 14.2)	128	19, 17	19
19	6.36 (1H, m)	132.7	18	
20	6.35-6.43 (1H, m)	132.7		
21	6.35-6.43 (1H, m)	132.7		
22	6.35-6.43 (1H, m)	132.7		
23	6.34 (1H, m)	132.7		
24	6.41 (1H, m)	132.3	25, 23	25, 23
25	5.95 (1H, dd, 5.8, 15.1)	132.7	26, 24	26, 24
26	4.04 (m)	72.8		
27	4.86 (1H, m)	73.1	28, 26	1, 26, 25
28	1.33 (m, 3H)	16.9	27	
29	1.80 (3H, s)	10.1	17	15, 17, 16
1'	1.61, 1.72 (m)	28.8		
2'	1.35 (2H, m)	29		
3'	1.31 (2H, m)	31.4		
4'	1.39 (2H, m)	22.2		
5'	0.8 (3H,m)	13	4'	4', 3'

Table 3.4. Filipin IX correlation table

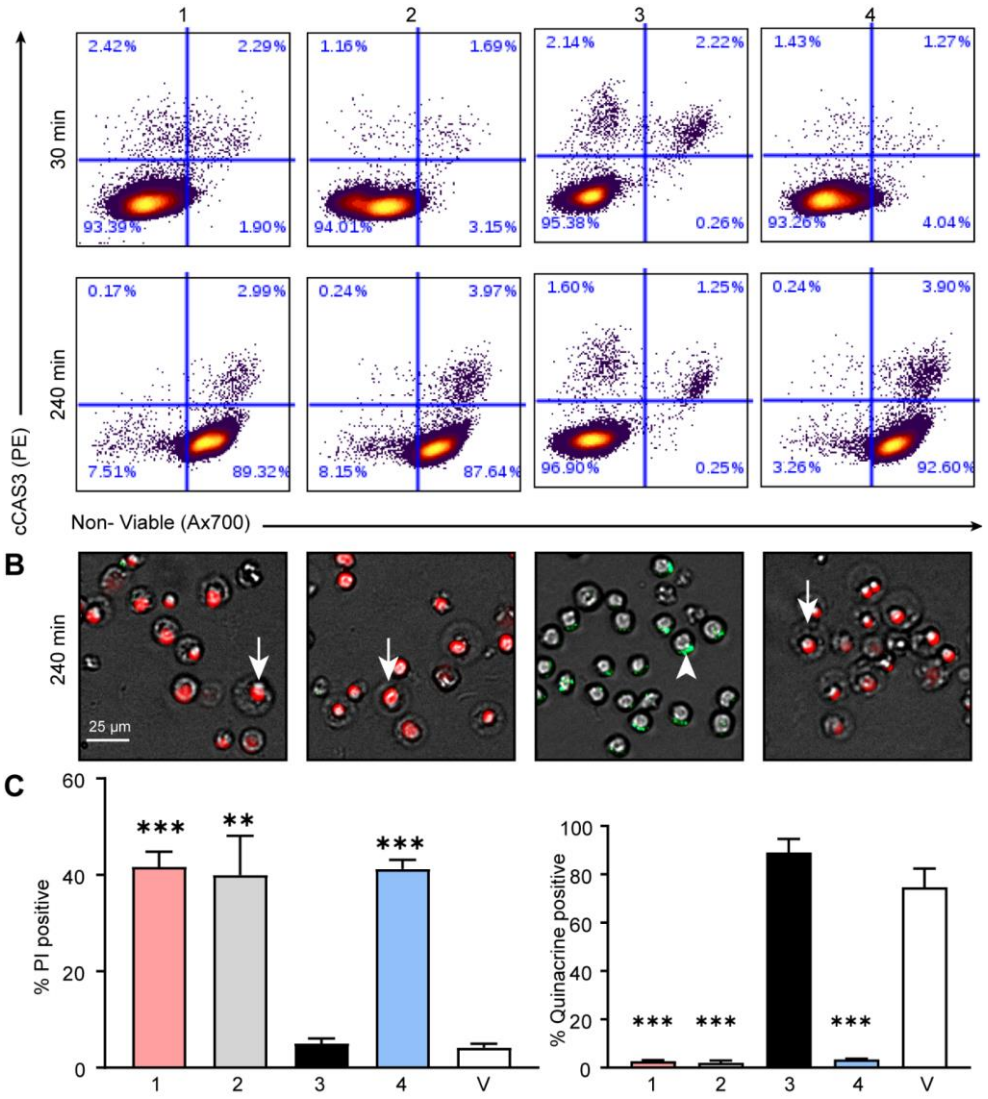

Figure 3.14. Filipin induced death is cCAS3 independent and pendant alkyl chain dependent. (A) Single cell contour plots of apoptotic marker cCAS3 and Ax700 viability stain. Cells were treated for indicated time then stained with Ax700, fixed, permeabilized, and stained for cCAS3. Compounds 1, 2, and 4 disrupted cell membranes without activating cCAS3. **(B)** Cells were challenged with each filipin and stained with a propidium iodide (cell viability, DNA) and quinacrine (intracellular ATP) cocktail. Compounds 1, 2, and 4 exhibit robust PI labeling (white arrows) and concomitant loss of ATP. Compound 3 does not enhance PI infiltration of loss of ATP (white arrowhead). **(C)** Quantification of percent positive PI or quinacrine positive cells versus vehicle control. Cells were challenged with 10 µM of each compound for indicated. Scale bar = 25 µm; Red, PI = DNA; Green, quinacrine = ATP

3.2.6 Isolation and structural elucidation of filipins

K. psammotica culture was scaled up to increase the molecular abundance of the four identified secondary metabolites to afford isolation through HP20 extraction, LH-20 chromatography, and preparative HPLC. Established Fieser-Kuhn rules (*43, 44*) indicated that

candidate *m/z* 639.4 likely contained five conjugated olefins. Further 1D NMR studies also indicated that this metabolite contained a polyol functionality. Based upon these parameters, literature searches identified the candidate compound as the known polyene macrolide metabolite filipin II (**1**), which was confirmed by subsequent 2D NMR studies including correlated spectroscopy (COSY), heteronuclear multiple-bond correlated spectroscopy (HMBC), and heteronuclear single quantum coherence spectroscopy (HSQC) (Figure 3.9A, Figure 3.10, and Table 3.1). The decreased mass of candidate *m/z* 611.4 indicated this metabolite lacked two methylene functional groups in comparison to the assigned structure of compound **1** (Figure 3.9A). 2D NMR analysis (COSY, HMBC, HSQC) of this metabolite demonstrated the core filipin structure was intact, and that the pendant alkyl chain lacked two methylenes (Figure 3.11 and Table 3.2). These assignments confirmed the second polyene macrolide metabolite isolated as a previously described member of the filipin family, chainin (**2**) also known as TPU-0043 (Figure 3.9A) (*45*, *46*). Following the identification of these previously described members of the filipin

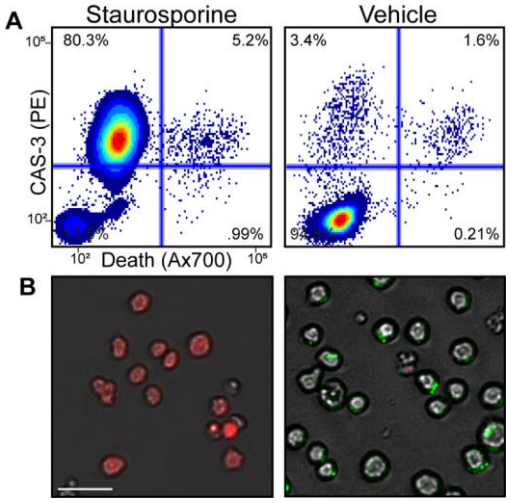

Figure 3.15. Flow cytometry and fluorescent microscopy controls (A) Contour plot of staurosporeine or vehicle challenged cells. Staurosporine challenged cells are cCAS3 positive Vheicle challenged cell are negative for cCAS3 and Ax700. (B) Fluorescent micrographs of staurosporine (left) and vehicle (right) challenged cells. Staurosporince treated cell are penetrated by PI and are negative for ATP detection agent quinacrine. Vehicle challenged cells are PI negative and positive for quinacrine.

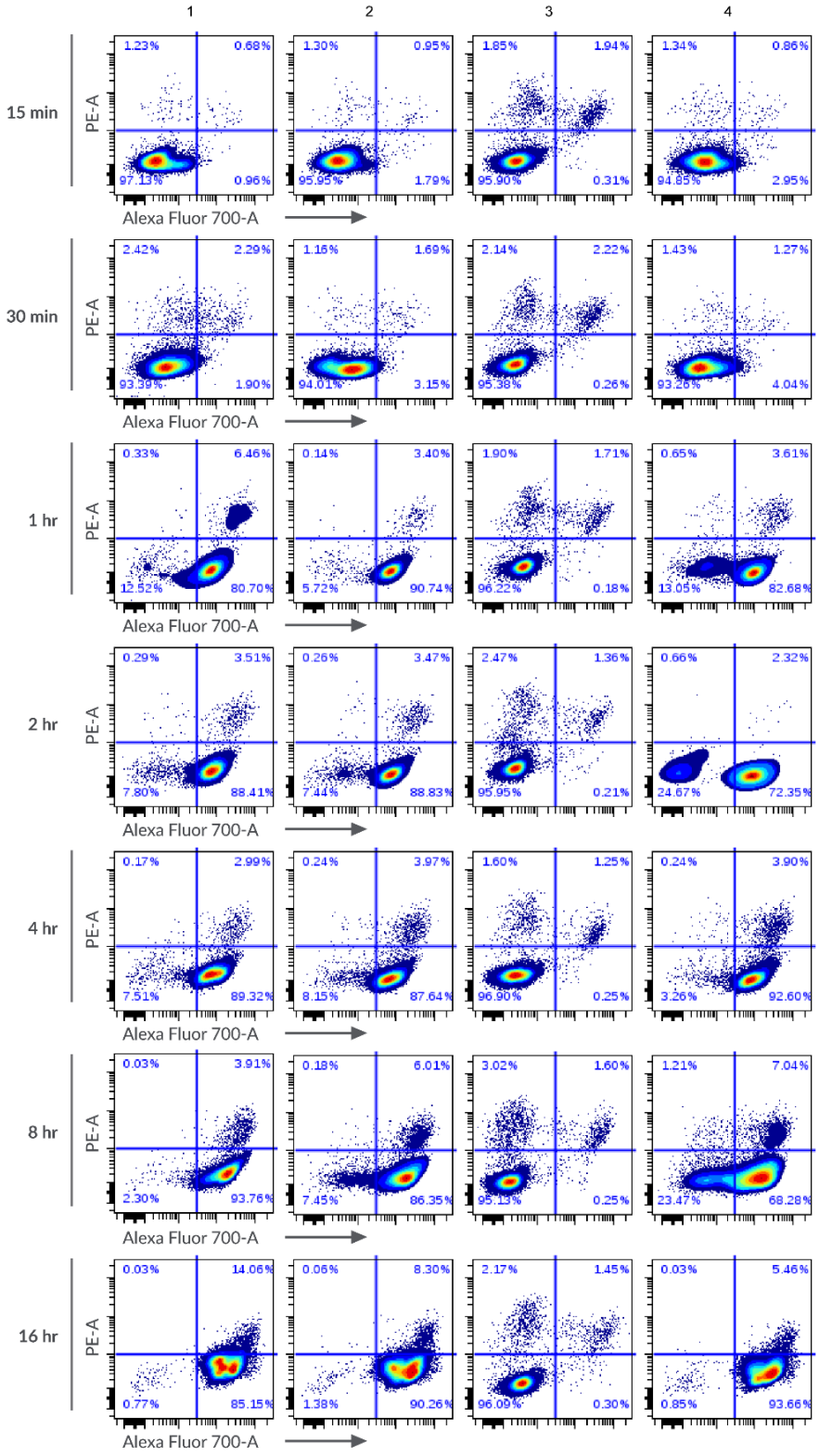

Figure 3.16. Response time course to filipin challenge in MV-4-11 cell line. Compounds 1, 2, and 4 induce cCAS3 independent death as early as 1 hour. Compound 3 is non-toxic.

family, two lower-abundance metabolites with *m/z* of 627.4 and 625.4 respectively were identified. The *m/z* of the more polar of these metabolites (627.4) indicated the addition of a hydroxyl functionality relative to compound **2**. 2D NMR analysis (COSY, HMBC, HSQC) of this metabolite demonstrated that the core filipin structure was intact and indicated an unusual hydroxylation demonstrated that the core filipin structure was intact and indicated an unusual hydroxylation pattern at carbon 3' (Figure 3.12 and Table 3.3). This assignment, combined with high-resolution mass spectrometry analysis validated the mass of this metabolite (Theoretical: 649.3564 (M + Na), Observed: 649.3582 (M + Na)), and confirmed its identity as a new member of the filipin family herein referred to as filipin XV (Figure 3.12). The final metabolite isolated possessed one additional methylene group relative to compound **2**, based upon its *m/z* of 625.4. 2D NMR analysis (COSY, HMBC, HSQC) of this metabolite demonstrated that the core filipin structure was intact, and that the additional methylene functionality was located on the pendant alkyl chain (Figure 3.13, and Table 3.4). The validation of the mass of this metabolite (Theoretical: 647.3771 (M + Na), Observed: 647.3770 (M + Na)) confirmed the identity of this metabolite as filipin IX (Figure 3.13). Historically, filipins have found minimal therapeutic use as they bind unesterified sterols plasma membranes to promote cell lysis. Despite this, filipins have provided a useful diagnostic agent for detecting disrupted cholesterol (*47*) trafficking that occurs in the lysosomal storage disorder Niemann-Pick disease type C, with microscopy due to their intrinsic fluorescent properties (*47-49*). Thus, the excitation/emission spectra of equimolar concentrations of each filipin were assessed to compare relative fluorescent intensities. (Figure 3.9B). This revealed compound **3** as the most excitable compound followed by **2**, **4**, and **1**. Complementary to the excitation spectra **3** also displayed the brightest emission profile followed by **2**, **4**, and **1**. Despite differences in fluorescent intensity, all compounds exhibited bimodal excitation maxima of 340

nm and 357 nm complemented by emission maxima of 451 nm and 491 nm for a stokes shift of 111 nM and 134 nM respectively (9).

3.2.7 Filipin induced cell permeation is caspase-3 independent

Since staurosporine induced apoptosis leads to non-viable cell exclusion in this system, it was possible that filipins engaged apoptosis to account for overall cell loss by non-viable exclusion prior to 16-hour time point signal measurement. This was tested by challenging cells with 10 µM of each filipin compound, staurosporine, or vehicle control and sampling cell populations across time points to measure cCAS3 induction and permeation by flow cytometry.

At each timepoint, cells were stained with Ax700 to detect non-viable cells prior to fixing, then permeabilized with methanol and stained with fluorescent cCAS3 antibody to measure apoptosis. By 60 minutes, 80 % or more of cells treated with **1**, **2**, and **4** exhibited cell population shifts towards the Ax700 positive, non-viable phenotype independent of cCAS3 activation (Figure 3.14 and Figure 3.15). This phenomenon was observed at all timepoints measured after 60 minutes (Figure 3.16). Compound **3**; however, failed to induce cCAS3 or non-viable marker shifts at any timepoint which indicated hydroxylation of the 3' carbon on a four-carbon pendant alkyl chain prevents filipin induced cell permeation (Figure 3.14A). These observations were confirmed with a dimetric fluorescent microscopy assay that utilized propidium iodide (PI), a red fluorescent DNA intercalator that only penetrates cells with compromised cell membranes, and quinacrine, a green fluorescent intracellular ATP detection agent that is lost following membrane permeation (*50, 51*). MV-4-11 cells treated with 10 µM of **3** presented robust quinacrine staining and few PI positive cells comparable to vehicle control (Figure 3.14B). Alternatively, 10 µM of **4**, **2**, and **1** all permeabilized cell membranes as confirmed by PI positive staining and subsequent loss of quinacrine staining, potentially by ATP leakage through membrane pores (Figure 3.14A-C).

Staurosporine control was positive for cCAS3 induction, PI infiltration, and quinacrine signal loss while vehicle control remained cCAS3 and PI negative and quinacrine signal positive. (Figure 3.15A-B). In combination, flow cytometry and fluorescent microscopy confirmed diminished cell populations observed in MAM are consistent with the bioactivity of **4** and **1**. The observed cytotoxicity of **2** was unexpected and most likely failed to deplete viable cells in MAM because of insufficient well concentrations Moreover, all compounds share identical polyene, macrolide chemical scaffolds with varied alkane pendant lengths. Only compound **3**, which carries a hydroxyl group on C 3', was found to be non-cytotoxic.

3.3 Discussion

The MAP and MAM assays owe their versatility and productivity to the efficiencies of FCB. This strategy enabled multiplexing of 48 unique conditions to simultaneously detect six biometric readouts (Death, cCasp3, γ-H2AX, p-S6, p-Hh3, and DNA content), the equivalent of performing 336 individual experiments, with flow cytometry. FCB also afforded a robust staining protocol that saved on fluorescent antibodies, ensures consistent staining among samples, and reduced instrument time (*8*). Moreover, MAM integrates multidimensional chromatographic, mass spectrometric and UV data to yield well-defined metabolomic fractions for independent evaluation of bioeffector potential. This quickly informs decisions to isolate candidate bioactive natural products from complex extracts.

This study demonstrated the metabolomic potential *A. colorodensis* and of *K. psammotica ssp. carrieae* to synthesize siderochelin and a diverse family of filipin molecules, respectively. MAP rapidly identified bioactive and cytotoxic extracts in MV-4-11 AML cell line. The active extracts were then fractionated in MAM to identify secondary metabolites responsible for observed mammalian cell phenotypes. The active extracts were then fractionated in MAM to identify

secondary metabolites responsible for observed mammalian cell phenotypes and ultimately informed the decision to isolate the bioactive components.

The first of the siderochelin family of compounds was isolated from *Nocardia* and described as a ferrous ion chelating agent with weak antibiotic activity (*30*). Additional analogs with similar metal chelating properties have been isolated; however, reported antibiotic properties are consistently weak (*31, 52*). To our knowledge, this is the first report of any siderochelin analog imposing diverse phenotypic changes in mammalian cancer cell models, let alone at the post-translational modification level. Future work will consider testing siderochelin in AML models.

While the MAM workflow detects cCAS3(*8*) it did not detect fluorescent labeling of cCAS3 in wells containing any filipin analogs and confirmed cCAS3 independent death with a flow cytometry time course and overt cytotoxicity with fluorescence microscopy. This works suggests that binding of **1**, **2**, and **4** to cholesterol in cell membranes permeabilized cells thus allowing the viability dye Ax700 entry yielding diminished cell populations in wells with the bioactive components of sufficient concentrations (*47, 49*). The workflow enabled by MAP and MAM with automated data analysis with DebarcodeR affords a generalizable platform for discovery of bioactive secondary metabolites in cancer. The filipins discovered in this case study demonstrate that membrane targeting drugs such as filipins and other polyene antifungals may not target intracellular processes prior to reaching a critical concentration and depolarizing cells, and do not perturb canonical markers of cell injury and regulated cell death.

3.4 Materials & Methods

Isolation of *K. psammotica ssp. carrieae* from Cave Sediments

Soil samples were collected from ten locations throughout the Blue Spring cave system located in White County, Tennessee, using sterile Falcon tubes and a sterile spatula. A 100 mg portion of the

sediment sample was vortexed with 1 mL of sterile water, and the supernatant was serially diluted and plated on agar selective for actinobacteria. Agar plates were incubated at 30 °C for 1-3 weeks and screened for the presence of single actinobacteria colonies. *Kitasatospora psammotica ssp. carrieae* was obtained from loose, oligotrophic, rocky soil taken far from the cave entrance as one of 41 actinomycete isolates derived from cave sediments.

Taxonomy of Producing Organisms

The 16S rRNA sequence was amplified with 27F (AGA GTT TGA TCC TGG CTC AG) and 1525R (AAG GAG GTG ATC CAG CCG CA) universal primers, the resulting amplicon isolated (Qiagen QIAquick® Gel Extraction kit) and sequenced using the described primers. The resulting sequence was analyzed using the EZBioCloud database and NCBI database.

Scanning electron microscopy

A. colordensis and *K. psammotica ssp. carrieae* was plated on ISP-2 agar, overlaid with nylon membrane, and incubated at 30 °C for 3 weeks. Samples were air dried, coated with gold palladium using a Cressington 108 sputter coater and imaged on a FEI Quanta 250 SEM at 5 kV.

Isolation of siderochelin

A. coloradensis subsp. *ossimia* was plated on ISP-2 agar yeast extract 4 g/L, malt extract 10 g/L, glucose 4 g/L, and agar 20 g/L, pH 7.2) from glycerol stocks, and incubated at 30 oC for 5-7 days. Cells were then harvested from solid culture, homogenized, and used to inoculate seed cultures (25 mL ISP-2 liquid media (yeast extract 4 g/L, malt extract 10 g/L, glucose 4 g/L, pH 7.2) in 250 mL Erlenmeyer flasks. Seed cultures were incubated at 30°C for 48 hrs, cells were then harvested from liquid cultures, homogenized, and used to inoculate 500 mL Rich Media (Supplemental Table 1). After 7-day incubation, 100 mL of activated Diaion® HP-20 resin (Supelco)/H2O slurry was added to each 500 mL flask and flasks were incubated with shaking for 3 hrs. Cells/resin were then

centrifuged (3700 × g, 30 min), the supernatant discarded, and the resin/cellular mass extracted with 200 mL methanol/100 mL Diaion® HP-20 resin (Supelco) used (incubation with shaking for 1 hr). Cell mass/resin was centrifuged (3700 × g, 30 min), methanol extract removed, concentrated and stored, and the resin/cellular mass extracted with 200 mL acetone/100 mL HP-20 resin used (incubation with shaking for 1 hr). The cell mass/resin was again centrifuged (3700 × g, 30 min), and the acetone extract was removed, concentrated and stored. Crude acetone extract was fractionated with Sephadex LH-20 resin (GE Healthcare Bio-Sciences) with methanol as the eluent. Fractions were analyzed by analytical HPLC/MS, and fractions containing the compound(s) of interest were pooled and further purified by preparative HPLC (Waters, XBridge C18 Prep, 5 μM) (10 mL/min: linear gradient of 100% Solution A to 100% Solution B. Solution A = 95:5, H2O:MeCN, 10 mM NH4OAc; Solution B: 5:95 H2O:MeCN, 10 mM NH4OAc). Siderochelin was dereplicated using a combination of mass spectrometry and nuclear magnetic resonance spectroscopy data.

Isolation of filipins

Kitasatospora psammotica ssp. carrieae was plated onto ISP-2 agar (yeast extract 4 g/L, malt extract 10 g/L, glucose 4 g/L, and agar 20 g/L, pH 7.2) from glycerol stocks, and incubated at 30 ^{o}C for 5-7 days. Cells were then harvested from solid culture, homogenized, and used to inoculate seed cultures (25 mL ISP-2 liquid media (yeast extract 4 g/L, malt extract 10 g/L, glucose 4 g/L, pH 7.2) in 250 mL Erlenmeyer flasks). Seed cultures were incubated at 30 ^{o}C for 48 hrs, and cells were then harvested from liquid cultures, homogenized, and used to inoculate 500 mL ISP-2 media, ISP-2 + 1.5 mM $LaCl_3$, or ISP-2 + 120 nM rifampin in 2 L fermentation flasks. 500 mL cultures were incubated at 30 ^{o}C for 7 days. $LaCl_3$ and rifampin were added to respective cultures after overnight incubation in 2L fermentation flasks. After 7-day incubation, 100 mL of activated

Diaion® HP-20 resin (Supelco)/H_2O slurry was added to each 500 mL flask, and flasks were incubated with shaking for 3 hrs. Cells/resin were then centrifuged (3700 × g, 30 min), the supernatant discarded, and the resin/cellular mass extracted with 200 mL methanol/100 mL Diaion® HP-20 resin (Supelco) used (incubation with shaking for 1 hr). Cell mass/resin was centrifuged (3700 × g, 30 min), methanol extract removed, concentrated and stored, and the resin/cellular mass extracted with 200 mL acetone/100 mL HP-20 resin used (incubation with shaking for 1 hr). The cell mass/resin was again centrifuged (3700 × g, 30 min), and the acetone extract was removed, concentrated and stored. Crude acetone extract was fractionated with Sephadex LH-20 resin (GE Healthcare Bio-Sciences) with methanol as the eluent. Fractions were analyzed by analytical HPLC/MS, and fractions containing the compound(s) of interest were pooled and further purified by preparative HPLC (Waters, XBridge C18 Prep, 5 μM) (10 mL/min, 0–1 min: 100% solution A, 5 min: 85% solution A; 15% solution B, 65 min: 15% solution A; 85% solution B, and 70 min: 100% solution B) (Solution A = 95:5, H_2O:MeCN, 10 mM NH_4OAc; Solution B: 5:95 H_2O:MeCN, 10 mM NH_4OAc). In order to obtain analytical purity, fractions containing the compounds of were pooled and purified by flash column chromatography (95:5 CH_2Cl_2:MeOH to 80:20 CH_2Cl_2:MeOH). The structure of the filipins was elucidated using a combination of mass spectrometry and nuclear magnetic resonance spectroscopy data. Nuclear magnetic spectroscopy (COSY) allowed for the assignment of the spin systems present, multiplicity-edited heteronuclear single-quantum coherence spectroscopy allowed for assigned 1H shifts to be correlated to their corresponding 13C shifts. Full structure elucidation was completed with heteronuclear multiple-bond correlation spectroscopy.

Metabolomic array generation

Metabolomic array of crude of *K. psammotica ssp. carrieae* extract was prepared as described previously. Briefly, arrays were generated using a split flow 3:1 ratio with 3 parts to photodiode array detector and fraction collector: 1 part to TSQ Triple Quantum mass spectrometer. Fraction plates were prepared by injecting 20 µL of crude *K. psammotica ssp. carriae* extract (1:1 methanol:water) via Thermo PAL auto injector onto a Phenomenex Luna 5 µm C18(2) reverse-phase C_{18} HPLC column. The sample was fractionated using a gradient of 100% Buffer A (95% H_2O, 5% acetonitrile) to 100% Buffer B (5% acetonitrile, 95% H_2O) over 30 min at a flow rate of 1 mL/min and split in a 3:1 ratio with three parts going to the photodiode array detector and fraction collector and one part going to the MS reverse-phase HPLC column at a flow rate of 1 mL/min. Fractions were collected in 1-min intervals in a 96 deep well plate. A volume of 150 uL of eluent from each well was transferred to 96 well plates and dried in vacuo using a Genevac HT-6 system according to factory standard HPLC method.

Cell Seeding and chemical challenge

Metabolomic array was seeded with 200,000 MV-4-11 cells/well and incubated overnight. Control wells were treated with 0.5% DMSO (3 wells) or natural product control staurosporine, etoposide, aphidicolin, rapamycin, or nocodazole in 200 µL. Following treatment of cells with natural product controls, vehicle or metabolomic fractions, 200 µl of cells (1 million cells/mL), were stained with 20 µL of Ax700 (Thermo A20010, stock concentration 20 µg/mL) to a final concentration of 0.04 µg/mL 37 °C for 20 min at and protected from light. Cells were then transferred 96 well V-bottom polypropylene plate with 20 µL of 20 % PFA (Alfa Aesar 47340) for a final PFA concentration of 1.6 % for 10 min. at room temperature, and protected from light. Plate was centrifuged at 800 g for 5 min, supernatant decanted by plate inversion and dabbed dry on a Kimwipe (Kimtech 34155).

The plate was then vortexed, and cells permeabilized with 200 µl ice-cold MeOH for at least twenty minutes at -20 °C. After permeation and prior to FCB, cells were centrifuged at 800 g for 5 min, decanted by inversion, vortexed, and resuspended in 200 µL PBS (Gibco 10010-023).

Fluorescent cell barcoding

Eight 1:1.7 serial dilution stock concentrations of Pacific Blue (Thermo P10163) were prepared in DMSO at concentrations ranging from 10 µg/mL to 0.24 µg/mL. Six 1:1.7 serial dilution stock concentrations of Pacific Orange (Thermo P30253) were prepared in DMSO at concentrations ranging from 40 µg/mL to 2.82 µg/mL. Alexa750 (Thermo A20011) 500 µg/mL stock solution in DMSO was prepared at 5 µg/mL. All three dyes were combined on a single V-bottom polypropylene master plate as follows: 50 µL of Pacific Blue were added to plate rows with the highest concentration in row A and the lowest concentration in row H; 50 µL of Pacific Orange were added to columns with the highest concentration in column 1 and lowest concentration in column 6; 50 µL of Alexa 750 were added to all wells. Primary plates were then aliquoted in 15 µL volumes to 96 well V-bottom propylene plates and stored at –20 °C. An aliquot of 185 µL of fix/permed cells in PBS was added to 15 µL of barcode dyes and stained for 15 minutes at room temperature, protected from light. Barcoding reactions were quenched with 70 µL 2% BSA in PBS, centrifuged at 800 x g for 5 min, decanted by inversion, vortexed, washed with 200 µL 2% BSA in PBS, centrifuged at 800 x g for 5 min, decanted by inversion, and vortexed. Wells in column 1 were then resuspended in 200 µL of 2% BSA in PBS then transferred to column 2 and repeated to column 6. All rows in column 6 were then pooled into 1 flow cytometry tube.

Fluorescent cell staining

Cells were stained with antibodies γH2AX:Percp-Cy5.5 (BD 564718, 2.5:100), cCAS3:PE (10:100), p-HH3:Pe-Cy7 (Biolegend 6410, 1:1000), p-S6:Ax647 (CST. 4:100) for 30 minutes at

4 °C then washed with 2% BSA/PBS and resuspended in 475 uL of 2% BSA/PBS. The DNA intercalator YoPro (Invitrogen) was diluted 1:1000 in 960 uL of 2% BSA/PBS plus 40 uL of RNAse for addition of 25 uL to each stained experiment for a total volume of 500 uL.

Flow cytometry

Flow cytometry data was acquired using a 4 laser BD fortessa. Acquired data was uploaded to Cytobank for compensation and gating. Samples were debarcoded with DebarcodeR to produce one .fcs file per well and uploaded to Cytobank for storage and further analysis.

Fluorescent microscopy

MV411 cells were seeded on Greiner Bio-One black-glass bottom 96 well plates and challenged with each compound overnight. Cells were stained with 10 μM quinacrine for 30 minutes at room temperature in the dark and washed with 2% BSA/PBS. Cells were stained with 300 nM propidium iodide. Images were captured with ImageXpress Micro XL fluorescent microscope.

Statistical analysis and figure generation

Data was input to GraphPad Prism (9.2.0) and analyzed with one-way ANOVA. All data is reported as mean +/- standard deviation (S.D.) of at least 3 biological replicates. GraphPad Prism, Adobe Illustrator 2021, Microsoft Excel 2016 were used for figure generation.

General Experimental Procedures

Mass spectrometry was performed by using a TSQ Triple Quantum mass spectrometer equipped with an electrospray ionization source and Surveyor PDA Plus detector (Thermo Fisher Scientific, Waltham, MA, USA) (ESI, positive and negative mode). High Resolution Electrospray Ionization-Mass Spectrometry (HRESI-MS) was performed using a Waters Synapt G2S HDMS (Milford, MA, USA). NMR spectra were recorded on a 600 MHz Bruker AV-II FT NMR spectrometer with

cryoprobe & LC-SPE (Bruker BioSpin Corp., Billerica, MA, USA). Methanol-d4 (Sigma-Aldrich) and dimethyl sulfoxide-d6 (Sigma-Aldrich) were used as solvents, and the chemical shifts were referenced to the solvent signal of methanol-d4 (3.30 ppm)

3.5 References

1. J. C. Albright *et al.*, Large-Scale Metabolomics Reveals a Complex Response of Aspergillus nidulans to Epigenetic Perturbation. *ACS Chemical Biology* **10**, 1535-1541 (2015).
2. M. T. Henke *et al.*, New Aspercryptins, Lipopeptide Natural Products, Revealed by HDAC Inhibition in Aspergillus nidulans. *ACS Chemical Biology* **11**, 2117-2123 (2016).
3. D. K. Derewacz, B. C. Covington, J. A. Mclean, B. O. Bachmann, Mapping Microbial Response Metabolomes for Induced Natural Product Discovery. *ACS Chemical Biology* **10**, 1998-2006 (2015).
4. B. C. Covington, M. R. Seyedsayamdost, MetEx, a Metabolomics Explorer Application for Natural Product Discovery. *ACS Chemical Biology*, (2021).
5. F. Xu, B. Nazari, K. Moon, L. B. Bushin, M. R. Seyedsayamdost, Discovery of a Cryptic Antifungal Compound from Streptomyces albus J1074 Using High-Throughput Elicitor Screens. *Journal of the American Chemical Society* **139**, 9203-9212 (2017).
6. B. K. Mahmoud *et al.*, Metabolomic profiling and biological investigation of Tabebuia Aurea (Silva Manso) leaves, family Bignoniaceae. *Natural Product Research* **35**, 4632-4637 (2021).
7. J. H. Boyce, B. J. Reisman, B. O. Bachmann, J. A. Porco, Jr., Synthesis and Multiplexed Activity Profiling of Synthetic Acylphloroglucinol Scaffolds. *Angew Chem Int Ed Engl* **60**, 1263-1272 (2021).
8. D. C. Earl *et al.*, Discovery of human cell selective effector molecules using single cell multiplexed activity metabolomics. *Nat Commun* **9**, 39 (2018).
9. P. O. Krutzik, G. P. Nolan, Fluorescent cell barcoding in flow cytometry allows high-throughput drug screening and signaling profiling. *Nature Methods* **3**, 361-368 (2006).
10. P. O. Krutzik, M. R. Clutter, A. Trejo, G. P. Nolan, Fluorescent Cell Barcoding for Multiplex Flow Cytometry. *Current Protocols in Cytometry* **55**, (2011).
11. B. J. Reisman, S. M. Barone, B. O. Bachmann, J. M. Irish, DebarcodeR increases fluorescent cell barcoding capacity and accuracy. *Cytometry Part A*, (2021).
12. M. Otoguro, M. Hayakawa, T. Yamazaki, Y. Iimura, An integrated method for the enrichment and selective isolation of Actinokineospora spp. in soil and plant litter. *Journal of Applied Microbiology* **91**, 118-130 (2001).
13. N. S. Chi, H. C. Ji, B. Keun-Shik, An Improved Selective Isolation of Rare Actinomycetes from Forest Soil.pdf. *The Journal of Microbiology* **39**, 17-23 (2001).
14. K. Kawai, G. Wang, S. Okamoto, K. Ochi, The rare earth, scandium, causes antibiotic overproduction inStreptomycesspp. *FEMS Microbiology Letters* **274**, 311-315 (2007).
15. B. C. Covington, J. M. Spraggins, A. E. Ynigez-Gutierrez, Z. B. Hylton, B. O. Bachmann, Response of Secondary Metabolism of Hypogean Actinobacterial Genera to Chemical and Biological Stimuli. *Appl Environ Microbiol* **84**, (2018).
16. A. D. Steele, C. N. Teijaro, D. Yang, B. Shen, Leveraging a large microbial strain collection for natural product discovery. *Journal of Biological Chemistry* **294**, 16567-16576 (2019).
17. K. E. Diggins, P. B. Ferrell, Jr., J. M. Irish, Methods for discovery and characterization of cell subsets in high dimensional mass cytometry data. *Methods* **82**, 55-63 (2015).

18. D. K. Derewacz, B. C. Covington, J. A. McLean, B. O. Bachmann, Mapping Microbial Response Metabolomes for Induced Natural Product Discovery. *ACS Chem Biol* **10**, 1998-2006 (2015).
19. R. Subramani, W. Aalbersberg, Culturable rare Actinomycetes: diversity, isolation and marine natural product discovery. *Appl Microbiol Biotechnol* **97**, 9291-9321 (2013).
20. H. K. Kumar *et al.*, Genomic characterization of eight Ensifer strains isolated from pristine caves and a whole genome phylogeny of Ensifer (Sinorhizobium). *J Genomics* **5**, 12-15 (2017).
21. P. Rangseekaew, W. Pathom-Aree, Cave Actinobacteria as Producers of Bioactive Metabolites. *Front Microbiol* **10**, 387 (2019).
22. B. C. Covington, J. A. McLean, B. O. Bachmann, Comparative mass spectrometry-based metabolomics strategies for the investigation of microbial secondary metabolites. *Nat Prod Rep* **34**, 6-24 (2017).
23. C. R. Goodwin *et al.*, Structuring Microbial Metabolic Responses to Multiplexed Stimuli via Self-Organizing Metabolomics Maps. *Chem Biol* **22**, 661-670 (2015).
24. D. K. Derewacz, C. R. Goodwin, C. R. McNees, J. A. McLean, B. O. Bachmann, Antimicrobial drug resistance affects broad changes in metabolomic phenotype in addition to secondary metabolism. *Proc Natl Acad Sci U S A* **110**, 2336-2341 (2013).
25. Y. Imai, S. Sato, Y. Tanaka, K. Ochi, T. Hosaka, Lincomycin at Subinhibitory Concentrations Potentiates Secondary Metabolite Production by Streptomyces spp. *Appl Environ Microbiol* **81**, 3869-3879 (2015).
26. C. T. Nguyen, D. Dhakal, V. T. T. Pham, H. T. Nguyen, J. K. Sohng, Recent Advances in Strategies for Activation and Discovery/Characterization of Cryptic Biosynthetic Gene Clusters in Streptomyces. *Microorganisms* **8**, (2020).
27. K. Ochi, T. Hosaka, New strategies for drug discovery: activation of silent or weakly expressed microbial gene clusters. *Appl Microbiol Biotechnol* **97**, 87-98 (2013).
28. B. K. Okada, M. R. Seyedsayamdost, Antibiotic dialogues: induction of silent biosynthetic gene clusters by exogenous small molecules. *FEMS Microbiol Rev* **41**, 19-33 (2017).
29. F. J. Reen, S. Romano, A. D. Dobson, F. O'Gara, The Sound of Silence: Activating Silent Biosynthetic Gene Clusters in Marine Microorganisms. *Mar Drugs* **13**, 4754-4783 (2015).
30. <Liu-1981-Siderochelin-a-new-ferrous-ion-chel.pdf>.
31. C.-H. Lu, F.-W. Ye, Y.-M. Shen, Siderochelins with anti-mycobacterial activity from Amycolatopsis sp. LZ149. *Chinese Journal of Natural Medicines* **13**, 69-72 (2015).
32. D. A. Evans, B. T. Connell, Synthesis of the Antifungal Macrolide Antibiotic (+)-Roxaticin. *Journal of the American Chemical Society* **125**, 10899-10905 (2003).
33. A. Herbrik *et al.*, A Human Lung-Associated Streptomyces sp. TR1341 Produces Various Secondary Metabolites Responsible for Virulence, Cytotoxicity and Modulation of Immune Response. *Front Microbiol* **10**, 3028 (2019).
34. S. Zhou *et al.*, Pentamycin Biosynthesis in Philippine Streptomyces sp. S816: Cytochrome P450-Catalyzed Installation of the C-14 Hydroxyl Group. *ACS Chem Biol* **14**, 1305-1309 (2019).
35. S. Kumar, G. Stecher, K. Tamura, MEGA7: Molecular Evolutionary Genetics Analysis Version 7.0 for Bigger Datasets. *Molecular Biology and Evolution* **33**, 1870-1874 (2016).
36. S.-H. Yoon *et al.*, Introducing EzBioCloud: a taxonomically united database of 16S rRNA gene sequences and whole-genome assemblies. *International Journal of Systematic and Evolutionary Microbiology* **67**, 1613-1617 (2017).

37. D. P. Labeda *et al.*, Phylogenetic relationships in the family Streptomycetaceae using multi-locus sequence analysis. *Antonie van Leeuwenhoek* **110**, 563-583 (2017).
38. A. Oren, G. M. Garrity, List of novel names and novel combinations previously effectively, but not validly, published. *International Journal of Systematic and Evolutionary Microbiology* **67**, 2075-2078 (2017).
39. L. J. Kuo, L.-X. Yang, γ-H2AX – A Novel Biomarker for DNA Double-strand Breaks. *in vivo* **22**, (2008).
40. W. C. Liu *et al.*, Siderochelin, a new ferrous-ion chelating agent produced by Nocardia. *J Antibiot (Tokyo)* **34**, 791-799 (1981).
41. D. Okuyama *et al.*, Isolation, racemization and absolute configuration of siderochelin A. *The Journal of Antibiotics* **35**, 1240-1242 (1982).
42. L. A. Mitscher *et al.*, Isolation and structural determination of siderochelin C, a fermentation product of an unusual Actinomycetes sp. *The Journal of Antibiotics* **37**, 1260-1263 (1984).
43. W. R. Silverstein, G. C. Bassler, Spectrometric Identification of Organic Compounds. *Journal of Chemical Education* **39**, 546-553 (1962).
44. D. M. F. Edwards, Direct liquid introduction LC-MS of polyene macrolide antibiotics: Comment on the structure of filipin II. *The Journal of Antibiotics* **42**, 322-324 (1989).
45. R. C. Pandey, N. Narasimhachari, K. L. Rinehart, D. S. Millington, Polyene antibiotics. IV. Structure of chainin. *Journal of the American Chemical Society* **94**, 4306-4310 (1972).
46. Y. Igarashi *et al.*, Absolute Configuration of TPU-0043, a Pentaene Macrolide from Streptomyces sp. *The Journal of Antibiotics* **58**, 523-525 (2005).
47. M. E. Bergy, T. E. Eble, Filipin complex. *Biochemistry* **7**, 653-659 (1968).
48. J. Ledvinová, M. Elleder, Filipin test for diagnosis of Niemann-Pick disease type C. *Sb Lek* **94**, 137-143 (1993).
49. R. Bittman, S. A. Fischkoff, Fluorescence Studies of the Binding of the Polyene Antibiotics Filipin III, Amphotericin B, Nystatin, and Lagosin to Cholesterol. *Proceedings of the National Academy of Sciences* **69**, 3795-3799 (1972).
50. A. Q. Sukkurwala *et al.*, Screening of novel immunogenic cell death inducers within the NCI Mechanistic Diversity Set. *OncoImmunology* **3**, e28473 (2014).
51. I. Martins *et al.*, Chemotherapy induces ATP release from tumor cells. *Cell Cycle* **8**, 3723-3728 (2009).

CHAPTER 4 – Single Cell Responses to Anthracycline Family of Compounds

4.1 Introduction

Understanding how the complex coterie of cell types and subtypes comprising heterogenous patient-derived samples respond to bioactive molecules can provide powerful insight into the development of potential of drug candidates. However, patient-level compound characterization does not generally occur until pre-clinical development. There is therefore an additional gap in typical discovery workflows in assessing the potential for isolated compounds in biologically relevant contexts and primary cell preparations. Recent advances in single cell genomics, transcriptomics, and proteomics have enabled rapid detection of cell type and subtype responses to small molecules. In this work we demonstrate how purified active compounds (identified via MAM) can be subsequently evaluated via multiplexed phospho-proteomic assays in biopsied samples from patients diagnosed with acute myeloid leukemia (AML). Using mass cytometry to measure up to 30x simultaneous cell identity and/or status immunomarkers and bioinformatic analysis produces a comprehensive map of cellular responses in patient-derived cellular preparations. Linking these results to genomic information provides future opportunities for development of patient-specific therapies.

Biosynthetically apt microbial sources of natural products can be obtained via discovery of novel taxa, which have a track record of leading to novel chemical diversity or, more recently be found within existing organism collections via genomic (*1*) or within ecosystems via metagenomic (*2-4*) assessment of biosynthetic potential. However, a rate determining step in microbial natural product discovery is ascertaining conditions for the production of active metabolites from an organism of interest. There are many means by which to activate microbial biosynthetic gene clusters, ranging from heterologous expression in chassis organisms, to promoter engineering and

chemical/biological stimuli in native producers. Herein we describe a multiplexed activity profiling system (MAP) that can simultaneously correlate multiple stimuli of natural product biosynthesis against multiple single cell phenotypic markers of mammalian cell function to rapidly determine productive activation conditions.

To unambiguously link initial biological phenotypes of interest in an extract to a discrete metabolite, it is typically necessary to isolate and structurally identify a metabolite of interest prior to investigating the scope of its bioactivity. This remains an additional rate determining step in activity-based workflows. Herein, we further demonstrate how multiplexed activity metabolomics (MAM) can identify known molecular features within active extracts and rapidly prioritize potentially new molecular features for further characterization. MAM accelerates the discovery of both previously unreported secondary metabolites and known compounds with novel biological phenotypes with potential for human medicine. Of note, MAM can be practiced with suspended mammalian cell lines or primary cell preparation to provide insight to pharmacological potential, in many cases, even prior to compound isolation.

Using MAP and MAM this work identified new biological activity of the anthracycline isoquinocycline B synthesized by cave-isolated organism *Micromonospora phyotophila*. isoquinocylcline B was then assayed against two additional anthracyclines in one healthy peripheral blood mononuclear cell sample (PBMC) and three genotypically distinct AML patients to determine anthracycline specificity to induce functional responses in defined cell subsets.

4.2 Results

4.2.1 MAP and MAM identified new activity of isoquinocycline B

M. phytophila extract challenged MV-4-11 cells exhibit robust phenotypic, dose-dependent changes across cell status markers (Figure 4.1A). Most notably, DNA fluorescence shifts increase

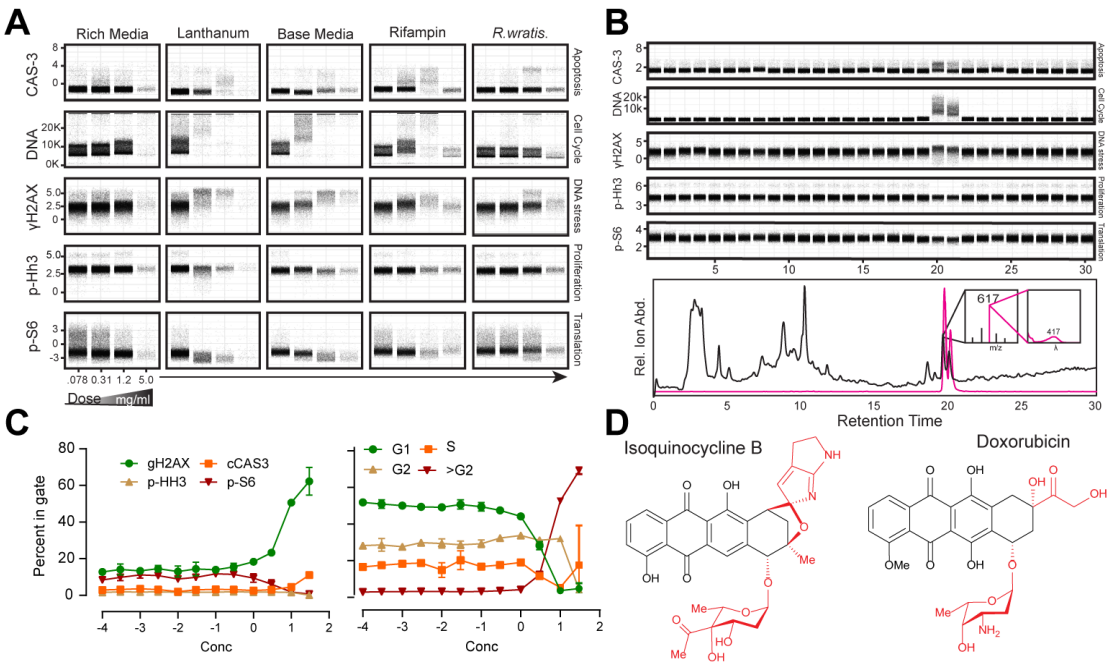

Figure 4.1. Bioeffector led discovery identifies preferred stimuli for biosynthesis and new activity of isoquinocycline B. (A) *M. phytophila* lanthanum stimulated extract demonstrates dose-dependent phenotypic shifts in fluorescently cell barcoded single cell populations. (B) MAM aligns well-time specific phenotypic shifts that aligns to positive extracted ion current 617. (C) Dose responses of bioactiivty markers to 16 hour isoquinocycline B challenge. IsoB is a robust DNA damaging agent that increases cellular DNA content above 2N as shown by percent of cells positive for DNA fluorescent intensity beyond G2 cells. (D) The bioactive agent was dereplicated to isoquinocycline B an anthracycline compound with pyyrole function installed on the D ring.

well beyond typical G2 locked cell fluorescent profiles. The phenomenon was observed in MAM wells 20 and 21, consistent with additional yH2AX, cCasp3, p-Hh3, and p-S6 fluorescent shifts observed in screening (Figure 4.1A). Extracted positive ion currents indicate candidate metabolite of *m/z* 617 with local UV absorbance of maxima of 417nm (Figure 4.1B). *M. phytophila* was scaled in base media since this was the optimal condition for biosynthesis of candidate compound *m/z* 617 (Figure 4.1B). Crude acetone extract of scaled *M. phytophila* cultures were purified by size-exclusion, preparative, and analytical chromatography. The structure of the bioactive component was dereplicated to isoquinocycline B (*5, 6*) by NMR (Figure 4.2 and Figure 4.3) and mass spectrometry. Isoquinocycline B is described as a week antibiotic (*5*) with cytotoxic potential in

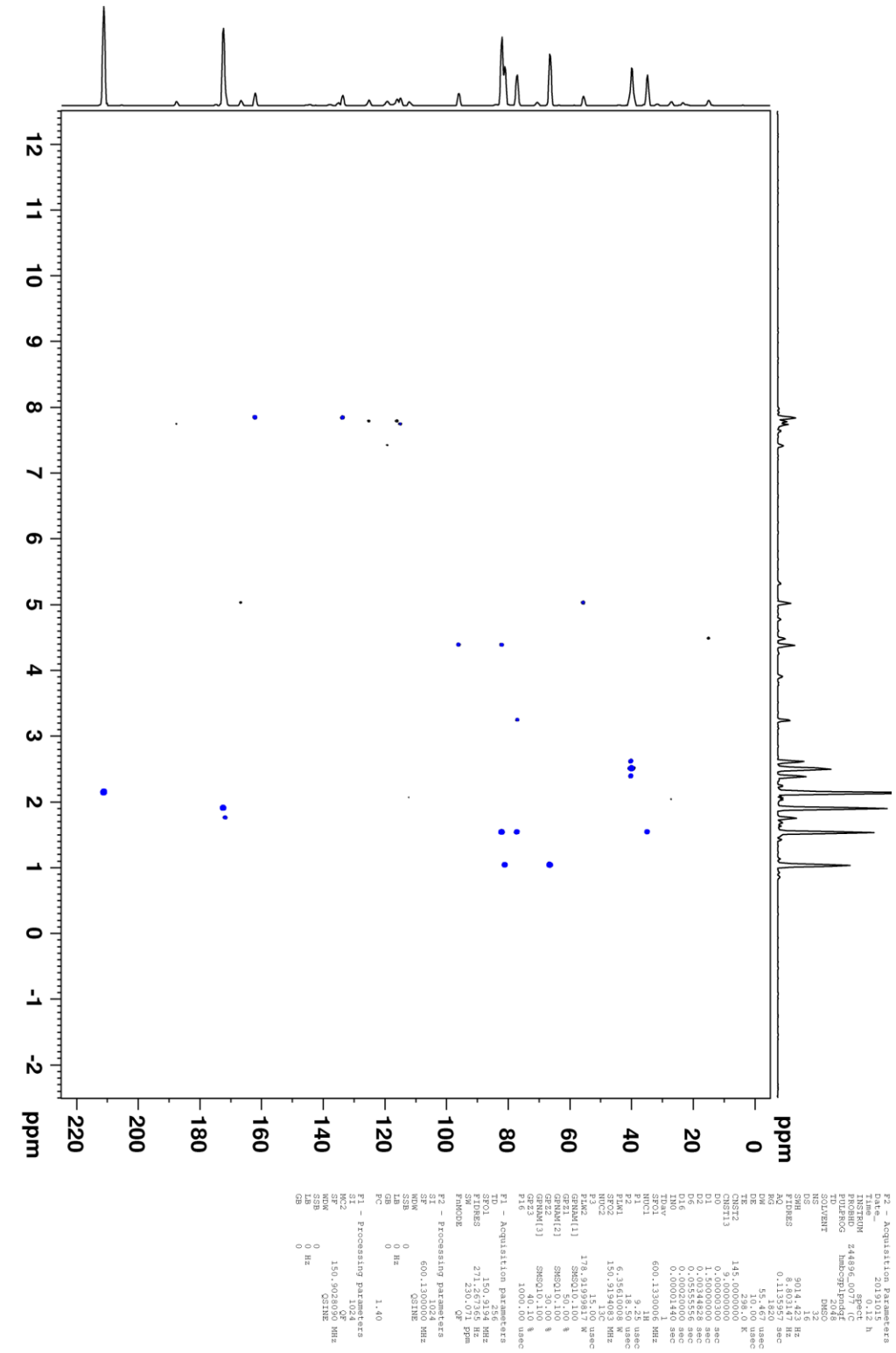

Figure 4.2. 600 MHz HMBC of isoquinocycline B in DMSO.

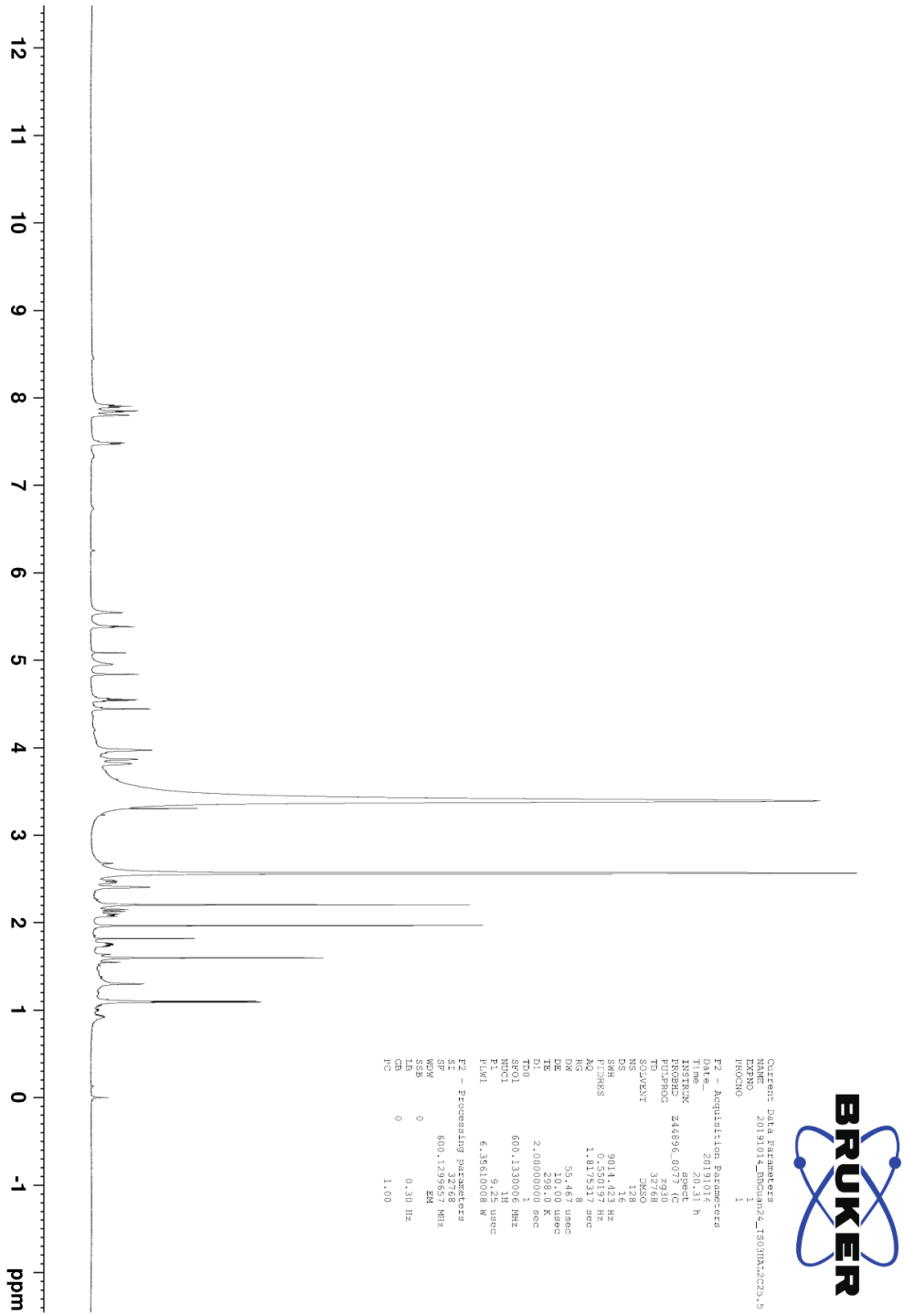

Figure 4.3. 600 MHz ^{1}H spectra of isoquinocycline B in DMSO

mammalian cell lines (*6*). Additionally, the BGC and subsequent biosynthesis are known (*7*); however, deep functional characterization of isoquinocycline B in mammalian systems remained lacking. A dose response of phenotype responses in MV-4-11 to isoquinocycline B challenge revealed and EC_{50} of 5 μM for γH2AX response and 7 μM for > G2 DNA phenotype (Figure 4.1C). Given the utility of the anthracycline compound doxorubicin, also known as the red death for its uncomfortable and detrimental side effects (*8, 9*), in AML, we queried isoquinocycline B alongside doxorubicin (Figure 4.1D) and an additional anthracycline identified by the laboratory, specumycin A1 (Figure 4.4) (*10*), for distinct phenotypic effects in MV-4-11 cell line. All three molecules maintain integrity of the aglycone core (Figure 4.1D and Figure 4.4) supporting DNA intercalation as the major mechanism of action (*11, 12*), however it remained unclear if all three compounds instituted similar phenotypes in MV-4-11 cell line. Thus, we challenged MV-4-11 cells overnight with 10 μM of each compound. Unlike Isoquinocycline B, doxorubicin and specumycin A1 dramatically depressed DNA fluorescent shifts to sub-G1 (<2n) levels (Figure

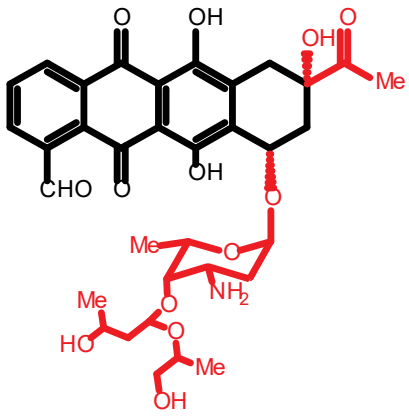

Specumycin A1

Figure 4.4. Structure of specumycin A1. Red bonds and atoms indicate deviations from isoquinocycline B or doxorubicin.

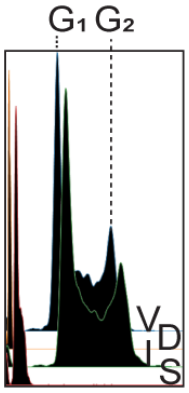

Fold$_{\Delta}$, % in gate	V	D	I	S
<G_1	1	81	1.5	78
G_1	1	0	.85	0
S	1	0	1	0
G_2	1	0	.69	0
>G_2	1	0	4.5	0

Figure 4.5. Cell cycle response to anthracycline challenge measured as fold change of percent cells in gate verse vehicle control. Doxorubicin and specumycin A1 suppressed DNA content to <G1 compared to vehicle control. Isoquinocycline increased cells with >G2 DNA content V = Vehicle, D = Doxorubicin, I = Isoquinocycline B, S = Specumycin A1

4.5). To our knowledge, this is the first instance of distinctly opposite single cell phenotypes induced by anthracycline family of compounds (Figure 4.4C and Figure 4.5).

4.2.2 Anthracyclines induce different functional profiles in healthy peripheral blood mononuclear cells

Healthy PBMC cell identity was measured with 22 surface markers and then were dimensionally reduced with UMAP. Cell types were gated by dominant CD surface marker antigen to assess population changes and functional responses (Figure 4.6A) Antigen presenting cells distinguished by CD11 exhibited DNA damage in response to doxorubicin and specumycin A1 (Figure 4.6B). Specumycin A1 also diminished transcription initiation factor p-NFκB which could impact transcriptional programs to redirect cell type or function (Figure 4.6B). Loss of p-NFκB was also prevalent in CD14+ monocytes treated with specumycin A1 (Figure 4.6B). Monocytes and other APCs, excluding B cells, are derived from myeloid precursor cells and follow distinct transcriptional and translational programs that distinguish cellular identity. Alternatively, lymphoid lineage cells including CD16+ NK cells, B cells, and T cells did not exhibit reductions

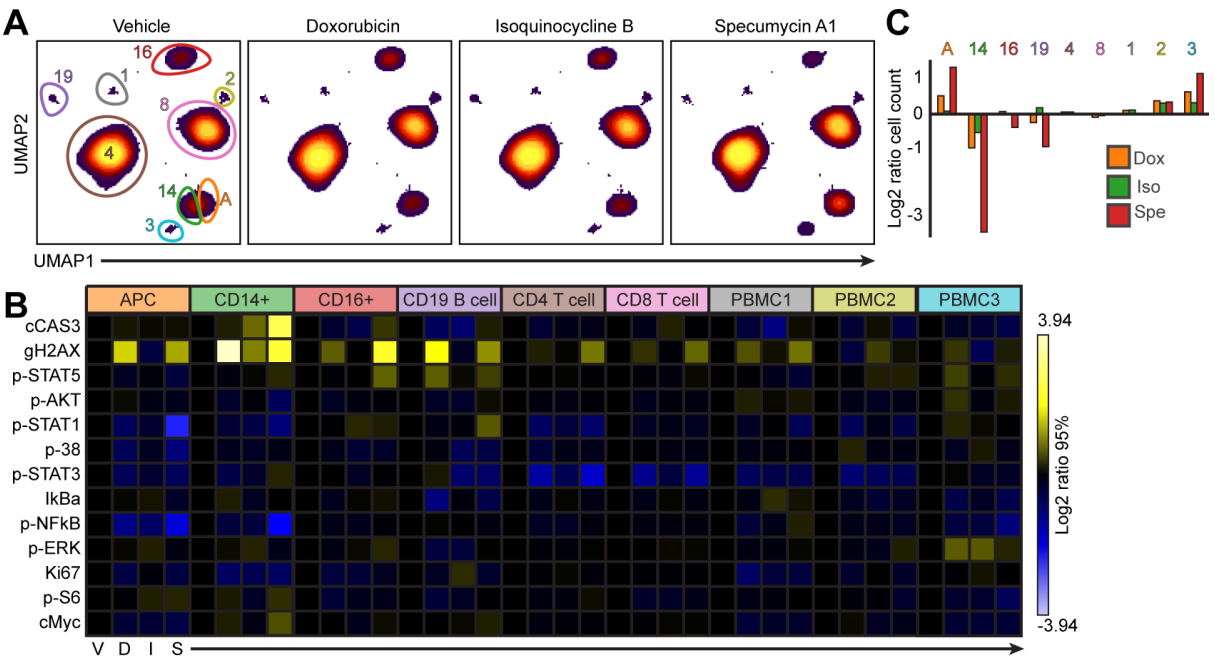

Figure 4.6. Responses of PBMC following anthracycline challenge. (A) UMAP demonstrate shifts in cell density with respect to drug. Gated populations indicate cell type. (B) Functional responses of gated cells. (C) Log2 ratio of cell population shifts with respect to drug.

to p-NFκB in response to challenge with specumycin A1 (Figure 4.6B-C). Taken together this data suggest specumycin A1, but not doxorubicin nor isoquinocycline B, can modulate p-NFκB directed transcription in myeloid lineage cells. A common feature observed in doxorubicin and specumycin A1 but not isoquinocycline challenge conditions is prominent γH2AX DNA damage marker induction. This phenotype has been described previously in cells treated with anthracyclines and is largely thought to be a consequence of topoisomerase inhibition(*13*). Isoquinocycline B however failed to damage DNA in all cell types except monocytes (Figure 4.6B). Moreover, monocyte cell populations demonstrated the most dramatic reduction in cell population ratio compared to vehicle control (Figure 4.6C). These observations support enhanced toxicity of doxorubicin and specumycin A1 compared to isoquinocycline B in PBMC subsets and that monocytes overall are most sensitive to changes in identity and functional phenotypes in the presence of anthracyclines.

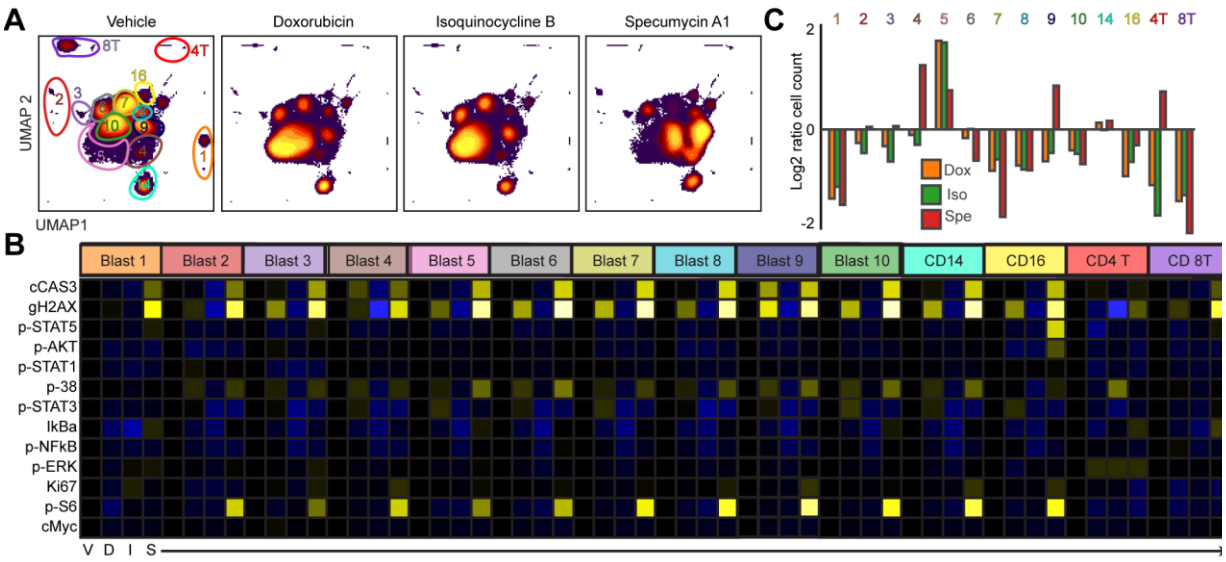

Figure 4.7. Responses of AML patient 03 following anthracycline challenge. (A) UMAP demonstrate shifts in cell density with respect to drug. Gated populations indicate cell type. (B) Functional responses of gated cells. (C) Log2 ratio of cell population shifts with respect to drug.

4.2.5 Blast cell responses to anthracycline challenge are patient specific

Current leukemia standards of care include treatment with an anthracycline drug such as doxorubicin or daunorubicin and targeted therapies specific to gene mutations like *FLT3* or cell surface markers like CD33. The selection of anthracycline for initial chemotherapy are not typically considered on the pretext of gene mutations or cell surface markers. To observe the potential impacts of genetics on anthracycline therapy doxorubicin, isoquinocycline, or specumycin A1 were given to three AML patient samples of different genotypes and assayed for functional responses and changes in Blast cell population ratios by measuring 12 functional and 23 surface marker readouts with Cytof.

Patient AML 03 presented mutation IDH1R132c which confers a mutant isocitrate dehydrogenase 1 (IDH1) protein with oncogenic effects. Patients with this mutation may be sensitive to intensive chemotherapy and require treatment with ivosidenib, a small molecule

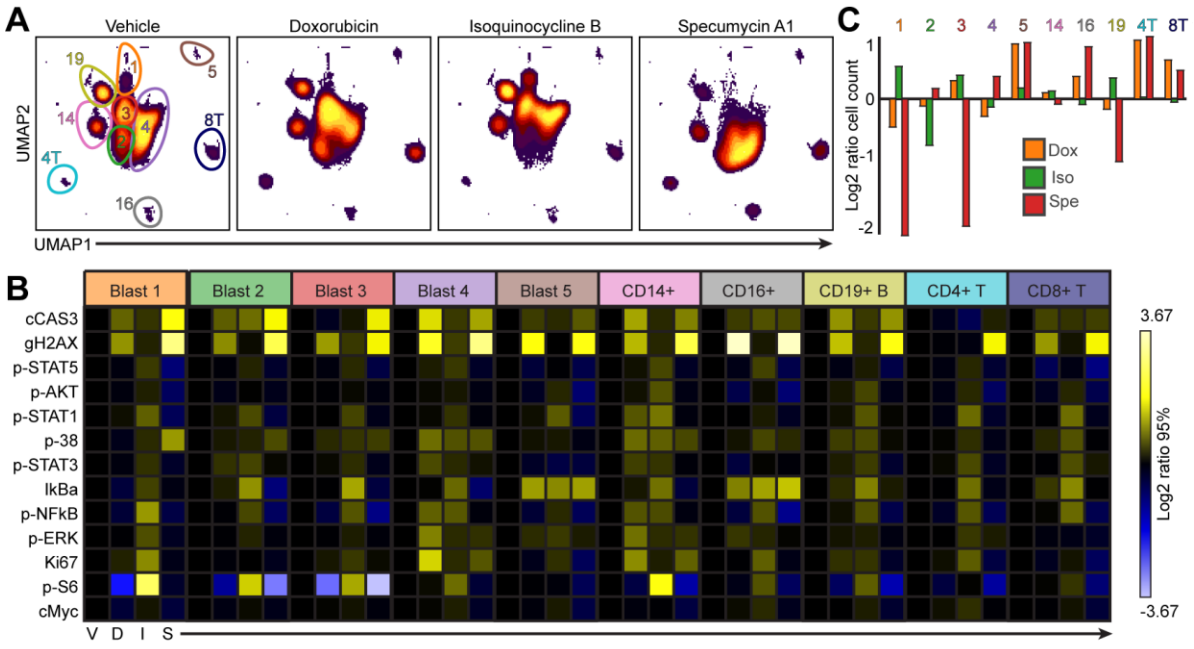

Figure 4.8. Responses of AML patient 10 following anthracycline challenge. (A) UMAP demonstrate shifts in cell density with respect to drug. Gated populations indicate cell type. (B) Functional responses of gated cells. (C) Log2 ratio of cell population shifts with respect to drug.

mutant IDH1 inhibitor, instead of canonical anthracyclines. Thus, interrogating patient specific responses to a variety of anthracycline scaffolds may identify an analog with therapeutic efficacy in patients with IDH1 mutations that lack toxic side effects. This hypothesis was tested by challenging AML 03 patient samples with three anthracycline compounds: doxorubicin, isoquinocycline B, and specumycin A1; then evaluating functional responses is Blast and non-Blast cell populations. The 23 surface identify markers were dimensionally reduced with uniform manifold approximation and projection (UMAP) to assess phenotypes by cell identity. UMAP topology of specumycin A1 treated samples is markedly shifted into the lower right quadrant compared to vehicle and drug challenge (Figure 4.7A). Blast and non-blast cell populations and were hand gated by cell density or surface marker expression in Cytobank. All blast cell and most non-blast, excluding T cells, populations witnessed an increase in the apoptotic marker cCAS3 exclusively in specumycin A1 condition (Figure 4.7B). Specumycin A1 also enhanced translation

marker p-S6 in all populations except Blast 1 and T cells (Figure 4.7B). DNA damage response γH2AX also increased in all cells treated with specumycin A1 (Figure 4.7B). Doxorubicin exhibited a similar DNA damage response as specumycin A1 except Blast 1 and Blast 2 which did not present a large γH2AX signal (Figure 4.7B). In regards to cell identity, only specumycin A1 increased the ratio of Blast 4, Blast 9, and CD4 T cells to that of the vehicle control (Figure 4.7C). The increased cell ratio of Blast 4 and Blast 9 may be due to a shift in surface marker expression or as a consequence of resistance to specumycin A1. This attribute may be beneficial in the context of CD4 T cells as specumycin A1 will spare what healthy CD4 helper T cells are circulating the bloodstream while damaging surrounding Blast populations.

Alternatively, AML patient 10 possessed an FLT3ITD mutation that promotes hematopoietic cell survival, proliferation and differentiation. Interestingly all blast cells were sensitive to all anthracycline compounds albeit across different functional. The distribution of cell density by quadrants was most prominent in isoquinocycline B and specumycin A1 challenged cells; however, the shift magnitude was not mutual between compounds (Figure 4.8A). Doxorubicin and specumycin A1 both induced cCAS3 and γH2AX in all cell populations except CD4 T cells (Figure 4.8B). Isoquinocycline also marginally activated these responses in addition to non-injury specific signals (Figure 4.8B). Notably, the levels of p-NFκB regulator IkB and p-S6 translation status increased in Blast 1, 2, and 3 when challenged with isoquinocycline B (Figure 4.8B). This is in contrast to doxorubicin and specumycin A1 which either decreased or had no effect on IkB or p-S6 compared to vehicle control (Figure 4.8B). It is also interesting to consider that Blast 5 and CD16 NK cells presented increased IkB across drug conditions (Figure 4.8B). The variety of functional responses with respect to drug and cell identity suggest an interplay between compound and cell identity that ultimately determines the functional response.

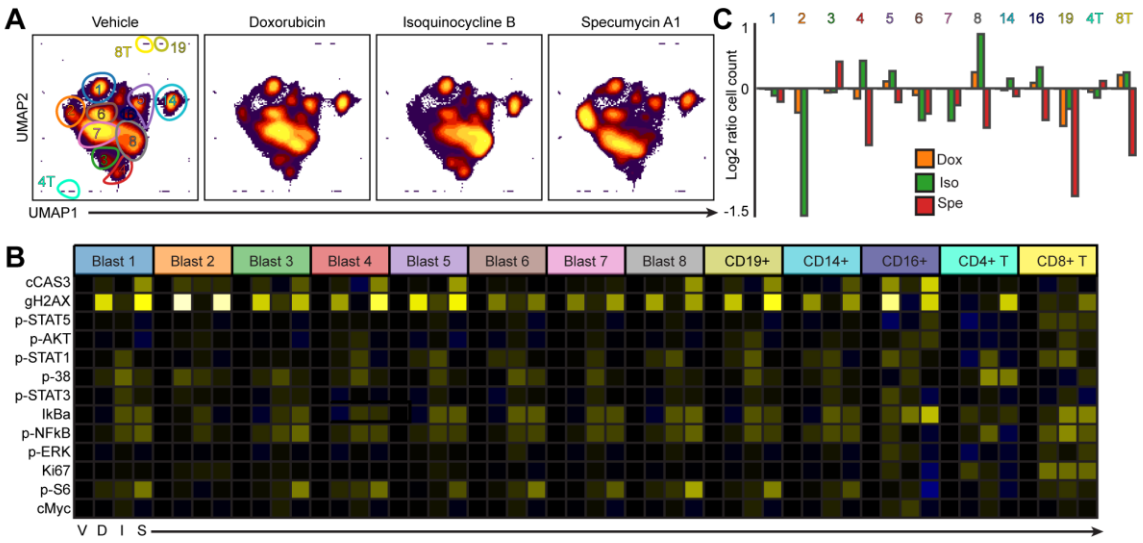

Figure 4.9. Responses of AML patient 13 following anthracycline challenge. (A) UMAP demonstrate shifts in cell density with respect to drug. Gated populations indicate cell type. (B) Functional responses of gated cells. (C) Log2 ratio of cell population shifts with respect to drug.

Patient AML13 with genotype DNMT3A and IDH1R132C was also tested for anthracycline dependent functional responses. The DNMT3A mutation is somatic and effects methylation status such that normally silent genes become active and promote oncogenesis. Consistent with patients AML 03 and AML 10, specumycin A1 induced cCAS3 and γH2AX injury responses in multiple Blast and non-Blast populations (Figure 4.9B). Blast 6 and Blast 7 were resistant to cCAS3 as were T cells (Figure 4.9B). Doxorubicin also activated DNA damage response in all cell types except CD4 T cells (Figure 4.9B). Isoquinocycline B did not activate either apoptotic or DNA damage stressors but did increase IkBa signal similar to patient AML 10 (Figure 4.9B). Specumycin A1, but not doxorubicin, also enhanced IkBa and p-NFκB in Blast and non-blast cell populations (Figure 4.9B). Interestingly, isoquinocycline B exhibited a robust shift of Blast 2 cell population ratio suggesting these cells either died or underwent surface marker identity remodeling (Figure 4.9C).

4. 3 Discussion

The anthracycline family of compounds are commonly prescribed across multiple clinical indications (*8, 14*). The tetracyclic aglycone core promotes DNA intercalation resulting in replication stress and cellular demise (*14*). However, anthracycline treatment is associated with maladaptive cardiotoxic effects (*8, 15*) and can be overcome in refractory or relapsing leukemias (*16, 17*). Exquisite chemical moieties on the D ring effect DNA minor grove binding and enzyme-interacting domains (*14*) and may serve as a selectivity filter that yields robust and varied responses in single cell subsets from heterogenous patient primary cell samples. To observe such effects, we challenged AML patient sample with 1 μM of anthracycline class compound or vehicle control for 24 hours and acquired cell subtype specific response with surface marker and functional marker Cytof panel.

AML genotypes and functional responses exposed some similarities between mutation and drug challenge. For instance, patient AML 03 and AML13 both possessed an IDH1 mutation. In both patients, specumycin A1 induced a strong cCAS3 and γH2AX damage phenotypes as well as increased translation status marker p-S6. The p-S6 phenotype however was less pronounced in AML 13 who also presented with a DNMT3A mutation. Taken together, this suggests Blast cells in patients with IDH1 mutations are sensitive to apoptosis and DNA damage induced by specumycin A1 and that DNMT3A mutations contribute to less robust damage signal phenotypes. Doxorubicin also induced a prominent γH2AX response independent of cCAS3 in AML03 and AML13. Isoquinocycline B did not exhibit robust injury phenotypes. This data suggests the disparity in branched sugars of each anthracycline in crucial to the observed functional phenotypes as no anthracycline induced functional profile was the same for each compound across patients.

Patient AML 10 presented an FLT3 mutation was most sensitive to chemically induced phenotypes of the three patients. In particular, isoquinocycline B stimulated p-S6 and increased detection of regulatory protein IkBa. Elevated p-S6 indicates active translation. Since IkBa levels increased, and the detected form is not a post-translation modification, it is possible that IkBa is one protein being actively translated under isoquinocycline B challenge. An increase in IkBa also suggests decreased transcription of NFκB target genes as IkBa masks nuclear localization of the NFκB protein. However, a concomitant loss of p-NFκB consistent with increased IkBa is lacking in isoquinocycline B challenged cells. Further work is required to elucidate how isoquinocycline B and the p-NFκB pathway through the NFκB pathway detection is not a post-translational modification it is possible that IkBa is a potentia and displayed a unique phenotypic profile with respect to each compound. Doxorubicin Notably, specumycin A1 reduced p-S6 in direct contrast to AML 03 and AML 10

This demonstrated the first application of isoquinocycline B in primary patient samples and compared and contrasted functional responses to anthracyclines with varied sugar side chains. Isoquinocycline B exhibited specific activity for IκBa inhibition or activation dependent on patient and cell type without activation or suppression of p-NFκB. This phenomenon deserves additional attention to discern why and how isoquinocycline B induced this effect but doxorubicin and specumycin A1 were less prolific. Likewise, isoquinocycline B was less efficient than doxorubicin and specumycin A1 to induce apoptotic or DNA damage response signals. Even without robust damage signaling, isoquinocycline B did modulate cluster abundance relative to vehicle control. To definitively answer this question will require single cell tracing studies over multiple timepoints and doses of isoquinocycline B.

Moreover, continued investigation of isoquinocycline B and specumycin A1 offer an avenue for deep interrogation of anthracycline specific cell targeting to kill specific, potentially resistant, cancer cell precursors. Additionally, the immunogenicity of isoquinocycline B is unknown. Despite less toxicity compared to specumycin A1and doxorubicin there is potential for isoquinocycline B to injure cells over an extended time frame or increased dose. Indeed, isoquinocycline B may be an immunogenic compound, like doxorubicin, with potentially less off-target toxicities. Evaluating this family of anthracyclines with the assays described in chapter 2 could reveal therapeutically beneficial immunogenic properties.

Materials & Methods

Cave strain isolation and Identification

Snail Shell (Rockvale), and Cagle's Chasm (South Pittsburg) caves in Tennessee collected between 2010 and 2015 were vortexed in sterile water (100 mg/ml), and supernatants were serially diluted (10-fold, 100-fold, and 1,000-fold) and plated on minimal medium agar plates (ISP2 medium/100-fold diluted, 1.5% agar). Plates were then incubated at 30°C, and colonies were picked over a 3-week period. DNA isolations for purified colonies were performed with a commercial kit (Wizard DNA isolation kit; Promega, Inc.). The 16S rRNA genes for these were then amplified with universal primers 27F (AGA GTT TGA TCC TGG CTC AG) and 1525R (AAG GAG GTG ATC CAG CCG CA) and the use of high-fidelity DNA polymerase (Phusion; Thermo, Inc.). The PCR thermocycler conditions were initial incubation at 98°C for 1 min and 30 cycles of (i) denaturation at 98°C for 0.5 min, (ii) annealing at 59°C for 1 min, and (iii) extension at 72°C for 1.5 min. The final extension step was conducted at 72°C for 10 min. Target 16S rRNA amplicons were purified using a gel extraction kit (QIAquick gel extraction kit). Purified PCR products were directly sequenced from both the 5= and 3= ends, and these sequences were

combined to give the near-full-length 16S rRNA gene sequences. Preliminary genus identifications were determined by a comparison of 16S rRNA gene sequences to type strains in the EzBioCloud database (30). Phylogenetic analsysis was accomplished in Mega7 by muscle alignment of 16s sequences and phylogenetic tree formation using the maximum likelihood method of 1000 bootstrapped experiments.

Preparation of microbial crude extracts

Streptomyces strains were maintained on ISP2 agar (yeast extract 4 g/L, malt extract 10 g/L, glucose 4 g/L, and agar 20 g/L, pH 7.2). Loops of mycelia were used to inoculate 5-mL seed cultures in ISP2 medium (yeast extract 4 g/L, malt extract 10 g/L, and glucose 4 g/L, pH 7.2) for Streptomyces strains, incubating them for 3 days at 30 °C. Seed cultures were then transferred to 250-mL Erlenmeyer flasks containing 25 mL of BA medium (soybean powder 15 g/L, glucose 10 g/L, soluble starch 10 g/L, NaCl 3 g/L, MgSO4 1g/L, K2HPO4 1 g/L, and trace elemental solution 1 mL/L, pH 7.2) and grown for 7 days at 30 °C with shaking. Aqueous fermentation broth was extracted by shaking with Diaion HP20 synthetic absorbent resin (Alfa Aesar) (125 mL of HP20 bead/H2O slurry per 500 mL of aqueous broth) for 2 h. Fermentation broth was then centrifuged (3700 × g, 30 min) and the supernatant was decanted. Metabolites were eluted from absorbent resin and cells with methanol (250 mL of methanol/125 mL of HP20 bead/H2O slurry) by shaking for 1.5 h, followed by centrifugation (3700 × g, 30 min) and decanting of the methanol extract. Further extraction was performed with acetone (250 mL of acetone/125 mL of HP20 bead/H2O slurry) by shaking for 1.5 h, followed by centrifugation (3700 × g, 30 min) and decanting of the acetone extract.

Generation of metabolomic arrays

Mass spectrometry was performed by using a TSQ Triple Quantum mass spectrometer equipped with an electrospray ionization source and Surveyor PDA Plus detector. For positive ion mode, the following settings were used: capillary temperature was 270 °C; spray voltage 4.2 kV; spray current 30 mA; capillary voltage 35 V; tube lens 119 V; and skimmer offset 15 V. For negative ion mode, capillary temperature 270 °C; spray voltage 30 kV; spray current 20 mA; capillary voltage 35 V; tube lens 119 V; and skimmer offset 15 V. Fraction plates were prepared by injecting 20 µL of purified compounds in methanol or concentrated extract via a Thermo PAL auto injector onto a phenomenex luna 5 µm C18(2) reverse-phase HPLC column. The sample was fractionated using a gradient of 100% Buffer A (95% H2O, 5% acetonitrile) to 100% Buffer B (5% acetonitrile, 95% H2O) over 48 min at a flow rate of 1 mL/min and a fixed splitter with a 3:1 ratio with three parts going to the photodiode array detector and fraction collector and one part going to the MS. Fractions were collected in 1-min intervals in a 96 deep well plate. A volume of 150 µL of eluent from each well was transferred to four replica plates and dried in vacuo using a Genevac HT-6 system with standard HPLC-Lyo protocol.

Fluorescent cell barcoding of cell-seeded metabolomic arrays

Eight serial 1:2.14 dilutions of Pacific Blue were prepared, covering a concentration range from 0.038 to 7.67 µg/mL. Six serial 1:2.5 dilutions of Pacific Orange were prepared, covering a concentration range from 0.22 to 21 µg/mL. Each dilution of Pacific Blue was added to all wells in a single row of a 96-well plate (10 µL/well), so that the dye concentration in each row decreased from the top to the bottom of the plate. Similarly, each dilution of Pacific Orange was added to all wells in a column of the same 96-well plate (10 µL/well), so that the concentration in each column decreased from columns 1 to 6 and from columns 7 to 12. This procedure yielded two sets of 48

barcoded wells per plate. Approximately 200,000 cells (180 µL suspended in phosphate-buffered saline (PBS)) were added to each well and incubated in the dark at room temperature for 30 min. Staining was then quenched by addition of 75 µL of 1% BSA (Sigma) in PBS.

Antibody staining

Cells were stained with antibodies in 100-µL staining medium for 30 min in the dark, unless otherwise noted. Individual antibodies were added in accordance with the manufacturer's instructions. Staining was quenched with 1% BSA in PBS, and stained cells were washed with PBS prior to analysis.

Isolation of isoquinocycline B

Isoquinocycline B was isolated from *M. phytophila* was plated on ISP-2 agar yeast extract 4 g/L, malt extract 10 g/L, glucose 4 g/L, and agar 20 g/L, pH 7.2) from glycerol stocks, and incubated at 30 oC for 5-7 days. Cells were then harvested from solid culture, homogenized, and used to inoculate seed cultures (25 mL ISP-2 liquid media (yeast extract 4 g/L, malt extract 10 g/L, glucose 4 g/L, pH 7.2) in 250 mL Erlenmeyer flasks. Seed cultures were incubated at 30°C for 48 hrs, cells were then harvested from liquid cultures, homogenized, and used to inoculate 500 mL Rich Media (Supplemental Table 1). After 7-day incubation, 100 mL of activated Diaion® HP-20 resin (Supelco)/H2O slurry was added to each 500 mL flask and flasks were incubated with shaking for 3 hrs. Cells/resin were then centrifuged (3700 × g, 30 min), the supernatant discarded, and the resin/cellular mass extracted with 200 mL methanol/100 mL Diaion® HP-20 resin (Supelco) used (incubation with shaking for 1 hr). Cell mass/resin was centrifuged (3700 × g, 30 min), methanol extract removed, concentrated and stored, and the resin/cellular mass extracted with 200 mL acetone/100 mL HP-20 resin used (incubation with shaking for 1 hr). The cell mass/resin was again centrifuged (3700 × g, 30 min), and the acetone extract was removed, concentrated and stored.

Crude acetone extract was fractionated with Sephadex LH-20 resin (GE Healthcare Bio-Sciences) with methanol as the eluent. Isoquinocycline B was dereplicated using a combination of mass spectrometry and nuclear magnetic resonance spectroscopy data.

AML patient samples

All specimens were obtained in accordance with the Declaration of Helsinki following protocols approved by the Vanderbilt University Medical Center Institutional Review Board. Details of patients and sample acquisition were previously published49. Briefly, consent was obtained via an approved written consent form, and eligibility criteria included ≥18 years of age with suspected AML undergoing clinical evaluation at Vanderbilt. Samples analyzed here were collected from bone marrow prior to any treatment. Once obtained, samples underwent immediate (within <30 min) density gradient separation of mononuclear cells using a BD Vacutainer CPT Cell Preparation Tube with Sodium Heparin (BD Biosciences, Franklin Lakes, NJ). The separated mononuclear cells were then pelleted with low-speed centrifugation (200 × g) and aliquoted into multiple cryotubes in an 88% FBS + 12% DMSO solution. Samples were stored at −80 °C for 24–72 h prior to long-term storage in liquid nitrogen. Patient 03 is IDH1R132c, 10 is FLT3ITD and abnormal karyotype (46 X, -Y, t(2;21;8)(q13;q22;q21.3),+6[19]/46, XY [1]), 13 is DNMT3A and IDH1R132C.

Mass cytometry

After compound challenge, samples were pelleted by centrifugation at 200 × g, resuspended and washed with PBS (HyClone, HyClone Laboratories, Logan, UT), pelleted, and resuspended in PBS. They were then stained with Cell-ID Cisplatin (Fluidigm, South San Francisco, CA) as per the manufacturer's recommended protocol. The cells were washed and resuspended in staining medium [CSM: PBS + 1% BSA (Fisher Scientific, Fair Lawn, NJ)]. Cells were then stained with

a mass cytometry antibody panel of 22 extracellular antibodies designed to characterize AML blasts and most non-AML peripheral blood mononuclear cells (Supplemental Table 3) and 13 functional markers. A master mix of these antibodies was added to each sample to give a final staining volume of 50 µL and incubated at room temperature for 30 min.

4.5 References

1. J. Chu, X. Vila-Farres, S. F. Brady, Bioactive Synthetic-Bioinformatic Natural Product Cyclic Peptides Inspired by Nonribosomal Peptide Synthetase Gene Clusters from the Human Microbiome. *J Am Chem Soc* **141**, 15737-15741 (2019).
2. J. Chu *et al.*, Discovery of MRSA active antibiotics using primary sequence from the human microbiome. *Nat Chem Biol* **12**, 1004-1006 (2016).
3. H. A. Iqbal, L. Low-Beinart, J. U. Obiajulu, S. F. Brady, Natural Product Discovery through Improved Functional Metagenomics in Streptomyces. *J Am Chem Soc* **138**, 9341-9344 (2016).
4. J. G. Owen *et al.*, Multiplexed metagenome mining using short DNA sequence tags facilitates targeted discovery of epoxyketone proteasome inhibitors. *Proc Natl Acad Sci U S A* **112**, 4221-4226 (2015).
5. NMR Analysis of Quinocycline Antibiotics: Structure Determination of Kosinostatin, an Antitumor Substance from Micromonospora sp. TP-A0468.
6. Kosinostatin, a Quinocycline Antibiotic with Antitumor Activity from Micromonospora sp. TP-A0468.
7. H. M. Ma *et al.*, Unconventional origin and hybrid system for construction of pyrrolopyrrole moiety in kosinostatin biosynthesis. *Chem Biol* **20**, 796-805 (2013).
8. G. Minotti, P. Menna, E. Salvatorelli, G. Cairo, L. Gianni, Anthracyclines: molecular advances and pharmacologic developments in antitumor activity and cardiotoxicity. *Pharmacol Rev* **56**, 185-229 (2004).
9. <CDM-16-412.pdf>.
10. D. C. Earl *et al.*, Discovery of human cell selective effector molecules using single cell multiplexed activity metabolomics. *Nat Commun* **9**, 39 (2018).
11. D. Gewirtz, A critical evaluation of the mechanisms of action proposed for the antitumor effects of the anthracycline antibiotics adriamycin and daunorubicin. *Biochemical Pharmacology* **57**, 727-741 (1999).
12. C. Temperini *et al.*, The crystal structure of the complex between a disaccharide anthracycline and the DNA hexamer d(CGATCG) reveals two different binding sites involving two DNA duplexes. *Nucleic Acids Res* **31**, 1464-1469 (2003).
13. C.-Y. Xie *et al.*, MFTZ-1, an actinomycetes subspecies–derived antitumor macrolide, functions as a novel topoisomerase II poison. *Molecular Cancer Therapeutics* **6**, 3059-3070 (2007).
14. <2008_Book_AnthracyclineChemistryAndBiolo.pdf>.
15. N. R. Neuendorff *et al.*, Anthracycline-related cardiotoxicity in older patients with acute myeloid leukemia: a Young SIOG review paper. *Blood Adv* **4**, 762-775 (2020).
16. P. Ferguson *et al.*, An operational definition of primary refractory acute myeloid leukemia allowing early identification of patients who may benefit from allogeneic stem cell transplantation. *Haematologica* **101**, 1351-1358 (2016).
17. F. Caiado *et al.*, Lineage tracing of acute myeloid leukemia reveals the impact of hypomethylating agents on chemoresistance selection. *Nat Commun* **10**, 4986 (2019).

CHAPTER 5 – Future Directions

5.1 Summary

This work focused on the discovery of natural products that may be beneficial to cancer therapy by invoking cell death that yields chemically induced anti-tumor immunity (CIATI) or induce functional phenotypes in specific cell types. A fluorescent cytometry assay was established to measure six injury signals including autophagy, unfolded protein response (UPR), mitosis, DNA damage, necroptosis, and apoptosis. Measuring these injury phenotypes with multiplexed activity profiling (MAP) and multiplexed activity metabolomics (MAM) identified new bioactivity of the compounds narbomycin, siderochelin, filipins, and isoquinocycline B. Prioritization of compounds for isolation were determined by bioactivity, abundance, and clinical relevance. Isoquinocycline B is a member of the anthracyclines previously reported with weak anti-microbial properties. To investigate the potential of isoquinocycline B in a clinical setting it was compared against doxorubicin and specumycin A1for induction of functional responses and changes in population ratio in cancer cell subsets of healthy and leukemic patients. It was revealed that each anthracycline exhibited some selectivity for functional responses by cell subtype and patient genotype. In total, these studies present a discovery paradigm of secondary metabolites that target specific cell types and engage multiple injury signals that can generate robust and durable immune responses to tumor associated antigens.

5.2 Conclusion

Natural products are a robust medicinal source that elicit specific biological effects via specific molecular targets. Cyclopamine binds the Smoothened receptor to inhibit Hedgehog signaling which results in easily distinguishable developmental deformities. These specific molecular interactions and deformed phenotypes facilitated the discovery of Smoothened as a

cancer target and hatched medicinal chemical campaigns to develop Smoothened inhibitors. These campaigns have provided FDA approved drugs and numerous tool compounds, such as KAAD-cyclopamine, to interrogate hedgehog signaling. Rather than discover compounds and molecular targets by "accident" due to obvious phenotypes, modernized assays such as flow cytometry can be used to measure single cell phenotypes that represent a diverse array of cellular processes.

In addition to cyclopamine derivatives, other natural products such as doxorubicin or cytarabine have found utility as treatments for leukemia, breast, and colon cancers. The continued application of these compounds is due in part to enhancing cell immunogenicity. Immunogenic cancer cells recruit the immune system to the site of tumor insult for phagocytosis of cellular debris including tumor associated antigens (TAA). The TAA are used by the immune system to develop a durable immune response such that tumor cells expressing the same TAA are targeted and destroyed. It was fortuitous that compounds such as doxorubicin, that were originally discovered by cytotoxicity, induced immunogenic cell death (ICD).

In mouse models, ICD affords protection against tumor rechallenge and extends overall survival by invoking chemically induced anti-tumor immunity (CIATI). CIATI is the phenomenon in which compounds invoke a number of cellular processes that prime the immune system to take up and process TAA towards long-term durable immune protection. The avenues to CIATI include a number of molecular signals that are representative of cell injury and can promote ICD. For example, DNA damage can be detected by measuring the phosphorylation status of histone 2AX. Studying such cellular processes in the context of cancer offer an opportunity to discover molecules that act on cell processes conducive to anti-tumor immune responses. This direct approach offers discovery of bioactive natural products, or other small molecules, by stimulation of injury signals conducive to immunogenicity.

In Chapter 2 I developed a fluorescent cytometry module that measured six injury signals implicated in immunogenicity. This module discovered new activity of narbomycin in an unknown metabolomic extract to demonstrate phenotypic drug discovery of secondary metabolites by injury induction at the single cell level. In addition, benchmark control compounds were established as positive controls to maintain assay validity. These compounds were also evaluated for immunogenic potential by measuring the release of ATP and HMGB1 along with externalization of calreticulin. None of the benchmark compounds appeared immunogenic and established that injury does not equal immunogenicity, thus any compound isolated on the basis of injury will require additional testing to determine its immunogenicity.

In Chapter 3 I discussed the rediscovery of siderochelin based on new bioactivity and filipins based on cytotoxicity and UV/MS spectra. This offers two additional examples for the utility of high-throughput single cell assays for discovery of active compounds within complex chemical mixtures. This also established that known molecules may possess unknown bioactivity worthy of additional investigation.

In Chapter 4 I close with the comparison of anthracycline compounds in healthy and leukemic subjects. Using Cytof I characterized cancer cell subsets by 22 surface identity markers and compared functional responses among populations in response to each anthracycline. Responses across patients by compound were unique. This established a first step towards assessing structural analogs of known compounds to better target and elicit injury in specific cancer cell subtypes.

5.3 Future Directions

5.3.1 Is the sequence of injury signals relevant to immunogenicity?

The appearance of numerous injury signals including autophagy, UPR, externalized

calreticulin and DAMP release are necessary for immunogenic death. However, if an optimal injury sequence exists for immunogenic death, it is not yet known. Other cellular events including DNA damage and cell cycle arrest may also be an essential temporal component that enhance or hinder ICD. For instance, if DNA damage occurred prior to autophagy but did not yield an immunogenic response then this injury sequence is not immunogenic. On the other hand, if autophagy was activated then DNA damage occurred and produced an immunogenic response then the sequence of injury can be used to identify or refute immunogenicity.

Status markers for other cellular processes (*e.g.* translation and p-S6) could also be critical events to immunogenicity depending on activation or silence. Consider that a compound may induce p-EIF2α and p-S6. This suggests that despite saturation of ER folding capacity of proteins the cell continues to expend energy on protein synthesis. If these signals were measured in tandem and only enhanced immunogenicity when expressed together, but not alone, would suggest active translation during ER stress is an immunogenic injury but that translation or ER stress alone is not.

5.3.2 Can signaling pathways and or cell identity facilitate drug discovery?

This work focused on measuring terminal effectors of molecular pathways with canonical sequence. For example, the necroptotic marker p-MLKL is phosphorylated by p-RIPK3 which is phosphorylated by p-RIPK1 (*1-3*). Including the phospho-status of all three kinases in an immunogenic module could be used to identify temporal relationships among phospho-status markers in response to drug challenge. Additionally, activation of necroptosis confirmed by p-MLKL in the absence of p-RIPK events would suggest an alternative pathway for p-MLKL activation and subsequent necroptosis. This observation would lay groundwork to interrogate alternative p-MLKL pathways and prioritize isolation of a compound that imparts a unique signaling phenotype. This discovery platform can also be expanded into additional cell types. Lung

and breast cancer cells are much more susceptible to ICD than leukemias and may offer a more suitable experimental model for identifying secondary metabolites with immunogenic potential (*4-6*). Following cell line incorporation, the platform could be advanced to include cell identify markers in addition to injury signals to expedite discovery of cell type selectivity of pure compounds. For example, hematopoietic surface markers CD33, CD38, and CD34 could be adjoined to the injury module to identify optimal concentrations and timepoints of chemically induced phenotypic shifts across cancer cell populations in clinical samples(*7*).

5.3.3 Are siderochelin or narbomycin active in primary patient samples?

The DNA damage phenotype exhibited by siderochelin was a pleasant surprise and immediately opens questions the chemical mechanism of siderochelin interactions with its biological target. Siderochelin effected DNA damage in MV-4-11 leukemia cell line but is unknown if it induced a similar phenotype in primary AML samples and if it possesses cell subtype selectivity. The injury phenotype induced by narbomycin was a novel discovery. Since it belongs to the macrolide family of natural products and effected LC3 levels it likely falls under the umbrella of an inhibitor of autophagic flux (*8*). The induction of LC3 is a necessary signal for ICD (*9-11*) and the control macrolide compound prompted ATP release. It would be interesting to investigate narbomycins potential to induce the three canonical hallmarks of ICD to expand the ICI – ICD roadmap. If narbomycin did produce ICD hallmarks it would advance into phagocytosis assays to assess phagocyte responses of macrophages towards narbomycin challenged cancer cells. Additionally exploring narbomycin injury profile in AML patient samples may introduce new utility to this compound.

5.3.4 Does immunogenic cell injury stimulate phagocytosis?

In addition to measuring chemically induced ICI to identify hit bioactivity, monocyte derived dendritic cells (MoDC)s)(*12*) could be stimulated with expired tumor cells and/or spent media. Chemically challenged, fluorescently labeled cancer cells would be incubated with macrophages marked with an alternative fluorescent label and allowed to incubate 48 hours. Cells would be sampled at 4, 24, and 48 hours to measure the number of double positive fluorescent cells with flow cytometry as a surrogate for phagocytosis. MoDCs would be incubated with (1) chemically challenged cells in spent media, (2) chemically challenged cells in fresh media, or (3) spent media with unchallenged cells. Double positive cells in condition one would indicate either chemically challenged cells or spent media enhance phagocytosis. Double positive cells in condition 2 but not 3 would indicate the injured cells promote phagocytosis. Double positive cells in condition 3 but not 2 would indicate the spent media possess some DAMP that enhances phagocytosis. Double positive cells in conditions 2 and 3 would indicate both the chemically challenged cell and spent media present components that activate MoDC phagocytosis. In a MAM experiment, the condition with double positive cells would be referred back to complementary spectral data to identify candidate compounds for isolation and the supernatant evaluated for immunogenic DAMPs ATP and HMGB1. If neither ATP nor HMB1 are detected then some other DAMP in the spent is potentially activating phagocytosis in macrophages. This would be immediately relevant as moDC are an *ex vivo* differentiated primary cell type that mimics APC that can be recruited to the tumor site to phagocytose expiring tumor cells and present antigen to downstream effector cell types of adaptive immunity.

5.3.5 Can cell identity and/or functional profiles tailor patient specific chemotherapy?

One possible application of molecules inducing ICI is an *ex-vivo* treatment paradigm for

prolonged immunological protection that obviates direct exposure to chemotherapies with debilitating side effects. For example, this injury module could be adjoined to cell identification modules (e.g., leukemia stem cell populations) for characterization of cell injury cross-indexed by cell type and sub-types. In effect, ICI signatures of patient samples could infer and confirm optimal chemotherapies that target new cancer cell types, and thus exposure of novel tumor antigens, as they arise during disease progression. Chemically induced ICI and subsequent ICD activated cancer cells reintroduced to the patient could provide a continuous supply of personalized TAA vaccines that builds long term antitumor immunity. The addition of an antigen cross presentation assay would also help validate ICI candidates toward antitumor immunity studies in animals.

5.3.6 Can immunogenic compounds complement existing immunotherapies?

ICI treated cancer cells have potential as an adjuvant to current immunotherapies. Immune checkpoint blockade with PD-1 and CTLA4 antibodies exhibit minimal efficacy in immunogenically silent tumors due to minimal expression of chemotactic stimuli that recruits T cells or due to lack of mutations in TAA that activate T cells (*13*). Likewise, chimeric antigen receptor T (CAR-T) cell therapy designed to recognize and eliminate cancer cells in an antigen specific fashion may fail due to poor tumor penetration or downregulation of the target antigen (*14*, *15*). It is also possible for cancer cells to experience immunoediting: genetic and non-genetic processes that decrease immunogenicity. Incorporating secondary metabolites that penetrate tumors to induce ICI and subsequent ICD may overcome these barriers by enhancing expression of immunogenic signals that recruit and activate T cell responses.

5.4 References

1. D. A. Rodriguez *et al.*, Characterization of RIPK3-mediated phosphorylation of the activation loop of MLKL during necroptosis. *Cell Death & Differentiation* **23**, 76-88 (2016).
2. K. Weber, R. Roelandt, I. Bruggeman, Y. Estornes, P. Vandenabeele, Nuclear RIPK3 and MLKL contribute to cytosolic necrosome formation and necroptosis. *Communications Biology* **1**, (2018).
3. A. L. Samson *et al.*, MLKL trafficking and accumulation at the plasma membrane control the kinetics and threshold for necroptosis. *Nature Communications* **11**, (2020).
4. M. Sauler, I. S. Bazan, P. J. Lee, Cell Death in the Lung: The Apoptosis–Necroptosis Axis. *Annual Review of Physiology* **81**, 375-402 (2019).
5. T. Flieswasser *et al.*, Clinically Relevant Chemotherapeutics Have the Ability to Induce Immunogenic Cell Death in Non-Small Cell Lung Cancer. *Cells* **9**, 1474 (2020).
6. S. Nobili *et al.*, Vinorelbine in Non-Small Cell Lung Cancer: Real-World Data From a Single-Institution Experience. *Oncology Research Featuring Preclinical and Clinical Cancer Therapeutics* **28**, 237-248 (2020).
7. D. C. Earl *et al.*, Discovery of human cell selective effector molecules using single cell multiplexed activity metabolomics. *Nat Commun* **9**, 39 (2018).
8. S. Moriya *et al.*, Macrolide antibiotics block autophagy flux and sensitize to bortezomib via endoplasmic reticulum stress-mediated CHOP induction in myeloma cells. *International Journal of Oncology* **42**, 1541-1550 (2013).
9. D. J. Klionsky *et al.*, Guidelines for the use and interpretation of assays for monitoring autophagy. *Autophagy* **8**, 445-544 (2012).
10. L. Galluzzi *et al.*, Consensus guidelines for the definition, detection and interpretation of immunogenic cell death. *Journal for ImmunoTherapy of Cancer* **8**, e000337 (2020).
11. M. Michaud *et al.*, Autophagy-Dependent Anticancer Immune Responses Induced by Chemotherapeutic Agents in Mice. *Science* **334**, 1573-1577 (2011).
12. T. Q. Chometon *et al.*, A protocol for rapid monocyte isolation and generation of singular human monocyte-derived dendritic cells. *PLOS ONE* **15**, e0231132 (2020).
13. M. W. Teng, S. F. Ngiow, A. Ribas, M. J. Smyth, Classifying Cancers Based on T-cell Infiltration and PD-L1. *Cancer Res* **75**, 2139-2145 (2015).
14. E. Alard *et al.*, Advances in Anti-Cancer Immunotherapy: Car-T Cell, Checkpoint Inhibitors, Dendritic Cell Vaccines, and Oncolytic Viruses, and Emerging Cellular and Molecular Targets. *Cancers* **12**, 1826 (2020).
15. R. C. Sterner, R. M. Sterner, CAR-T cell therapy: current limitations and potential strategies. *Blood Cancer Journal* **11**, (2021).